NOVEL APPROACH FOR DIRECT METHODS IN MEDICAL IMAGING USING COMPRESSIVE SENSING

GABRIEL LUIS DE ARAÚJO E FREITAS

DISSERTAÇÃO DE MESTRADO EM ENGENHARIA ELÉTRICA
DEPARTAMENTO DE ENGENHARIA ELÉTRICA

FACULDADE DE TECNOLOGIA

UNIVERSIDADE DE BRASÍLIA

UNIVERSIDADE DE BRASÍLIA
FACULDADE DE TECNOLOGIA
DEPARTAMENTO DE ENGENHARIA ELÉTRICA

NOVEL APPROACH FOR DIRECT METHODS IN MEDICAL IMAGING USING COMPRESSIVE SENSING

UMA NOVA ABORDAGEM PARA O USO DE MÉTODOS DIRETOS NA RECONSTRUÇÃO DE IMAGENS MÉDICAS COM COMPRESSIVE SENSING

GABRIEL LUIS DE ARAÚJO E FREITAS

ORIENTADOR: VINÍCIUS PEREIRA GONÇALVES, PHD.
COORIENTADOR: CRISTIANO JACQUES MIOSSO, PHD.

DISSERTAÇÃO DE MESTRADO EM
ENGENHARIA ELÉTRICA

PUBLICAÇÃO: PPGENE.DM-790/22

BRASÍLIA/DF: JULHO - 2022

UNIVERSIDADE DE BRASÍLIA
FACULDADE DE TECNOLOGIA
DEPARTAMENTO DE ENGENHARIA ELÉTRICA

NOVEL APPROACH FOR DIRECT METHODS IN MEDICAL IMAGING USING COMPRESSIVE SENSING

GABRIEL LUIS DE ARAÚJO E FREITAS

DISSERTAÇÃO DE MESTRADO SUBMETIDA AO DEPARTAMENTO DE ENGENHARIA ELÉTRICA DA FACULDADE DE TECNOLOGIA DA UNIVERSIDADE DE BRASÍLIA COMO PARTE DOS REQUISITOS NECESSÁRIOS PARA A OBTENÇÃO DO GRAU DE MESTRE.

APROVADA POR:

Vinícius Pereira Gonçalves, PhD. – ENE/UnB
Orientador

Mylene Christine Queiroz de Farias, PhD. – ENE/UnB
Membro Interno

Vinícius de Carvalho Rispoli, PhD. – FGA/UnB
Membro Interno

BRASÍLIA, 15 DE JULHO DE 2022.

FICHA CATALOGRÁFICA

GABRIEL L. A. FREITAS
Novel Approach for Direct Methods in Medical Imaging Using Compressive Sensing [Distrito Federal] 2022.
xxii, 116p., 210 x 297 mm (ENE/FT/UnB, Mestre, Engenharia Elétrica, 2022).
Dissertação de Mestrado – Universidade de Brasília, Faculdade de Tecnologia.
Departamento de Engenharia Elétrica

1. Imageamento Médico
2. Compressive Sensing
3. Método Direto
4. Minimização Não-Convexa

I. ENE/FT/UnB
II. Título (série)

REFERÊNCIA BIBLIOGRÁFICA

FREITAS, GABRIEL L.A. (2022). Novel Approach for Direct Methods in Medical Imaging Using Compressive Sensing . Dissertação de Mestrado em Engenharia Elétrica, Publicação PPGENE.DM-790/22, Departamento de Engenharia Elétrica, Universidade de Brasília, Brasília, DF, 116p.

CESSÃO DE DIREITOS

Gabriel Luis de Araújo e Freitas

Departamento de Engenharia Elétrica (ENE) - FT
Universidade de Brasília (UnB)
Campus Darcy Ribeiro
CEP 70919-970 - Brasília - DF - Brasil

Aos meus pais, Iron e Joana

ACKNOWLEDGMENTS

O trabalho de pesquisa apresentado nessa dissertação foi desenvolvido durante a pandemia de COVID-19. Portanto, inicialmente gostaria de agradecer aos profissionais das mais diversas áreas que nos permitiram passar por esses dias estranhos com algum tipo de esperança.

Agradeço ao meu pai, Iron Freitas, minha mãe, Joana Araújo e minha irmã, Fernanda. Tal apoio é fundamental para meu desenvolvimento enquanto pessoa e pesquisador. A presença deles fez com que os dias fossem mais leves e me permitiu dedicar integralmente ao trabalho de pesquisa.

Desde a graduação, a Universidade de Brasília me apresentou a vários amigos que, apesar do contato mais distante nos últimos anos, estiveram sempre presentes de alguma forma. São eles, Adriel, Ana Beatriz, Ana Laura, Eduardo, Hugo, Ian, Lucas F, Luso e Victor

Agradeço ao corpo docente e de funcionários do PPGEE. Em especial, ao meu orientador Vinícius Gonçalves por todo apoio e ensinamentos ao longo dos últimos anos. Agradeço também meu coorientador Cristiano Miosso, que me apresentou grande parte dos conceitos trabalhados na pesquisa e foi essencial para a construção da minha visão de mundo enquanto pesquisador. Por fim, gostaria agradecer à professora Mylène Queiroz e ao professor Vinícius Rispoli, que participaram da banca de avaliação e fizeram comentários valiosos que contribuíram para a qualidade deste trabalho.

O presente trabalho foi realizado com apoio da Coordenação de Aperfeiçoamento de Pessoal de Nível Superior – Brasil (CAPES) – Código de Financiamento 001.

***

The research work presented in this thesis was developed during the COVID-19 pandemic. Therefore, I would first like to thank the professionals from the most diverse areas that allowed us to go through these strange days with some hope.

I thank my father, Iron Freitas, my mother, Joana Araújo, and my sister, Fernanda. This support was fundamental to my development as a person and researcher. Their presence made my days lighter and allowed me to fully dedicate to the research work.

Since my undergraduate, the University of Brasilia introduced me to several friends who, although we have been apart in recent years, were always present in some way. They are Adriel, Ana Beatriz, Ana Laura, Eduardo, Hugo, Ian, Lucas F, Luso, and Victor.

I thank the PPGEE's professors and collaborators. In special thanks to my advisor

Vinícius Gonçalves for all the support and teachings throughout the last years. I also thank my co-adviser, Cristiano Miosso, who introduced me to most of the concepts worked on in the research and was essential for the construction of my worldview as a researcher. Finally, I would like to thank professors Mylène Queiroz and Vinícius Rispoli, who participated in the examining board and made valuable comments that contributed to the quality of this work.

This study was financed in part by the Coordenação de Aperfeiçoamento de Pessoal de Nível Superior – Brasil (CAPES) – Finance Code 001.

Viver é melhor que sonhar
Eu sei que o amor é uma coisa boa
Mas também sei que qualquer canto
É menor do que a vida de qualquer pessoa
Como Nossos Pais, Belchior

RESUMO

Título: Uma Nova Abordagem para o Uso de Métodos Diretos na Reconstrução de Imagens Médicas com Compressive Sensing
Autor: Gabriel Luis de Araújo e Freitas
Orientador: Vinícius Pereira Gonçalves, PhD.
Coorientador: Cristiano Jacques Miosso, PhD.
Programa de Pós-Graduação em Engenharia Elétrica
Brasília, 15 de julho de 2022

A partir das tecnologias de imageamento médico, profissionais de saúde conseguem informações relevantes sobre o estado de um paciente para o planejamento e acompanhamento de seu tratamento. A Tomografia Computadorizada por raios-x (CT) e a Ressonância Magnética (MR) são duas das tecnologias mais bem consolidadas no meio. Estas técnicas permitem a obtenção de imagens anatômicas de planos específicos ou volumes. Apesar de a CT e a MR explorarem princípios físicos diferentes, ambas coletam medidas que podem ser modeladas como coeficientes da Transformada de Fourier da imagem a ser reconstruída.

O processo de reconstrução refere-se a etapa de calcular a imagem desejada a partir das medidas adquiridas pelos equipamentos médicos. A aquisição geralmente requer que o paciente permaneça em uma mesma posição por longos períodos e, no caso da CT, há a emissão de radiação ionizante. Assim, é de interesse que tais procedimentos ocorram da forma mais segura e rápida possível. Uma maneira de abordar este problema é o desenvolvimento de algoritmos de reconstrução que consigam gerar imagens úteis para a atividade clínica usando uma quantidade reduzida de medidas.

Conceitos de *Compressive Sensing* (CS) vem sendo adotados na elaboração de novos algoritmos para reconstrução de imagens médicas em vista de uma aquisição mais eficiente. Esta área de conhecimento estuda a reconstrução de sinais a partir de medidas incompletas por meio da resolução de sistemas lineares subdeterminados. O sinal de interesse é a solução cuja maior parte dos coeficientes é nula. Ou seja, considera-se que o sinal reconstruído possui uma representação esparsa em algum domínio conhecido. A minimização de ℓ_p $(0 < p \leq 1)$ é uma estratégia frequentemente explorada por algoritmos de CS. Adotar métricas ℓ_p com menores valores de p, apesar de recair em problemas não-convexos, pode possibilitar uma redução ainda maior de medidas.

Imagens são sinais de grande dimensão. Por esta razão, técnicas de reconstrução que se baseiam em CS recorrem a métodos indiretos para a realização de operações matriciais, já que o armazenamento das matrizes que modelam o problema é inviável durante a execução dos algoritmos. A estabilidade e a convergência dos métodos indiretos são afetadas pela redução do valor de p de modo que esta estratégia não pode ser bem explorada ao executar as operações matriciais indiretamente.

Neste contexto, a presente pesquisa desenvolve a Estrutura de Reconstrução Direta (DRS) para formação de imagens médicas por meio da composição de sinais de menor dimensão, que são obtidos através de minimização de ℓ_p. Inicialmente, apresentamos o formalismo matemático para implementações genéricas dessa estrutura, em que não se assume nenhuma operação específica para a composição. Em um segundo momento, derivamos o modelo matemático e o problema de minimização para uma formulação que compõe a imagem a partir de sinais unidimensionais, que contém a informação de uma linha de medidas no plano de frequências.

Implementamos esta formulação específica do DRS usando o IRLS (*Iteratively Reweighted Least Squares*) como algoritmo de minimização e a pré-filtragem para a representação esparsa. Realizamos quatro experimentos numéricos com o objetivo de investigar o comportamento dos algoritmos de CS ao reduzirmos o valor de p e avaliar a performance do DRS em comparação às técnicas que usam método indireto. Em nossos testes usamos tanto sinais artificiais como dados de imagens reais. Os resultados apontam que o DRS reconstrói satisfatoriamente as imagens médicas em condições favoráveis de esparsidade. A pré-filtragem não obteve a mesma eficiência em esparsificar os sinais reconstruídos pelo DRS em comparação ao que é verificado no caso dos algoritmos que usam método indireto.

Palavras-chave: Imageamento Médico, Compressive Sensing, Método Direto, Minimização Não-Convexa.

ABSTRACT

Title: Novel Approach for Direct Methods in Medical Imaging Using Compressive Sensing
Author: Gabriel Luis de Araújo e Freitas
Supervisor: Vinícius Pereira Gonçalves, PhD.
Co-Supervisor: Cristiano Jacques Miosso, PhD.
Graduate Program in Electronic and Automation Systems Engineering
Brasília, July 15th, 2022

With the support of medical imaging technologies, healthcare workers are provided with relevant information about a patient's condition when planning and following up on treatment. X-ray Computed Tomography (CT) and Magnetic Resonance (MR) are two of the most consolidated technologies in the field. These techniques yield anatomical images of specific planes or volumes. Although CT and MR exploit different physical principles, both collect measurements that can be modeled as the Fourier Transform coefficients of the image to be reconstructed.

The reconstruction procedure refers to the stage of computing the desired image from the measurements acquired by the medical equipment. The acquisition usually requires the patient to stay in the same position for long periods, and, in the case of CT, there is the emission of ionizing radiation. Thus, such procedures should take place as safely and quickly as possible. A possible approach to address this issue is the development of reconstruction algorithms that can generate meaningful images for clinical practice from a reduced amount of measurements.

Concepts of Compressive Sensing (CS) have been adopted in the devising of new algorithms for medical imaging to achieve a more efficient acquisition. This area of knowledge studies the reconstruction of signals from incomplete measurements by solving underdetermined linear systems. The signal of interest is the solution whose most of the coefficients are null. That is, the reconstructed signal is assumed to have a sparse representation in a known domain. Minimizing ℓ_p $(0 < p \leq 1)$ is a strategy often exploited by CS algorithms. Adopting ℓ_p metrics with smaller values of p, even leading to non-convex problems, opens up the possibility of further reductions in the number of measurements.

Images are large signals. For this reason, CS-based reconstruction techniques rely on indirect methods to perform matrix operations because the storage of the matrices that model the problem is impractical during the execution of the algorithms. The stability and convergence of indirect methods are affected by reducing the value of p so that this strategy cannot be well exploited when performing matrix operations indirectly.

In this background, the present research devises the Direct Reconstruction Structure (DRS) for medical image formation through the composition of lower-dimensional signals, which are obtained through ℓ_p minimization. First, we present the mathematical formalism for generic implementations of this structure, which makes no assumptions about the operation for composition. Following, we derive the mathematical model and the minimization problem for a formulation that composes the image from one-dimensional signals, which contain the information of a row of measurements in the frequency plane.

We implemented that specific DRS formulation using the Iteratively Reweighted Least Squares (IRLS) as the minimization algorithm and prefiltering for sparse representation. We conducted four numerical experiments to investigate the behavior of the CS algorithms when reducing the value of p and evaluate the performance of DRS compared to techniques using an indirect method. In our tests, we used both artificial signals and actual image data. The results suggest that DRS can satisfactorily reconstruct medical images in good sparsity conditions. Prefiltering did not achieve the same effect in sparsifying the signals reconstructed by DRS compared to the case of algorithms using the indirect method.

Keywords: Medical Imaging, Compressive Sensing, Direct Method, Non-Convex Minimization.

Contents

1 INTRODUCTION 1

1.1 The context of medical imaging 1

1.2 Stating the scientific problem and the research proposal 2

1.3 Objectives 4

1.4 Outline of this thesis 5

2 THEORETICAL FOUNDATIONS OF MEDICAL IMAGING 6

2.1 Computed Tomography 7

2.1.1 Physical principle 7

2.1.2 Mathematical modeling 8

2.1.3 Filtered Back Projection 10

2.2 Magnetic Resonance 11

2.2.1 Physical principle 11

2.2.2 Mathematical modeling 13

2.2.3 Non-Uniform Fast Fourier Transform 14

2.3 Artificial phantoms 15

3 THEORETICAL FOUNDATIONS OF COMPRESSIVE SENSING 17

3.1 The basics of Linear Algebra for Compressive Sensing 18

3.1.1 Sparsity and ℓ_p metrics 18

3.2 The sparse reconstruction problem 20

3.3 Conditions for sparse reconstruction 22

3.4 An interpretation of CS from Linear Algebra 28

3.5 Compressive Sensing algorithms 29

3.5.1 Orthogonal Matching Pursuit 30

3.5.2 Iteratively Reweighted Least Squares 31

3.6 Compressive Sensing for medical imaging reconstruction 32

3.6.1 Prefiltering 33

3.6.2 From sinogram projections to measurements in the frequency plane 34

3.6.2.1 Defining the radial lines on the Cartesian grid 35

3.6.2.2 The interpolation step 36

3.6.2.3 The Goertzel algorithm 36
3.6.3 Conjugate Gradient method 37

4 THE PROPOSED DIRECT RECONSTRUCTION STRUCTURE FOR MEDICAL IMAGING 38
4.1 General implementations of the DRS 39
4.2 Mathematical model for a DRS formulation based on the reconstruction of rows 40
4.3 Limitations of the decomposition by rows for modeling the DRS 45
4.4 An implementation of DRS with prefiltering 46
4.4.1 Adapting the MR implementation of DRS to CT 47

5 COMPUTATIONAL EXPERIMENTS 48
5.1 Parameters for results evaluation 49
5.2 Experiment 1 – investigating the effects of adopting smaller values of p on the reconstruction quality with a 1D toy example 50
5.2.1 Simulation methodology 50
5.2.2 Results and discussion 51
5.2.2.1 The effect of the number of iterations on the reconstruction quality 52
5.2.2.2 The effect of using ℓ_p with smaller p in reconstruction quality 55
5.2.2.3 A remark on sparsity reconstruction conditions 61
5.3 Default image reconstruction settings 64
5.4 Experiment 2 – image reconstruction using prefiltering as the sparsity representation strategy 69
5.4.1 Simulation methodology 69
5.4.2 Results and discussion 70
5.5 Experiment 3 – reconstructions of synthetic images sparse on 1D domain 80
5.5.1 Synthetic image generation 81
5.5.2 Simulation methodology 81
5.5.3 Results and discussion 82
5.6 Experiment 4 – the effect of the interpolations on the computation of the measurements on the Cartesian grid from a sinogram 86
5.6.1 Simulation methodology 86
5.6.2 Results and discussion 86
5.7 Compilation of the discussion of all experiments 89

6 CONCLUSION 90
6.1 Summary of contributions 91
6.2 Published works 92

6.3 Future works 92
6.4 Final Considerations 93

REFERENCES 94

A ADDITIONAL PLOTS 101
A.1 CT1 actual image 101
A.2 CT2 actual image 104
A.3 MR1 actual image 105
A.4 MR2 actual image 107

B ADDITIONAL RECONSTRUCTED IMAGES 108
B.1 CT1 actual image 108
B.2 CT2 actual image 111
B.3 MR1 actual image 112
B.4 MR2 actual image 115

List of Figures

2.1 Example of geometries for acquiring measurements used in commercial CT scanners. 7
2.2 Representation of the trajectory of parallel beams. 9
2.3 Example of CT image and its Radon Transform. 9
2.4 Example of CT image reconstruction using Back-Projection and Filtered Back-Projection algorithms with projections acquired in 200 angles. 11
2.5 Example of MR image and the position of its measurements acquired in a spiral trajectory in the frequency plane. 14
2.6 The 256×256 Shepp-Logan phantom. 15

3.1 Geometrical representation of some two-dimensional unit ℓ_p balls. 19
3.2 Venn diagram summarizing the Compressive Sensing acquisition and reconstruction processes. 29
3.3 General prefiltering scheme. 33
3.4 Radial lines approximation with 20 angles on Cartesian grid taking different tolerances. The white pixels represents the position in the radial lines. 35
3.5 Example of interpolated sinogram of the 512×512 Shepp-Logan phantom for a Cartesian grid taking measurements in 16 angles. 36

4.1 Generic representation of the Direct Reconstruction Structure for an arbitrary decomposition of the relationship between the measurements and the sparse signal to be reconstructed. 40
4.2 A signal that contains the pixel domain information related to a single row in the frequency plane. This example was calculated from the 50^{th} row of the spectrum content of the 256×256 Shepp-Logan phantom. 42
4.3 Representation of the DRS formulation based on reconstructions of the contribution of each row of measurements. 44
4.4 Comparison between the DRS and the conventional CS-based reconstruction approach (with an indirect method) in the design of the ℓ_p minimization problems. 44

4.5 Reconstruction scheme using the DRS with prefiltering for CT images. In the case of MR, the scheme remains the same, but the process starts with the measurements already in the frequency plane, and they can be in other trajectories than radial lines. 47

5.1 Ratio of measurements per non-null entry to be estimated by IRLS for each acquisition scheme in reconstructing the synthetic one-dimensional signals. 52
5.2 Histograms of the SNR that reconstructions achieved for each scenario. Each plot contains two histograms. Note that the distributions are similar, so there is a significant overlap between them. 52
5.3 Histogram of the difference between the SNR obtained by reconstructions of the same signal with $i_{max} = 30$ and $i_{max} = 10$. Negative values indicate that reconstruction quality was impaired when running more iterations in IRLS. Cases where the convergence criterion was reached in up to 10 iterations have the same SNR regardless of the value of i_{max}, and the difference is zero. 54
5.4 Distribution of the values of p at which the reconstructions of the signals with 128 non-zero entries did not converge. 54
5.5 Histograms of the SNR achieved for each set of signals (16 and 128 non-null entries) separated according to the value of p adopted in the reconstruction and the method for matrix computations in IRLS. 55
5.6 Distribution of the reconstructions into 40 groups defined for the Wilcoxon tests to verify in which conditions the reduction of p reflects in quality gain. 57
5.7 Mean SNR value achieved in reconstructing the sparser synthetic signals (16 non-null entries) for each scenario. The area filled around the curves indicates the range of one standard deviation centered on the mean. 60
5.8 Mean SNR value achieved in reconstructing the less sparse synthetic signals (128 non-null entries) for each scenario. The area filled around the curves indicates the range of one standard deviation centered on the mean. 61
5.9 Mutual-Coherence criteria for each acquisition matrix available for experiment 1. 62
5.10 Distribution of the best reconstruction for each set of measurements. 63
5.11 Percentage of positions in the 256×256 grid that is measurements for each number of angles when defining the Cartesian radial lines with $tol = 0.698$. 65

5.12 The actual CT images used in our experiments from COVID-19 image data collection. 67
5.13 The actual MR images used in our experiments from Biomedical Informatics Research Network. 68
5.14 SNR achieved by the reconstructions of the Shepp-Logan phantom. Each surface corresponds to a reconstructions algorithm. 70
5.15 SSIM achieved by the reconstructions of the Shepp-Logan phantom. Each surface corresponds to a reconstructions algorithm 71
5.16 SNR achieved by the reconstructions computed using measurements along 220 radial lines of the Shepp-Logan phantom. Each curve corresponds to a reconstruction algorithm. 72
5.17 SSIM achieved by the reconstructions computed using measurements along 220 radial lines of the Shepp-Logan phantom. Each curve corresponds to a reconstruction algorithm. 72
5.18 SNR achieved by the reconstructions of the Shepp-Logan phantom. Each curve corresponds to a reconstruction algorithm. The CS-based approaches used $p = 1$ in the minimization step. 73
5.19 SSIM achieved by the reconstructions of the Shepp-Logan phantom. Each curve corresponds to a reconstruction algorithm. The CS-based approaches used $p = 1$ in the minimization step. 73
5.20 Reconstructions of the Shepp-Logan phantom from non-ideal measurements taken in 200 angles. 74
5.21 Reconstructions of the Shepp-Logan phantom from non-ideal measurements taken in 120 angles. 75
5.22 Reconstructions of the MR1 actual image from measurements taken in 170 angles. We chose to omit the axes in the representation of the images so that they would all fit on a single page. 76
5.23 SNR achieved by the reconstructions of the CT2 actual image. Each curve corresponds to a reconstruction algorithm. The CS-based approaches used $p = 1$ in the minimization step. 77
5.24 SSIM achieved by the reconstructions of the CT2 actual image. Each curve corresponds to a reconstruction algorithm. The CS-based approaches used $p = 1$ in the minimization step. 78
5.25 Quality indices achieved by the reconstructions of the MR2 actual image. Each curve corresponds to a reconstruction algorithm. The CS-based approaches used $p = 1$ in the minimization step. 78
5.26 Runtime for each CS-based algorithm when reconstructing the Shepp-Logan phantom using ideal and non-ideal measurements along 120 angles. 79

5.27 Runtime for each CS-based algorithm when reconstructing the CT2 actual image using ideal and non-ideal measurements along 120 angles. 79
5.28 Examples of signals reconstructed by CS minimization using direct and indirect methods to form the Shepp-Logan phantom using prefiltering as the sparsity representation strategy. 80
5.29 Example of a synthetic image created by replacing with zeros 60% of the entries of the one-dimensional signals of an actual 256×256 CT image. . 82
5.30 SNR achieved by the reconstructions of the synthetic images generated from actual CT images. Each surface corresponds to every reconstruction of the same synthetic image (the colors identify the percentage of null elements in the sparse one-dimensional signals). Each chart gathers data from artificial images generated from the same actual image (indicated in the caption beneath). 83
5.31 SNR achieved by the reconstructions of the synthetic images generated from actual MR images. Each surface corresponds to every reconstruction of the same synthetic image (the colors identify the percentage of null elements in the sparse one-dimensional signals). Each chart gathers data from artificial images generated from the same actual image (indicated in the caption beneath). 84
5.32 SNR achieved by some reconstructions of the synthetic images generated from the actual image CT1. Each curve corresponds to every reconstruction of the same synthetic image (the colors identify the percentage of null elements in the sparse one-dimensional signals). Each chart gathers data from reconstructions from measurements taken in the same amount of angles (indicated in the caption beneath). 85
5.33 Percentage of positions in the 256×256 grid that are measurements for each tolerance value when defining the Cartesian radial lines with 120 angles. 87
5.34 Error in the estimation of measurements of the 256×256 Shepp-Logan phantom in the Cartesian radial lines from 120 projections for different values of tolerance. 87
5.35 Quality of reconstructions of the Shepp-Logan phantom in terms of SNR and SSIM when using Cartesian radial lines defined with different tolerance values. 88

List of Algorithms

3.1 Orthogonal Matching Pursuit. 31
3.2 Iteratively Reweighted Least Squares. 32
3.3 Calculation of measurements in frequency plane from sinogram. 34
4.1 Direct Reconstruction Structure based on the reconstruction of rows with prefiltering. 46
5.1 Generation of a synthetic image that is sparse in a one-dimensional transformed domain. 82

List of Tables

5.1 Parameters for IRLS the reconstruction of synthetic 1D signals. 51

5.2 The Anderson-Darling test statistic for each group of $1,000$ reconstructions. If the returned statistic is larger than 1.088, then for the significance level of 1%, the null hypothesis that the data come from a normal distribution can be rejected. 58

5.3 The Wilcoxon test p-values for each comparison between the metrics adopted in reconstructions. The fields filled in blue are the p-values for which H_0 is rejected for the usual confidence levels. In red are the cases in which we cannot reject the H_0. Moreover, in yellow are the cases that can or cannot be rejected depending on the desired confidence level. 59

5.4 Parameters used in reconstructions with IRLS. 66

5.5 Identifiers of the actual images used in the numerical experiments. 66

5.6 Percentage of entries whose magnitude is under 10^{-6} for each filtered version of the testing images reconstructed by the CS algorithms 69

Acronyms

AI	Artificial Intelligence.
BIRN	Biomedical Informatics Research Network.
CG	Conjugate Gradient.
CS	Compressive Sensing.
CT	Computed Tomography.
DFT	Discrete Fourier Transform.
DRS	Direct Reconstruction Structure.
DTFT	Discrete-Time Fourier Transform.
FBP	Filteted Back-Projection.
FFT	Fast Fourier Transform.
FID	Free Induced Decay.
FST	Fast Slice Theorem.
IDFT	Inverse Discrete Fourier Transform.
IFFT	Inverse Fast Fourier Transform.
IRLS	Iteratively Reweighted Least Squares.
MI	Measurements Inversion.
MR	Magnetic Resonance.
NUFFT	Non-Uniform Fast Fourier Transform.
OMP	Orthogonal Matching Pursuit.
PET	Positron Emission Tomography.

RIC Restricted Isometry Constant.
RIP Restricted Isometry Property.

SNR Signal-to-Noise Ratio.
SSIM Structural Similarity Index Measure.

TV Total Variation.

WHO World Health Organization.

Chapter 1

Introduction

This research investigates the adoption of direct methods for matrix computations in Compressive Sensing (CS) algorithms for medical image reconstruction. Our first intent in proposing this study is to provide a reconstruction approach that relies on fewer measurements to obtain clinically useful images. We will present the theoretical model of a medical image reconstruction algorithm and experimentally evaluate its performance compared to an algorithm that uses an indirect method. In addition, we will numerically evaluate the impact of using a direct method on CS reconstruction in a generic scenario. In this first chapter, we will present the general context of medical imaging, introduce the scientific problem that the research addresses, as well as our objectives. In the end, we outline the structure of the remaining chapters.

1.1 The context of medical imaging

Medical images are important information sources to guide healthcare workers' decisions. Several stages of medical treatment make use of these technologies, from screening to follow-up. The progress of knowledge about the physical phenomena involved in image acquisition and the development of novel digital signal processing techniques have allowed the evolution of medical imaging procedures. Over the years, scientific research has developed more reliable methods that provide accurate information at lower operational costs [1].

The variety of physical principles and possible technologies for medical imaging allow obtaining different information about the internal structures of an organism. Clinicians can use it in managing a large number of pathologies. As such, medical imaging is a key resource in the practice of today's medicine [1, 2]. Evidence of that is the attention the World Health Organization (WHO) gives to the topic. A brief search on its website finds publications covering a wide range of aspects, from ethical

parameters regarding patient exposure to ionizing radiation during image acquisition [3] to issues about the use of these technologies in resource-scarce scenarios [4, 5] and their clinical usage in the treatment of various medical conditions [6].

The access to imaging in low and lower-middle-income countries is discussed in [2]. This study reviews why these countries have not adequately implemented medical imaging services and also suggests actions to overcome these barriers. Although the main proposed measures are of a political and economic nature, the technical improvement of technologies is cited as part of the solution. In this sense, several issues in medical imaging can be the subject of study in scientific research. For example, the survey in [7] points out future directions in the field with a focusing on Artificial Intelligence (AI) approaches. It organizes the current challenges into six key topics: (i) Image formation and acquisition, (ii) Data management and sharing in the context of big data, (iii) Data processing paradigms in radiology, (iv) Digital pathology, (v) 3D reconstruction and visualization, (vi) Integrative analytics and radiogenomics paradigm. Although our research does not involve AI, it contributes to the issues of image formation and acquisition. In this regard, studies such as [8, 9, 10] are examples of works in the same context

Image quality, as means of the relevance of the information obtained for clinical decision-making, is a pertinent factor when evaluating the performance of an imaging scheme [11]. In the case of Magnetic Resonance (MR) and x-ray Computed Tomography (CT), for instance, the image formation depends on a reconstruction step to convert the signals acquired by the equipment into images that have visual meaning for the human perception. Therefore, the image quality relies on the capacity of the reconstruction algorithm to extract information from the measurements to yield a meaningful representation of the structures of interest.

The larger the number of measurements, the more information is available for reconstructing the image. Thus, the same algorithm is expected to achieve higher quality levels in situations where more measurements are acquired. However, obtaining a larger amount of measurements implies longer acquisition times and higher patient exposure to ionizing radiation in cases such as CT. Thus, developing algorithms that compute images of a good standard from a reduced number of measurements leads to faster and safer acquisition stages.

1.2 Stating the scientific problem and the research proposal

Compressive Sensing is a field of study in digital signal processing that uses underdetermined linear systems to model reconstruction problems to design more efficient

acquisition schemes [12]. Reducing the number of measurements is achieved by assuming that the signal to be reconstructed has a sparse representation (whose most of the coefficients are zero) in some known domain. A possible way to evaluate the sparsity is through ℓ_p metrics[1] ($0 < p \leq 1$). Thus, the reconstruction of the signal can be given by solving an ℓ_p optimization problem subjected to the linear system [12, 13]. So, the adoption of CS in the context of medical imaging is a possible strategy for devising novel reconstruction algorithms [11].

One of the first ideas to get a sparse representation of tomographic signals exploits the fact that these images usually consist of relatively uniform regions with sharp edges [11]. Following this premise, some works have proposed medical image reconstruction schemes based on minimizing the Total Variation (TV) measure, among which we cite [14, 15]. Strategies based on ℓ_p metrics have also been explored for developing image reconstruction methods with CS techniques [16, 8]. We remark that there are a variety of alternatives to model the matrices that describe the acquisition of measurements, mainly due to the discretization process. Likewise, several formulations can be considered for the CS minimization problem by varying the cost function and the constraint. These design choices can lead to reconstruction algorithms that are quite distinct from each other. The survey in [11] systematically describes different approaches that take TV as the sparsity criterion.

The matrices that model the acquisition in medical imaging can be very large. It is often impractical to operate directly with them due to storage limitations during the algorithm execution. Therefore, a common feature among the CS-based algorithms we found in the literature is that they all rely on indirect methods at some stage of the image reconstruction process. Here, what we mean by an indirect method is any numerical technique that computes exact or approximately the solution to linear systems without using the coefficients of the matrix that describes the problem, such as Conjugate Gradient (CG) and Quasi-Newton methods. In contrast, direct methods are solvers with the matrix available to compute the operations.

Further reducing the number of measurements by using smaller values of p is a possibility that arises when developing models based on ℓ_p minimization [17]. However, this can not be well exploited by the algorithms we have mentioned. The models usually rely on poorly conditioned matrices [11], so reducing the value of p may affect the convergence and the stability of the indirect methods in a way that compromises the adoption of a smaller p in practical situations (either due to prohibitive computational time or unsatisfactory solutions).

[1] ℓ_p is not rigorously a norm in the mathematical sense for $p < 1$. However, it is common in CS literature to refer to them with "norm," "pseudonorm," or "quasinorm." Here, we have chosen to use the term "metric."

We propose the Direct Reconstruction Structure (DRS) for CT and MR in our study. In both of these imaging technologies, data used in reconstruction can be modeled as samples of the Fourier coefficients of the desired image. However, while MR measurements are already acquired in the frequency plane, CT measurements are projections related to the desired spectral information. We use the approach presented in [9] to condition the CT data as Fourier coefficients in a discrete Cartesian grid.

The strategy of DRS is based on composing the image from smaller signals, which can be reconstructed by CS algorithms using direct methods. Thus, we expect this new scheme to reduce the value of p in the definition of the minimization problem. One of our numerical experiments will compare the performance of the proposed reconstruction structure with another technique that uses an indirect method in different scenarios. Although there are no longer any noteworthy similarities, the very first ideas in the DRS development came from an attempt to adapt the streaming signal reconstruction algorithm presented in [18] to the medical imaging context.

1.3 Objectives

The study we present in this thesis was conducted with the following research question: "What are some benefits to the quality of medical images, in terms of objective parameters, achieved by reconstructing them using direct methods in Compressive Sensing algorithms?". Thus, the general objective of the research is to design a CS-based reconstruction scheme for CT and MR images that uses direct methods and investigate the potential contributions of this technique in helping to make the acquisition of measurements safer and faster. We can detail this primary objective in the following specific objectives:

1. Develop a formal discussion about the behavior of the reconstruction quality when reducing the value of p in the ℓ_p minimization problem.

2. Derive and present the mathematical model for general implementations of the DRS.

3. Derive a mathematical model for DRS regarding a specific composition strategy and implement this formulation computationally.

4. Test the performance, as means of objective parameters, of that specific DRS formulation for reconstructing images using measurements computed from synthetic and actual images.

5. Analyze the effect of the algorithm for arranging the CT measurements as Fourier coefficients proposed by [9] on reconstruction quality.

1.4 Outline of this thesis

The literature review consists of two Chapters. Chapter 2 introduces physical principles, mathematical models, and classical CT and MR image reconstruction algorithms. In Chapter 3, we present the basic concepts of CS, which include the formulation of the sparse reconstruction as an ℓ_p minimization problem, a discussion of reconstruction conditions, algorithms for general cases, and a possible approach for medical image reconstruction with a CS algorithm using an indirect method. In particular, Section 3.4 presents our interpretation of CS using concepts from Linear Algebra.

We propose the Direct Reconstruction Structure for medial imaging in Chapter 4. At first, the DRS is introduced from its mathematical motivation. The general idea is to make the use of the direct method in the reconstruction algorithms feasible by composing the image from signals of reduced dimension. These signals are the solutions to CS minimization problems. Next, we derive a specific formulation based on the reconstruction of one-dimensional signals that contains the information relative to the measurements in a row of the Cartesian plane. Finally, we provide a reconstruction scheme for CT and MR images that uses DRS. We point out that the formulation we present in this work is not unique since DRS can lead to other reconstruction schemes, which model the image composition differently and use different strategies for sparsity representation.

We conducted computational experiments intending to verify the performance of DRS in comparison with a reconstruction algorithm that uses an indirect method. Chapter 5 presents both the methodological design and results discussions of the experiments. We chose to organize the content this way to ensure the cohesion of the text because the two last experiments are motivated by the results observed in a previous experiment. Chapter 6 presents the final considerations, summarizing the contributions and pointing out future work.

Chapter 2

Theoretical Foundations of Medical Imaging

Medical imaging technologies comprise a set of methods that enable the visualization of internal structures and functional aspects of the human body, often using non-invasive techniques. The evolution of such technologies has provided valuable tools for medicine in assisting the diagnosis and monitoring of medical conditions. The earliest approach consists of emitting x-rays over the region of the body that is to be imaged. Each biological tissue has a different radiation absorption capacity. Thus, each beam of radiation will have a different intensity after passing through the body, depending on the tissues it passes through. With this, it is possible to form the image on a photosensitive film positioned behind the body. These results were obtained from the studies of Wilhelm Röntgen [19]

Today there is a wide variety of technologies, based on many different physical principles, for the formation of medical images. Thus, the choice of which technology is most appropriate for each situation depends on what information is relevant for medical evaluation, as well as the general conditions of the patient.

The digital signal processing field contributes to the development of more advanced methods for medical imaging. In this sense, there are contributions both in image formation processes and post-processing and classification techniques to aid diagnosis. For instance, recent studies in medical image formation address issues such as (i) faster measurements acquisition schemes, (ii) better image quality, (iii) safer processes, and (iv) more computationally efficient algorithms [8, 9, 10, 16].

This work deals with Compressive Sensing based reconstruction methods for two-dimensional Computed Tomography and Magnetic Resonance images. This chapter covers an overview of these two technologies' physical concepts and mathematical models. The major references we adopted are [20, 21] for CT; and [22] for MR.

2.1 Computed Tomography

Computed Tomography images are also formed from the emission of radiation onto the object of interest. However, the image is not captured directly on a film behind the object but calculated from a collection of x-ray projections [20]. In contrast to conventional x-ray techniques, the CT approach allows the computation of cross-sectional images, which can visualize more specific details in narrowly delimited regions. The invention of the first CT scanner is attributed to Hounsfield.

2.1.1 Physical principle

The Beer-Lambert-Bouguer law models the attenuation of electromagnetic beams from the properties of the attenuating medium. In the case where a source emits radiation with initial intensity I_0 on a uniform object of thickness d, the intensity of the beam observed after passing through this object is given by the equation

$$I = I_0 e^{-\alpha d}, \tag{2.1}$$

where α is the linear attenuation coefficient related to the capacity of the medium to absorbs radiation. The projections used to calculate the image are measurements of the attenuation of the beams emitted into the object from different directions [20, 21].

The measurements acquired by a CT apparatus refer to the attenuation that an x-ray beam undergoes when passing through the object of interest in a specific linear path. Since each biological tissue absorbs a different amount of radiation, it is possible to compute an image from the information of the x-ray attenuation in some different directions as each beam will pass through a different combination of tissues [20, 21].

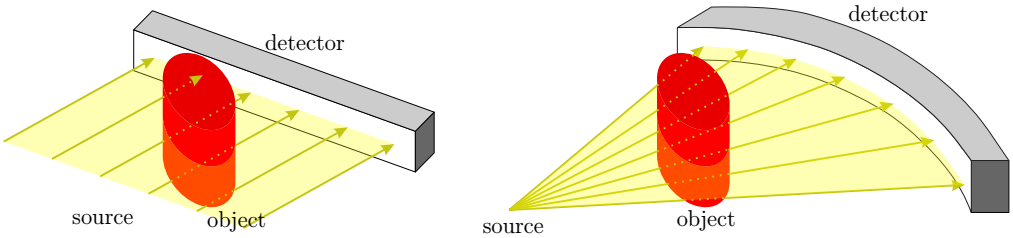

(a) Parallel beams. (b) Fan beams.

Figure 2.1 – Example of geometries for acquiring measurements used in commercial CT scanners.

There are a variety of possible geometries to arrange the radiation sources and sensors for the acquisition of measurements. The first commercial scanners used measurements acquired by parallel beams. Later, fan beams, which are emitted from the

same point, also became used. In this research, we consider measurements acquired by parallel projections. However, the algorithms we will describe can be used in the fan beams acquisition scheme if an intermediate interpolation step is performed to estimate the measurements that would be acquired in parallel beams. Figure 2.1 illustrates these acquisition geometries. The evolution of the acquisition strategies over the generations of commercial CT scanners, as well as more details about the physical phenomena that occur in the interaction of x-rays with matter, can be found in [21].

2.1.2 Mathematical modeling

As illustrated in Figure 2.2, let us identify the path $L(\theta, t)$ of each beam by the parameters θ, indicating the angle from which the beam was emitted; and t, referring to the position of the source in the array. In the case of CT imaging, the rays no longer propagate in a uniform medium. Despite this, the attenuation of each beam can also be modeled using Equation 2.1. For this new scenario, consider that each beam passes through k different sections that are uniform with attenuation coefficients $\alpha_1, \ldots, \alpha_k$. Thus, the resulting intensity is given by

$$I_k = I_0 e^{-\sum_{i=1}^{k} \alpha_i d}, \tag{2.2}$$

and the total attenuation caused by these k sections can be calculated as

$$-\ln\left(\frac{I_k}{I_0}\right) = \sum_{i=1}^{k} \alpha_i d. \tag{2.3}$$

At last, taking $k \to \infty$ allow us to compute the total attenuation along the trajectory $L(\theta, t)$. Therefore, the projections are given by

$$P(\theta, t) = \int_{L(\theta,t)} f(x, y) dL, \tag{2.4}$$

where $f(x, y)$ can be understood as a density function related to the linear attenuation coefficient α of each point (x, y) in the imaged plane. Substituting the differential dL to its Cartesian coordinate expression leads to the following form

$$P(\theta, t) = \int_{-\infty}^{\infty} \int_{-\infty}^{\infty} f(x, y)\delta(x\cos\theta + y\sin\theta - t)dxdy, \tag{2.5}$$

where δ is the Dirac delta function. This formulation allows an understanding that the CT image is an estimation of the attenuation distribution computed from projections modeled as line integrals [21].

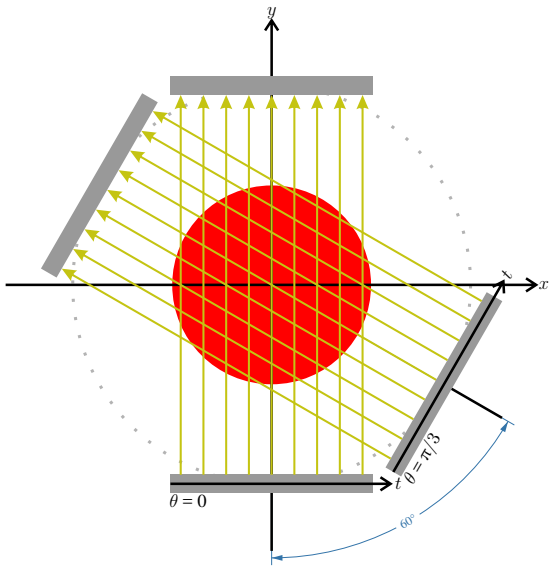

Figure 2.2 – Representation of the trajectory of parallel beams.

Forming a CT image consists of calculating a signal $f[m,n] \in \mathbb{R}^{M\times N}$ from the set of projections $P(\theta,t)$ taken by the scanner. The image $f[m,n]$ is a discrete signal that samples a function $f(x,y) \in \mathbb{R}^2$, which describes the coefficient α for each point (x,y) of a particular slice of the imaged object. Equation 2.5 is also known as the Radon Transform. Figure 2.3 shows an actual CT image from [23] and the set of projections used to reconstruct it. This type of graphical representation of $P(\theta,t)$ is called a sinogram because of the sinusoidal patterns in it.

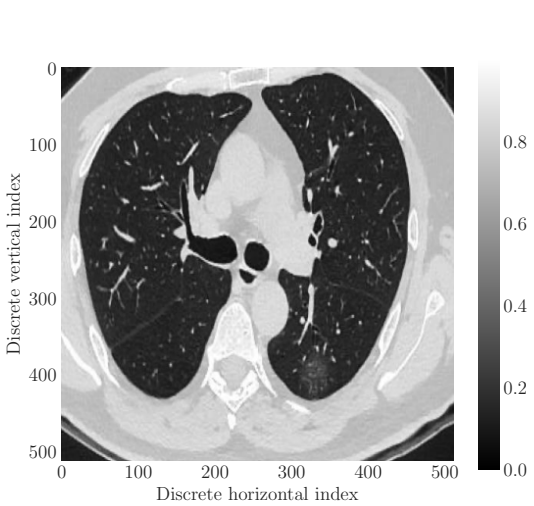

(a) 512 × 512 CT image

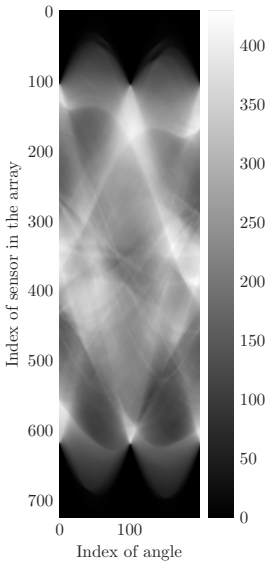

(b) sinogram (200 angles)

Figure 2.3 – Example of CT image and its Radon Transform.

2.1.3 Filtered Back Projection

The reconstruction algorithms for CT images seek a solution to the problem of inverting the Radon Transform. In this regard, the Fourier Slice Theorem (FST) is an important mathematical tool, as it establishes a relationship between the acquired projections and the spectral content of the image. The Fourier Transform of a projection acquired at a given angle equals the Fourier Transform of the image evaluated on the radial line at the same angle [20, 21]. This is stated as Theorem 2.1.

Theorem 2.1 ***Fourier Slice Theorem***

Given a function $f(x, y)$ with two-dimensional Fourier Transform $F(u, v)$ and Radon Transform $P(\theta, t)$. The content of F taken in a radial line at angle $\theta = \theta_i$ concerning the horizontal axis of frequencies can be computed as the one-dimensional Fourier transform of the column $P(\theta_i, t)$ of the Radon Transform. That is,

$$F(t\cos(\theta_i), t\sin(\theta_i)) = \mathcal{F}_{1D}\{P(\theta_i, t)\}, \tag{2.6}$$

where $\mathcal{F}_{1D}\{\cdot\}$ is the one-dimensional Fourier Transform operator.

The Filtered Back-Projection (FBP) is a milestone in the history of CT scanners and, for several decades, was the standard algorithm used in commercial equipment [24]. The Back-projection approach to reconstructing an image is to add the values of the projections along all pixels in their corresponding directions. Images obtained using this strategy are commonly characterized by blurred patterns.

The FST provides an intuitive explanation for that behavior. The blurry appearance in images is caused by the energy concentration in the image spectrum's low-frequency components. Note that due to the acquisition geometry of parallel projections, there is a higher density of samples at the low-frequency positions. Thus, Back-Projection is an algorithm that emphasizes the low-frequency information that results in the blurred artifacts. Equation 2.6 shows that blurred aspect of the reconstructed image can be reduced by one-dimensional filtering of the projections. So the FBP algorithm applies a ramp low-pass filter to the projections before back-projecting them [20, 21]. For example, Figure 2.4 shows reconstructions of the image in Figure 2.3 using Back-Projection and Filtered Back-Projection.

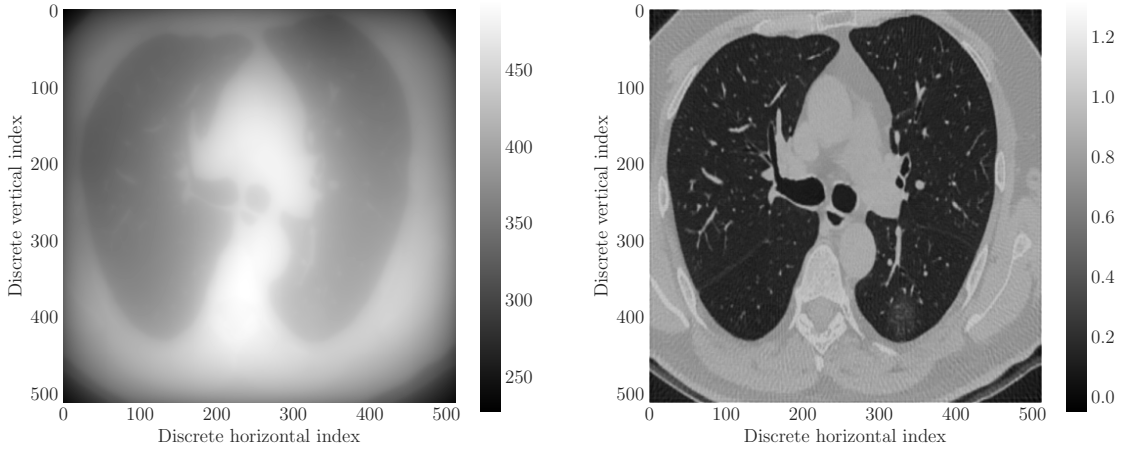

(a) Back-projection.

(b) Filtered Back-Projection.

Figure 2.4 – Example of CT image reconstruction using Back-Projection and Filtered Back-Projection algorithms with projections acquired in 200 angles.

2.2 Magnetic Resonance

Magnetic Resonance is another technique to obtain cross-sectional images. In this method, the image is calculated from measurements of the nuclear magnetic moments of the hydrogen atoms that compose the biological tissues. The MR acquisition scheme starts by placing the object to be imaged in a strong magnetic field, and sequences of magnetic pulses are applied. Then, coils measure the magnetic flux caused by the protons when returning to a lower energy state. At last, these measurements are used to calculate the desired image. In contrast to CT, MR imaging uses non-ionizing radiation and therefore presents less risk to the patient. The basis for the development of magnetic resonance technology comes from the work of Paul Lauterbur [19].

2.2.1 Physical principle

In their natural state, the spins of the protons of the hydrogen atoms in an organism are disordered. That is, each one is pointing in a random direction. Thus, the observed magnetization of the organism as a totality is zero. When the patient is inside the MRI scanner, he is exposed to a uniform magnetic field $B_z = B_0$. Conventionally, this field is along the anatomical longitudinal axis labeled by z. Part of the spins align to the field direction, while the other part assumes the anti-parallel direction. The Boltzmann factor describes this behavior of the spins interacting with B_0 as

$$\frac{N_p}{N_{ap}} = e^{\frac{\varepsilon}{kT}}, \tag{2.7}$$

where ε is the energy difference between the parallel and anti-parallel states, N_p is the number of parallel spins, N_{ap} is the number of anti-parallel spins, k is the Boltzmann constant, and T is the temperature [22]. Therefore, a non-zero resultant magnetization M_0 is now observed due to the alignment of the spins caused by the B_0 field. M_0 will be proportional to the intensity of B_0. Typical values for magnetic flux density in commercial equipment are between 1.5 and 3 tesla, although studies such as [25] investigate the use of Low-Field-Strength in MR imaging.

Another phenomenon that occurs as a result of the interaction of the spins with the external magnetic field is the precession motion. It means that the spins are not only aligned with B_0 but also make a circular motion around the z-axis due to the torque produced by the magnetic field [22]. The angular frequency of precession motion, also known as the Larmor frequency, is given by

$$\omega = \gamma B_z, \tag{2.8}$$

where γ is the gyromagnetic ratio.

After the spins align to B_0, radiofrequency pulses are emitted and disturb the magnetic field in the x and y directions. It causes new alterations in the alignment of the spins. When the perturbation ceases, the spins return to their previous state of equilibrium. The signal for the image reconstruction results from the magnetization $M_{xy} = M_x + jM_y$ in the xy plane during this process [26]. Precession generates an effective electric current, producing its magnetic field. Thus, the signal in the receiver coils is the sum of the contribution of each spin distributed along with the imaged object. In mathematical terms, this signal at time t is given by

$$s_u(t) = \int_{-\infty}^{\infty}\int_{-\infty}^{\infty}\int_{-\infty}^{\infty} M_{xy}(x, y, z, t)dxdydz. \tag{2.9}$$

Recall that s_u is generated by the realignment of the spins to the uniform field B_0 after emitting the RF pulse.

The signal s_u is a global measurement of the magnetization of the imaged object over time during the realignment of the spins. However, it is not yet possible to compute the image from that measurements since this signal does not allow the evaluation of M_{xy} individually for each position (x, y, z) in space. This issue, known as spatial encoding, is addressed by applying linear gradients to the field B_0 in a manner that weights the contribution of each $M_{xy}(x, y, z, t)$ in the signal obtained in the receiver coils. In MR scanners, in addition to the uniform magnetic field, some coils apply gradients to it to enable spatial encoding. Therefore, the resulting magnetic field strength is given by

$$B_z(x,y,z,t) = B_0 + G^T(t)\begin{bmatrix} x \\ y \\ z \end{bmatrix} \tag{2.10}$$

$$B_z(x,y,z,t) = B_0 + G_x(t)x + G_y(t)y + G_z(t)z, \tag{2.11}$$

where $G^T(t) = [G_x(t)\ G_y(t)\ G_z(t)]$ is the gradient strength in each direction. In this new scenario, in which the magnetic field B_z is no longer uniform, the Larmor frequency of the spins also varies with their position (see Equation 2.8). The signal $s(t)$ that is measured in the coils during the process of realignment to the non-uniform field B_z after the emission of the RF pulses is called the Free Induced Decay (FID) [22].

The spin realignment is described by the Bloch phenomenological equations [26]. The magnetization behavior observed in this process is a consequence of the interaction of the spins with their surroundings (lattice) and with each other. In the Bloch equations, each of these interactions is characterized by a time constant. While T_1 relates the spin-lattice interaction to the relaxation in the longitudinal axis, T_2 relates the spin-spin interaction to the realignment in the transverse plane [22].

The MR scanner will emit different sequences of RF pulses during the measurement acquisition process. By adjusting the pattern of these pulse sequences, it is possible to ponder the contributions of the constants T_1 and T_2 to the measurements. This way, it is possible to improve the contrast between different organs represented in the image since the T_1 and T_2 values can be used to distinguish the various biological tissues [22].

2.2.2 Mathematical modeling

As discussed in the previous section, the weight given to the contribution of each point in forming the signal $s(t)$ is defined by the gradient applied to the field B_z. In essence, the FID signal $s(t)$ corresponds to the sum of sinusoidal signals generated by the spins. Due to the gradient $G(t)$, the magnitudes and phases of these sinusoids depend on the spatial position of each spin [22]. Therefore, the reconstructed image tells the density of spins at each point of the imaged object, and the signal $s(t)$ available for image reconstruction is given by

$$s(t) = \int_{-\infty}^{\infty}\int_{-\infty}^{\infty}\int_{-\infty}^{\infty} M_{xy}(x,y,z,t)e^{-j2\pi[k_x(t)x+k_y(t)y+k_z(t)z]}dxdydz, \tag{2.12}$$

where $k^T(t) = [k_x(t)\ k_y(t)\ k_z(t)]$ is the vector of positions defined from the gradient $G(t)$ by

$$k(t) = \frac{\gamma}{2\pi} \int_0^t G(\lambda) d\lambda. \tag{2.13}$$

Therefore, the time samples of $s(t)$ correspond to samples of the Fourier Transform of the imaged object in a trajectory described by $k(t)$ [22].

The signals in the coils that generate the gradient $G(t)$ define the trajectory on which the samples of $s(t)$ will be acquired. The manipulation of these signals enables the selection of the region of interest to be imaged. Each trajectory has different acquisition times and reconstruction features; more details can be found in [22]. Figure 2.5 shows an MR image from [27] and the spiral trajectory in the two-dimensional case.

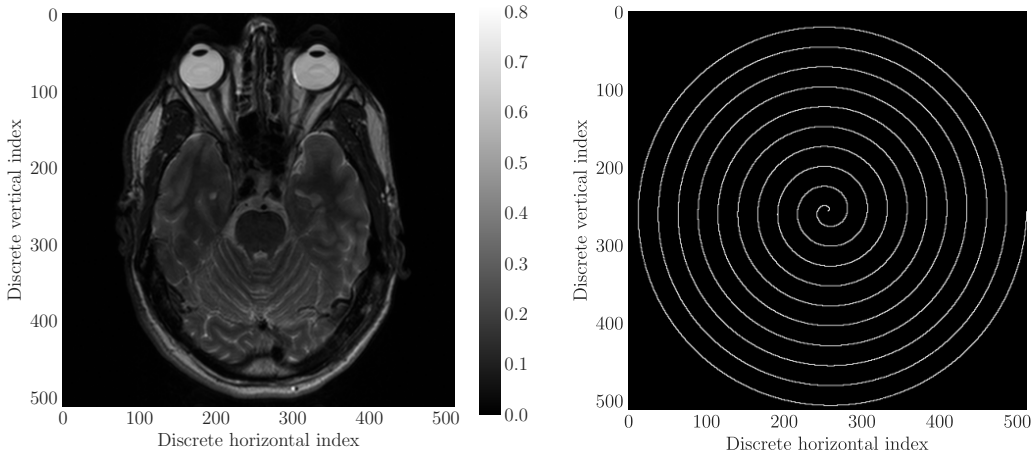

(a) 512 × 512 MR image

(b) Spiral trajectory (10 turns)

Figure 2.5 – Example of MR image and the position of its measurements acquired in a spiral trajectory in the frequency plane.

2.2.3 Non-Uniform Fast Fourier Transform

The Filtered Back-Projection we presented as a reconstruction algorithm for CT can also reconstruct MR images if the samples are in radial lines[1]. In Magnetic Resonance, the available data for computing the image are samples of its content in the frequency domain. Due to the nature of the acquired measurements, algorithms based on the Fast Fourier Transform (FFT) are standard in the literature. If the samples are in a Cartesian trajectory, the image can be obtained directly using the FFT [28]. On the other hand, the samples usually do not coincide with the Cartesian positions for

[1]The Fourier Slice Theorem allows the computation of the projections from spectrum samples along a radial line.

different trajectories. Thus, some MR reconstruction algorithms perform two tasks: estimate the spectral data at the non-sampled positions and invert the image to the pixel domain.

The standard FFT algorithm presumes that the input coefficients are equispaced signal samples in the time domain to compute its Discrete Fourier Transform (DFT). Algorithms that allow the analysis of spectral components in non-equispaced positions should be adopted for reconstructing MR images when measurements are along non-Cartesian trajectories. Efficient algorithms that compute the Fourier Transform under these conditions are called Non-Uniform Fast Fourier Transform (NUFFT). Different strategies are possible in devising these algorithms. Among them are low-rank approximations and polynomial interpolations [29, 30].

The NUFFT algorithms are efficient procedures for computing the Fourier Transform in non-uniformly distributed points. As such, it is a commonly used tool in developing fast and accurate methods for reconstructing MR images. In general, NUFFT-based reconstruction algorithms perform the inversion of measurements from regridded data. These strategies differ mainly in terms of the type of interpolator. Examples of reconstruction methods implemented with NUFFT are presented in [31, 32].

2.3 Artificial phantoms

Artificial images are commonly used for preliminary assessment of the quality of results when developing reconstruction techniques. The algorithm proposed in [33] is tested with reconstructions of Figure 2.6. This testing image became known as the Shepp-Logan phantom and is often used in studies that design and evaluate algorithms for medical image reconstruction.

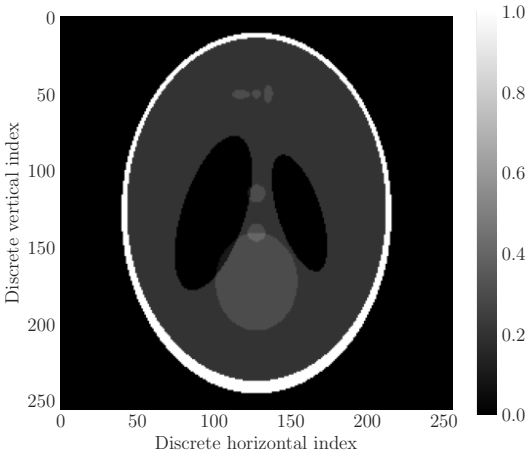

Figure 2.6 – The 256 × 256 Shepp-Logan phantom.

Although models such as the Shepp-Logan phantom allow initial evaluation of the performance of new methodologies in medical imaging, they consist of relatively simple structures. In light of this, there are efforts to develop more sophisticated artificial phantoms that exhibit anatomical structures in a more realistic representation [34]. Methodologies to create more complex phantoms represent relevant contributions to the validation process of medical imaging technologies. However, as indicated in [34], it is still necessary to improve these techniques to cover a broader population diversity and develop more specific and detailed models for more parts of the human body.

The tests developed in the present study conducted reconstructions of three groups of testing images: (i) the Shepp-Logan phantom, (ii) synthetic images with characteristics desired by the proposed algorithm (see Section 5.5), and (iii) actual images available in open databases, as means of looking for evaluating the reconstruction quality for images with more complex structures.

Chapter 3

Theoretical Foundations of Compressive Sensing

Many of modern life's daily activities are carried out using digital computation. Technologies based on digital signal processing theory are diverse, such as mobile communication, weather forecasting, industrial process automation, classification algorithms, medical diagnosis aids, etc. A common feature of many of these applications is that they rely on information available in the environment. Representing the information from physical quantities as discrete signals is a key task for engineering. In this sense, the Nyquist-Shannon sampling theorem is a milestone in the digital signal processing theory since it lays the foundations for the sampling techniques [35, 36].

Sampling is the process of obtaining a discrete representation of a signal that is initially on a continuous domain. The Nyquist-Shannon sampling theorem states a sufficient, but not necessary, condition to guarantee that a uniform sampling scheme preserves the information of a bandlimited continuous signal on the resulting discrete sequence. For that, the adopted sample rate should be at least two times the highest frequency of the continuous signal. The acquisition of signals using a sample rate below the Nyquist-Shannon criterion is possible, but other conditions must be established.

The Compressive Sensing theory uses sparsity to design acquisition systems that are more efficient in the sense of the number of entries required to represent the information. While the idea behind the sampling theorem is to get enough time samples to recover the original continuous signal, CS looks for linear measurements and exploits redundancy to acquire compressively the information into the continuous signal [12, 13]. In this context, sparsity is a property related to a signal's number of null components (more null values mean greater sparsity). This Chapter will present the basics of CS theory, as well as examples of algorithms and how they can be used to reconstruct medical images.

3.1 The basics of Linear Algebra for Compressive Sensing

A matrix $M \in \mathbb{K}^{m \times n}$ represents a linear relationship between two vector spaces of dimensions m and n. Throughout the text, we will use the symbol $\mathbb{K}$ to denote that the number set can be either real ($\mathbb{R}$) or complex ($\mathbb{C}$), depending on the application context. The product of this matrix M by a vector $x \in \mathbb{K}^n$ gives another vector $b \in \mathbb{K}^m$ that is a linear combination of the n columns of M. Therefore, the matrix M provides a mapping between the sets $\mathbb{K}^m$ and $\mathbb{K}^n$, and the product $Mx = b$ can be understood as the system of linear equations that establishes how this linear map is calculated. Solving a linear system is to calculate a vector x that satisfies the set of equations $Mx = b$ once the matrix M and the result b are known. The set of possible solutions for the system can be described by studying the linear dependency of the rows and columns of M.

Suppose an acquisition system modeled by the matrix M that relates the signal x properly acquired according to the sampling theorem with a set of measurements $b = Mx$. There is special interest in situations where M establishes a bijection between the vector spaces, that is, $Mx_1 = Mx_2$ implies $b_1 = b_2$ and every vector in $\mathbb{K}^m$ is mapped to $\mathbb{K}^n$ by M. This property guarantees that the information contained in a vector of $\mathbb{K}^m$ is preserved in $\mathbb{K}^n$ and that we can exactly recover x from b. This occurs, for instance, with invertible linear transforms such as the Discrete Fourier Transform.

In particular, CS aims to reduce the number of measurements required to represent information. With this, the acquisition process is modeled as underdetermined linear systems that map the original signals to lower-dimensional spaces. This assumption considers that there are redundancies in the signal and that they can be exploited in a compressive acquisition scheme. The problem that arises when solving underdetermined systems is that such systems are not a bijection and thus potentially have infinite solutions. The CS approach is to constrain the domain of the linear mapping by searching for the solution that is the sparsest in a transformed domain.

3.1.1 Sparsity and ℓ_p metrics

Looking over the Compressive Sensing theory from the point of view of Linear Algebra, "reconstructing a signal" is to calculate the sparsest vector from a vector of a smaller dimension once the linear map between them is known. CS is concerned with solving underdetermined linear systems by finding the sparsest solution. . The sparsity of a vector is a key concept for CS. A vector $x \in \mathbb{K}^n$ is called k-sparse if at least k of its entries are non-zero values. The set $\Omega_x = \{i \mid x[i] \neq 0\}$ is called the support of x.

In the present text, we will assume that a metric for a vector space V, denoted

by $\|\cdot\|$, is a function that associates a non-negative real value to a vector $x \in V$. In the context of CS, once the ℓ_p metrics (Definition 3.1) can be a parameter to evaluate the sparsity of a signal, we have a particular interest in them. Metrics that satisfy the following special conditions are called norms:

- $\|x\| = 0 \Leftrightarrow x$ is the null vector of V
- Homogeneity: for $\alpha \in \mathbb{R}$, $\|\alpha x\| = |\alpha|\|x\|$
- Triangle inequality: $\|x_1 + x_2\| \leq \|x_1\| + \|x_2\|$

Definition 3.1 (ℓ_p metric) Let $x = x[k]$ a vector in $\mathbb{R}^N$ and $p \in \mathbb{R}\backslash\{0\}$, the length of x calculated by an ℓ_p metric is given by

$$\|x\|_p = \left(\sum_{k=0}^{N-1} |x[k]|^p \right)^{\frac{1}{p}} . \tag{3.1}$$

For $p = 0$, the ℓ_0 metric is given by

$$\|x\|_0 = \lim_{p \to 0} \sum_{k=0}^{N-1} |x[k]|^p . \tag{3.2}$$

If $p \geq 1$ the ℓ_p metric is also a norm.

The ℓ_0 metric behaves by counting the number of non-zero entries in the vector x once the limit of $|x[k]|^p$ as $p \to 0$ is equal to zero for $x[k] = 0$ and it is equal to one otherwise. Thus, the sparser a signal, the lower its ℓ_0 norm [37].

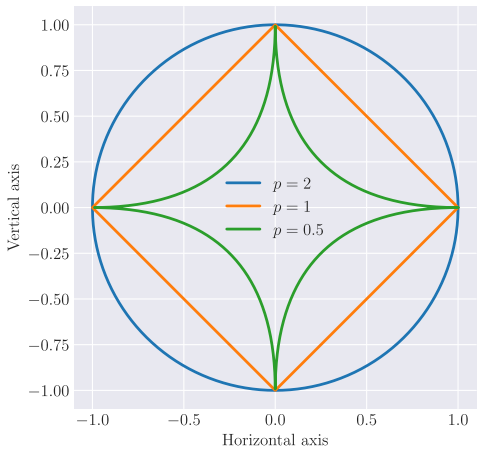

Figure 3.1 – Geometrical representation of some two-dimensional unit ℓ_p balls.

We can see in Figure 3.1 a geometric representation of the unit ℓ_p balls in $\mathbb{R}^2$ for some values of p. These curves are the set of vectors $x \in \mathbb{R}^2$ such that $\|x\|_p = 1$.

Observing these two-dimensional ℓ_p balls can be a simplified way of illustrating what CS algorithms pursue when calculating the solution. In a given linear system $Mx = b$, the matrix M defines a locus that contains all possible solutions. The reconstruction algorithm will search among all solutions for the one with the lowest ℓ_p metric. In the two-dimensional case, the set of solutions defines a straight line in the plane, and the CS solution is the common point between this line and the ℓ_p ball of the smallest radius that intercepts it.

Note that as p goes to zero, the ball gets closer to the axes, so the ℓ_p norms ($0 < \ell_p \leq 1$) will also find the sparsest solution for a wide variety of solution sets defined by the undetermined linear system. From now on, we will concern with formally defining the minimization problem behind CS and the conditions in which the ℓ_p norms are an adequate criterion for evaluating the sparsity of the signal to be reconstructed.

3.2 The sparse reconstruction problem

The Compressive Sensing theory deals with the acquisition systems in which there is a linear relationship between the acquired signal $x \in \mathbb{K}^N$ and its corresponding measurements $b \in \mathbb{K}^m$ that is available for recovery. Furthermore, it is assumed that the dimension of the signal is greater than the dimension of the measurements ($m < N$), i.e., the acquisition system can be modeled as an underdetermined linear system given by

$$Mx = b, \tag{3.3}$$

where $M \in \mathbb{K}^{m \times N}$ is called the measurement matrix. Thus, b does not form a bijection with the signal x. It occurs since distinct signals can provide the same measurements once the matrix representing the acquisition process has linearly dependent columns. Consequently, this kind of system has no solution or infinitely many solutions. Hence, a restriction is necessary to ensure the reconstruction algorithm can calculate a unique appropriate solution from the measurements b [13].

From the perspective of a minimization problem, defining a constraint to calculate the solution of an underdetermined linear system means choosing a cost function. Thus, solving this problem is to select among all the infinite solutions the one that returns the lowest value when applied to the cost function [37]. The minimization criterion adopted in the Compressive Sensing theory is sparsity. The CS solution for an underdetermined system is the signal x that satisfies the linear relationship (Equation 3.3), whose most entries are null. In this sense, the sparser the signal is, the fewer coefficients are required to represent the information.

There are situations where the class of the signals of interest does not meet the sparsity criterion. However, the Compressive Sensing algorithms can still be used as long as there is a transformed basis in which the signals of interest are sparse. In other words, the signal x is expected to have a sparse representation $\hat{x} = Tx$ under the linear transform $T \in \mathbb{K}^{N \times N}$. By defining the acquisition matrix as $A = MT^{-1}$, Equation 3.3 can be rewritten in terms of the sparse signal $\hat{x}$ as

$$A\hat{x} = b. \tag{3.4}$$

In order to formally define the CS minimization problem, the question that arises is: What are the possible cost functions that are a good metric for sparsity? As discussed in Section 3.1.1, the ℓ_0 metric counts the number of non-zero entries of the given vector, and therefore, at first glance, it seems to be an intuitive way to measure the sparsity of a vector [37]. Given this, the CS problem can be expressed in terms of the ℓ_0 metric as

$$\min_{\hat{x}} \|\hat{x}\|_0 \text{ subject to } A\hat{x} = b. \tag{3.5}$$

Suppose the support of the signal Ω is known. In that case, the solution can be trivially calculated by Least-Squares, because the problem can be reduced to either a determined or overdetermined system [37, 38]. In the case where there is no information about the support, this problem can lead to NP-hard complexity [13]. For instance, the ℓ_0 minimization problem can be tackled by an algorithm that tries to solve the linear system for all the possible combinations of support until the desired solution is found. Thus, this strategy may require prohibitive times for reconstructing larger signals in practical applications.

A first possible approach, instead of searching exhaustively for the support, is the greedy algorithms. The idea is to approximate the sparsest solution by improving the estimation of the support iteratively. Relaxing the ℓ_0 metric is a second alternative to make the minimization problem computationally tractable. In this sense, an ℓ_p metric with $0 < p \leq 1$ can be used as the cost function for the minimization problem [37]. This relaxed version of the problem is stated as

$$\min_{\hat{x}} \|\hat{x}\|_p^p \text{ subject to } A\hat{x} = b. \tag{3.6}$$

At first, the researchers had a special interest in ℓ_1 minimization because of the convexity of the problem. This optimization principle is commonly referred to as Basis Pursuit. This framework lays the foundation for developing convex algorithms for

solving the ℓ_1 minimization problem using a linear programming solution [39]. However, adopting $p \in (0, 1)$ has theoretical advantages, such as the possibility of reducing the number of measurements and the computation time [40, 17].

It is noteworthy that the performance of algorithms can be enhanced as more information is available to estimate the support of the solutions. Similarly, the quality of the results is related to the reliability of the model designed to represent the acquisition system and the sparse domain.

3.3 Conditions for sparse reconstruction

Although we have a formal definition for the problem of finding the sparsest solution of an underdetermined linear system $A\hat{x} = b$, we still need to look for the conditions that ensure the sparsest solution exists and is unique. In this sense, criteria that assess the matrix A to provide parameters on the relationship between sparsity and the number of measurements required for the reconstruction are necessary to describe the scenarios in which the CS algorithms apply.

The Mutual-Coherence (Definition 3.2) is an index that analyzes the linear dependence of the columns of a given matrix. This property is used to calculate the sparsity that guarantees the signals to be uniquely recovered by ℓ_0 minimization. So, the Mutual-Coherence relates the maximum number of non-null entries in the solution to the structure of the matrix that models the linear system to be solved.

Definition 3.2 (Mutual-Coherence) Take $A \in \mathbb{K}^{n\times m}$ and define $\tilde{A}$ as the matrix whose columns $\tilde{a}_1, \ldots, \tilde{a}_m$ are the ℓ_2-normalized versions of the columns of the matrix A. The Mutual-Coherence $\mu(A)$ is the maximum absolute value of the dot product between two distinct columns $\tilde{a}_i$ and $\tilde{a}_j$.

$$\mu(A) = \max_{1\leq i,j\leq m;\ i\neq j} |\tilde{a}_i^H \tilde{a}_j| \tag{3.7}$$

Equivalently, the Mutual-Coherence $\mu(A)$ is the highest absolute off-diagonal value in the Gram matrix $G = \tilde{A}^H \tilde{A}$.

Recall that the dot product measures the relative direction of two vectors. In this term, the Mutual-Coherence index is associated with the maximum angular distance between two distinct column-vectors of a given matrix A. Suppose that the columns of A form an orthogonal set, then $\mu(A) = 0$. Furthermore, the maximum value for the Mutual-Coherence $\mu(A) = 1$ occurs if at least two columns of the A are vectors in the same direction. Thus, higher values of Mutual-Coherence are achieved by matrices

whose columns are more similar to each other. On the other hand, the smallest Mutual-Coherence possible for non-orthogonal matrices occurs if the angle between each pair of columns in the matrix is the same.

In [37], Elad introduces the idea of Mutual-Coherence as a criterion to evaluate the uniqueness of the sparsest solution from an analysis of the null-space of A. This reasoning starts by defining the spark of a matrix as the smallest number of columns of this matrix that can be selected to form a linearly dependent set. Then suppose there is a non-null vector $y \in \mathbb{K}^n$ in the null space of A. Denoting the columns of A by $a_1, a_2, \cdots, a_n$ and the support of y by Ω_y, the following equation is valid

$$Ay = \sum_{i=1}^{n} y[i]a_i = \sum_{i \in \Omega_y} y[i]a_i = 0. \tag{3.8}$$

Thus, the subset $\{a_i | i \in \Omega_y\}$ of columns of A is linearly dependent. By the definition of spark, if $|\Omega_y| < spark(A)$, there is no non-zero vector y that satisfies the Equation 3.8 and therefore

$$\|y\|_0 \geq spark(A). \tag{3.9}$$

We can use this inequality to relate the spark of A to the sparsity of possible solutions to the underdetermined system. To do so, let's take $\hat{x}_1$ and $\hat{x}_2$, two distinct solutions for the underdetermined system $A\hat{x} = b$. Notably, the difference $\hat{x}_1 - \hat{x}_2$ is a non-null vector in the null-space of A. Recall that the triangle inequality holds for the ℓ_0 metric, although it is not a norm. So, taking into account the Equation 3.9, we have that

$$\|\hat{x}_1\|_0 + \|\hat{x}_2\|_0 \geq \|\hat{x}_1 + \hat{x}_2\|_0 \geq spark(A). \tag{3.10}$$

This inequality provides the first parameter to evaluate the uniqueness of the CS solution. Note that if $\|\hat{x}_1\|_0 < \frac{1}{2}\, spark(A)$, there is no other solution with fewer non-zero entries; therefore, the sparsest solution will be unique [37]. Some authors call this criterion Null Space Property (NSP). The next step is to extend this spark-based criterion to include the Mutual-Coherence index. It is usually proved by using the Gershgorin Disks Theorem stated below.

Theorem 3.1 ***Gershgorin Disks Theorem***

Take the matrix $A = [a_{ij}] \in \mathbb{K}^{n \times n}$. There is a Gershgorin disk $D_i(c_i, r_i)$ in the complex plane associated to each row of A. The i-th disk is centered at $c_i = a_{ii}$ with the radius equal to $r_i = \sum_{j \neq i} |a_{ij}|$, which is the sum of the absolute off-diagonal values of this i-th row.

All eigenvalues of A lie within the union of all Gershgorin disks of this matrix.

The Gershgorin Disks Theorem establishes a lower bound to the spark of a matrix A by doing a worst-case scenario analysis of the linear dependency of all possible subsets of p columns of A through the eigenvalues of a corresponding Gram matrix. To obtain this lower bound, we start by creating a matrix $\tilde{A}$ whose columns are the ℓ_2-normalized versions of the columns of matrix A [37]. This operation preserves the direction of the column vectors. So, it does not affect the columns' linear dependence or the matrix's spark. In other words, $spark(A) = spark(\tilde{A})$, $rank(A) = rank(\tilde{A})$, and $\mu(A) = \mu(\tilde{A})$.

Let Ψ_k be a set of k column vectors of $\tilde{A}$ and $\tilde{A}_{\Psi_p}$ be a submatrix of $\tilde{A}$ obtained by selecting only the columns in Ψ_k. Then we create a Gram matrix $G_{\Psi_k} = \tilde{A}^H_{\Psi_k}\tilde{A}_{\Psi_k}$. Once the columns of $\tilde{A}$ are ℓ_2-normalized, all the elements in the main diagonal of G_{Ψ_k} are equal to 1. Consequently, all of its Gershgorin disks are centered in 1. Moreover, $\mu(A)$ is the highest off-diagonal absolute value in G_{Ψ_k}, so the maximum possible value for the radius of the disks is given by

$$r_{i(max)} = (k-1)\mu(A). \tag{3.11}$$

As a consequence of its definition, the Gram matrix G_{Ψ_k} will be at least positive semidefinite, and it will be strictly positive definite if zero is not one of its eigenvalues. Thus, G_{Ψ_k} being positive definite means that the set Ψ_k is linearly independent. According to the Gershgorin theorem, for a given Gram matrix to be positive definite, it is sufficient that for each disk D_i, the radius r_i to be less than the magnitude of its center c_i. This condition guarantees that zero is outside all disks and cannot be one of the eigenvalues of this Gram matrix [37]. Writing this condition for G_{Ψ_k} we have that for every row i

$$r_i < 1. \tag{3.12}$$

The Equations 3.11 and 3.12 produce a sufficient condition to guarantee that every combination of k columns of A will be a linearly independent set. In this sense, we have that

$$r_{i(max)} < 1 \tag{3.13}$$

$$(k-1)\mu(A) < 1 \tag{3.14}$$

$$k < 1 + \frac{1}{\mu(A)}. \tag{3.15}$$

This last inequality implies that the smallest value of k for which there might be some set Ψ_k that is linearly dependent is $k = 1 + \frac{1}{\mu(A)}$. Thus,

$$spark(A) \geq 1 + \frac{1}{\mu(A)}. \tag{3.16}$$

Now we have a lower bound to $spark(A)$ as a function of $\mu(A)$. At last, to establish a condition for uniqueness, we need to relate the Mutual-Coherence to the ℓ_0-metric of distinct possible solutions. To achieve this, combine the inequalities the inequalities 3.10 and 3.16 as

$$\|\hat{x}_1\|_0 + \|\hat{x}_2\|_0 \geq 1 + \frac{1}{\mu(A)}. \tag{3.17}$$

This leads to the criterion stated as Theorem 3.2.

Theorem 3.2 ***Uniqueness by Mutual-Coherence***

Let $A\hat{x} = b$ be an underdetermined linear system with a known solution $\hat{x}_s$. If

$$\|\hat{x}_s\|_0 < \frac{1}{2}\left(1 + \frac{1}{\mu(A)}\right), \tag{3.18}$$

then this is the sparsest solution possible.

In summary, the Mutual-Coherence gives an upper bound for the spark of a matrix, which in turn concerns the total of the non-zero elements in two different solutions of the underdetermined linear system. With this, we can define a threshold that guarantees that the solution that has the ℓ_0 metric smaller is the sparsest and is unique. An alternative way to illustrate how the Mutual-Coherence evaluates uniqueness is by understanding the off-diagonal entries of $\tilde{A}^H\tilde{A}$ as disturbances in the estimation of the support of the solution [38]. An analysis of the maximum values of these perturbations so that the support positions can still be detected also leads to Equation 3.18. However, it does not prove rigorously Theorem 3.2 [38].

Indeed, the Mutual-Coherence $\mu(A)$ measures how close the behavior of the linear map described by A is to an orthonormal matrix [37]. In this sense, another sufficient criterion concerning the matrix A that can guarantee that it is possible to reconstruct signals from a reduced number of measurements by solving a ℓ_0 or ℓ_1 optimization problem is the Restricted Isometry Property (RIP). Candès introduced this notion in [41] and [42]. The Restricted Isometry Constant (Definition 3.3) is a necessary concept concept to state the RIP criterion.

Definition 3.3 (Restricted Isometry Constant - RIC) Let be the matrix $A \in \mathbb{K}^{m \times N}$, its Restricted Isometry Constant of order k is the smallest positive number δ_k such that, for all k-sparse vector $\hat{x}$,

$$(1 - \delta_k)\|\hat{x}\|_2^2 \leq \|A\hat{x}\|_2^2 \leq (1 + \delta_k)\|\hat{x}\|_2^2. \tag{3.19}$$

Like the Mutual-Coherence index, the Restricted Isometry Constant also reflects the linear dependence of the column vectors of the acquisition matrix. Moreover, both properties characterize the null-space of A by analyzing its singular values to ensure the uniqueness of the sparsest solution. However, in contrast to the Mutual-Coherence that considers pairs of columns (recall the Definition 3.2), the calculation of δ_k covers all possible combinations of k columns [13]. While this indicates that RIP may be a more robust condition, it also means that its calculation is more complex. The complexity of computing the RIP is comparable to that of the ℓ_0 minimization [37, 43].

If $\delta_k < 1$, the inequality that defines the RIC establishes a narrow range in which the energy (ℓ_2 norm) of the vector will vary after the linear transformation [37]. A property observed in orthogonal matrices is that the energy of a vector is preserved through linear mapping. The matrices used to model the acquisition schemes in the CS approach cannot be orthogonal; however, this property is convenient since it is related to the bijectivity of the matrix [13]. The idea of using the RIC as a criterion for uniqueness is based on providing a maximum value for the δ_{2k} for which the "near-orthonormal" behavior of the acquisition matrix guarantees that there is a unique k-sparse vector recoverable through the CS approaches [13, 37]. It puts us in a position to state the RIP criterion for uniqueness using the bound established by Candès.

Theorem 3.3 ***Uniqueness by Restricted Isometry Property***

Let δ_{2k} be the restricted isometry constant of the matrix $A = MT^{-1}$. The ℓ_1 minimization problem (Equation 3.6 taking $p = 1$) has a unique k-sparse solution if

$$\delta_{2k} < \sqrt{2} - 1. \tag{3.20}$$

Furthermore, the solution for the ℓ_1 and ℓ_0 minimizations are equivalent.

Theorem 3.3 states the RIC bounds for the ℓ_1 minimization general case. Specific studies can lead to different bounds for settings in which more information is available about the acquisition matrix or the reconstruction algorithm. It emphasizes that RIP

is also a worst-case criterion and, therefore, not a necessary condition for uniqueness. A compilation of some RIP analyses for the most common classes of CS algorithms is available at [13]. Note that Theorem 3.3 gives the RIC bounds to ensure the uniqueness of the solution of the ℓ_1 minimization. Further studies such as [40, 44, 45] expanded the RIP conditions for the ℓ_p with $p \in (0, 1]$ scenarios since these minimization cost functions potentially enlarge the group of matrices suitable for modeling CS acquisition schemes [43].

In particular, [45] describes the bounds for RIC as a function of two variables: $p \in (0, 1]$, referring to the metric adopted in the minimizer; and $t \in (1, 2]$, referring to the order of the constant δ_{tk}. So, the problem in Equation 3.6 has a unique solution if there is a combination of p and t such that

$$\delta_{tk} < \frac{\eta}{\frac{2-p}{t-1} - \eta}, \tag{3.21}$$

where η is the unique positive solution of

$$\frac{p}{2}\eta^{\frac{2}{p}} + \eta - \frac{2-p}{2(t-1)} = 0. \tag{3.22}$$

The RIP also allows the extension of the uniqueness discussion to stability when some random noise $\xi \in \mathbb{K}^n$ corrupts the measurements [37]. In this scenario, it is assumed that the noise energy $\|\xi\|_2 = \epsilon > 0$ is finite, and so the ℓ_p minimization problem (Equation 3.6) is rewritten as

$$\min_{\hat{x}} \|\hat{x}\|_p^p \text{ subject to } \|b - A\hat{x}\|_2 \leq \epsilon. \tag{3.23}$$

This new formulation addresses real-world applications better. But now, instead of a unique solution, a region of solutions close to the acquired signal $\hat{x}$ satisfies the problem. With this, a small enough RIC ensures that the set of feasible solutions will not include signals that are sparser than $\hat{x}$ [37]. The bounds for RIC stated in Theorem 3.3 guarantee the stability of the noisy ℓ_1 minimization problem [42]. Theorems that address the RIP conditions for ℓ_p minimization in [45] comprise noiseless and noisy cases.

In conclusion, the RIP and Mutual-Coherence provide us with parameters to infer from the structure of the acquisition matrix whether the degree of undersampling still allows the reconstruction given a maximum expected sparsity for the signals of interest. These conditions guarantee the exact recovery in noiseless scenarios; and stable recovery in noisy settings. However, although these properties are essential theoretical tools, they are sufficient conditions but not necessary. In other words, some matrices do not

meet the RIP and Mutual-Coherence criteria that can still model acquisition systems whose signals can be successfully recovered with CS algorithms. Theorems 3.2 and 3.3 (and alternative formulations) are widespread theoretical criteria for uniqueness. Despite this, more recent studies have sought new paradigms to evaluate sparsity and find other conditions that can lead to a broader class of acquisition matrices that ensure the reconstruction with CS techniques [46].

3.4 An interpretation of CS from Linear Algebra

The reconstruction of a signal acquired by a scheme based on CS is done through the solution of a given underdetermined linear system. We have presented the theory by modeling the problem from the optimization perspective. The recovery algorithms search for the most appropriate solution by minimizing a cost function that measures sparsity. The Mutual-Coherence and the Restricted Isometry Property are theoretical tools related to the linear dependency of the columns of the matrix A that can be used to evaluate the existence and uniqueness of the sparsest solution [37, 38].

The Compressive Sensing problem arises because the acquisition process is modeled by underdetermined linear systems that do not establish a bijection between the measurements and the desired vector. Thus, the reconstruction can't be done by simply calculating the inverse of the acquisition matrix, which would be possible if the operator was a bijection. When an appropriate cost function is defined to solve the system through minimization, the set of solutions is restricted to a unique solution, and an "artificial bijection" establishes. Therefore, the acquisition matrix A will behave under the CS reconstruction algorithm as a bijection between the measurements b and the k-sparse signals $\hat{x}$ with a constrained domain for $k < \frac{1}{2}(1+1/\mu(A))$ in the general case. Note that each algorithm may have specific conditions for uniqueness and convergence. Section 3.3 covered general criteria for ℓ_p minimization approaches without specifying an algorithm.

Assuming that the signals of interest are redundant, the criteria we presented guarantee it is possible to define a vector subspace embedded in the domain of A for which the solution to $A\hat{x} = b$ is unique. However, these criteria alone do not guarantee whether the subspace of the sparsest solutions will contain the signals of interest. Hence the importance of ensuring that the signals of interest have an optimal representation on the sparse domain according to the criterion evaluated by the cost function. Figure 3.2 summarizes this Linear Algebra interpretation of Compressive Sensing.

Recall that $A = MT^{-1}$ concerns the measurement scheme (M) and the sparsifying transform (T). While modeling the reconstruction problem, these two matrices must be

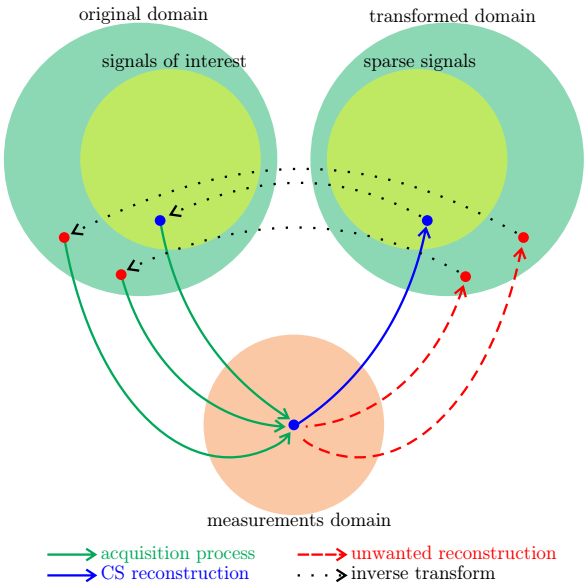

Figure 3.2 – Venn diagram summarizing the Compressive Sensing acquisition and reconstruction processes.

appropriately designed to ensure that the signals of interest are those with the intended sparsity in the transformed domain. Moreover, each cost function generates a different one-to-one correspondence between the measurements and the recovered signal. Thus, the chosen algorithm must establish the desired inverse relationship between these two sets. From this point of view, the "artificial bijection" depends on both the acquisition process and the reconstruction method. The Moore-Penrose generalized inverse that gives the standard Least Squares solution,

$$A^{\dagger} = (A^H A)^{-1} A^H, \tag{3.24}$$

is a well-known example of constraining the linear system solutions to get a specific "artificial bijection." The ℓ_2 minimum solution is easily computed as $x_{\ell_2} = A^{\dagger} b$. However, the CS problem deals with ℓ_p minimizations for some $p \in (0, 1]$, with no known closed solution.

3.5 Compressive Sensing algorithms

There are several algorithms available for signal reconstruction using CS. The choice of which one to use for each possible application can take into account different criteria: computational complexity, quality of reconstruction in terms of error, robustness to noise, memory usage during execution, and other factors. Comparisons of the performance of some algorithms can be found in [47]. In this section, as an example, we will present two CS reconstruction techniques: the Orthogonal Matching Pursuit (OMP),

which follows a greedy strategy, and the Iteratively Reweighted Least Squares (IRLS), a non-convex minimization algorithm.

3.5.1 Orthogonal Matching Pursuit

The greedy strategy is to approximate the sparsest solution iteratively. The algorithm begins with an estimate for the solution and for the support ($\Omega = \varnothing$ if there is no prior information). At each iteration, a new element is added to the support, and the solution is updated, minimizing the ℓ_2 error. The algorithm continues until some stopping condition is met [37].

Thus, broadly speaking, each iteration k comprises two main steps: selecting a new position to be added to the support Ω and the computation of a new estimate $\hat{x}_k$. The support update step determines which position will be added to the support set by using the residual value of the last iteration r_{k-1}. This residue is the part of the measurements that are not well represented by the last estimate $\hat{x}_{k-1}$.

The goal is to find which of the columns a_i of A is the vector that has the direction closest to the direction of the last residue. Let us consider the case where a_i is parallel to r_{k-1}. It means that there is a scalar $z_i \in \mathbb{K}$ such that

$$\begin{aligned} a_i z_i &= r_{k-1} && (3.25)\\ a_i^H a_i z_i &= a_i^H r_{k-1} && (3.26)\\ \|a_i\|_2^2 z_i &= a_i^H r_{k-1} && (3.27)\\ z_i &= \frac{a_i^H r_{k-1}}{\|a_i\|_2^2}. && (3.28) \end{aligned}$$

So, the position to be added to the support in the iteration k is the one with the smallest error

$$\epsilon_k(i) = \|a_i z_i - r_{k-1}\|_2, \tag{3.29}$$

where z_i is given by Equation 3.28. The support Ω_k is updated with

$$\Omega_k = \Omega_{k-1} \cup \{i | \arg\min \epsilon_k(i)\}. \tag{3.30}$$

The new estimate $\hat{x}_k$ is given by the Least Squares solution

$$\hat{x}_k = (A_{\Omega_k}^H A_{\Omega_k})^{-1} A_{\Omega_k}^H b, \tag{3.31}$$

where A_{Ω_k} is the submatrix of A obtained by selecting the columns corresponding to the positions in Ω_k. In the end, the residue r_k of the measurements b is calculated for the next iteration

$$r_k = b - A\hat{x}_k. \tag{3.32}$$

This procedure repeats until the ℓ_2 energy of the residual is below some predetermined tolerance *tol*. Algorithm 3.1 corresponds to the OMP.

Algorithm 3.1 Orthogonal Matching Pursuit.

Input: Acquisition matrix A; Measurements b; Residue tolerance *tol*; Initial estimation for the support set Ω_0
Output: Recovered signal (Approximated solution after k iterations)

```
Set the initial solution as a null vector x̂_0 = 0
Set the initial value for the residual r_0 = b
Set the initial value for the iterations counter k ← 0
while the residual energy is greater than the tolerance ||r_k||_2 > tol do
    for each column a_i (i ∉ Ω_k) of A do
        Calculate a scalar value z_i using Equation 3.28
        Calculate an error value ε_i using Equation 3.29
    end for
    Update the support set using Equation 3.30
    Update the solution x̂_k using Equation 3.31
    Update the residual r_k using Equation 3.32
    Update the iterations counter k ← k + 1
end while
```

3.5.2 Iteratively Reweighted Least Squares

The Iteratively Reweighted Least Squares, in contrast to the greedy strategies, models the sparse recovery from the perspective of an ℓ_p minimization problem. This method obtains the desired signal from successive Least Squares computations, taking the previous iteration's solution as weights to approximate the ℓ_p behavior [37, 48]. Thus, in the CS problem modeling, instead of solving the Equation 3.6, the solution is given by iteratively computing the weighed ℓ_2 norm,

$$\min \sum_{i=1}^{N} w_k[i]\hat{x}[i] \text{ subject to } A\hat{x} = b, \tag{3.33}$$

where $w_k \in \mathbb{K}^N$ is the weights vector at the k-th iteration [48]. Each entry $w_k[i]$of the w_k is updated with the solution $\hat{x}_{k-1}$ of the last iteration,

$$w_k = |\hat{x}_{k-1}|^{p-2} + \mu, \tag{3.34}$$

where $\mu > 0$ is a regularization term to improve the inversion of ill-conditioned matrices that might be necessary when computing $\hat{x}_k$. As discussed in [48], the performance of IRLS is improved if we adopt a relatively large value for μ in the first iterations and gradually decrease its value throughout the iterations.

If we define $Q_k \in \mathbb{K}^{N \times N}$ as a diagonal matrix with non-null entries w_k^{-1}, the estimate $\hat{x}_k$ at the current iteration is given by the standard Least Squares solution for Equation 3.33,

$$\hat{x}_k = Q_k A^H (A Q_k A^H)^{-1} b. \tag{3.35}$$

The regularization term μ is updated if the following convergence criterion is met,

$$\frac{\|x_k - x_{k-1}\|_2}{1 + \|x_{k-1}\|_2} < \frac{\sqrt{\mu}}{100}, \tag{3.36}$$

and the iterations are repeated until $\mu < \mu_{min}$. This stopping condition was proposed by [48]. The IRLS method is summarized in Algorithm 3.2

Algorithm 3.2 Iteratively Reweighted Least Squares.

Input: Acquisition matrix A; Measurements b; p; μ_{min}; maximum of inner iterations i_{max} before reducing μ
Output: Recovered signal

Set the initial solution as a null vector $\hat{x}_0 \leftarrow 0$
Set the initial value for the weights w_0 as a vector of ones
Set the counter for iterations $k \leftarrow 0$
while $\mu > \mu_{min}$ **do**
    while Equation 3.36 is not satisfied or i_{max} is not reached **do**
        Update the weights w_k using Equation 3.34
        Calculate the diagonal matrix Q_k
        Update the solution $\hat{x}_k$ using Equation 3.35
        Update the iterations counter $k \leftarrow k + 1$
    end while
    Update the regularization parameter $\mu \leftarrow \mu/10$
end while

3.6 Compressive Sensing for medical imaging reconstruction

The structure presented in this work for reconstructing medical images with CS algorithms using direct matrix calculations is based on the method proposed for MR images in [49]. This paper introduces an alternative for handling the sparsity representation of two-dimensional signals called prefiltering. Later, [9] presented a Fourier Slice Theorem-based approach that expanded the results to CT and PET images. The

first results for CT using these techniques and direct methods were published in [50].

In outline, part of the strategy consists in treating the image as a vector for the minimization process. To this end, the measurements available for reconstruction are expected to be samples of the spectral coefficients of the desired image arranged as a column vector. So, the minimization problem is formulated as in Equation 3.6. It allows the use of the CS algorithms described in the previous section. The result will be a column vector corresponding to stacked pixels. To obtain the image, it is a matter of rearranging the vector in the form of a matrix.

3.6.1 Prefiltering

Prefiltering is a technique to represent medical images sparsely instead of defining a sparsifying transform. This approach expects the measurements to be samples of the image Fourier spectrum. Then it is possible to filter such measurements before running the reconstruction CS algorithm to recover a partial image that is sparse in the pixel domain. However, this filtered version of the image does not have the complete information we would like to recover. The final image is composed by appropriately selecting the coefficients of partial images recovered from different filtered versions of the measurements [49, 9]. Figure 3.3 illustrates a generic reconstruction scheme with prefiltering. On the left, the white pixels represent the positions where acquired measurements are in the Fourier spectrum. The output is the recovered image.

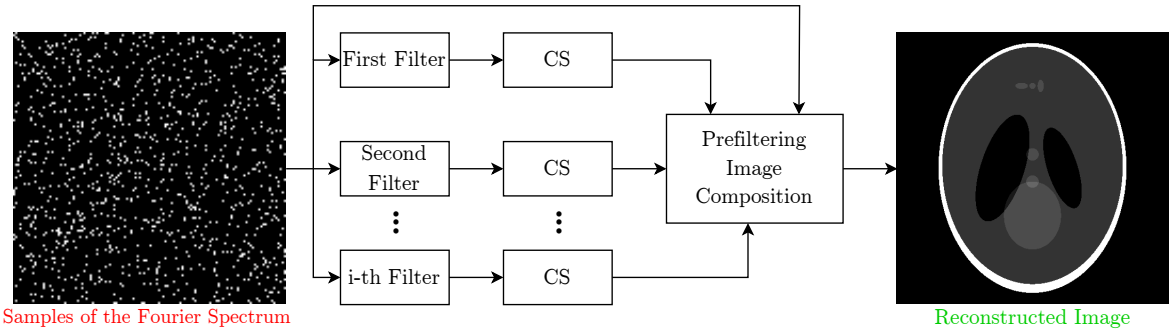

Figure 3.3 – General prefiltering scheme.

Each set of filters generates a different sparse representation. Thus, the choice of which filters are used and how many of them affects the quality of the reconstructions. The filtered versions of the image and the measurements are used in the composition step to form the final image. This procedure, proposed in [49], is detailed below:

1. The algorithm starts by creating a null matrix in the frequency domain;
2. The entries in this matrix at positions with acquired samples are filled with the values of the respective measurements;

3. We select for each remaining entry the partial reconstruction related to the filter that has the higher gain in the frequency of the specific position. Then the entry is filled in with the spectral content of the selected sparsified image divided by the correspondent filter coefficient;

4. This last matrix has the spectral information from the initial measurements and the filtered images. Finally, the recovered image is obtained by computing the Inverse Fourier Transform of this resulting matrix.

3.6.2 From sinogram projections to measurements in the frequency plane

The strategy to reconstruct medical images we have described relies upon measurements as samples in the frequency domain. For CT images, whose measurements are acquired as a sinogram, an intermediate step must be executed before the reconstruction to arrange the measurements as expected. That is, to reconstruct the image, samples of its Fourier Transform should be estimated from the sinogram. The approach we used in our computational experiments is an adaption from work in [9] and is summarized in Algorithm 3.3.

The Fourier Slice Theorem (2.1) sets the basis for this procedure: the 1D Fourier Transform of each column of the sinogram gives the coefficients of the 2D Fourier Transform of the image over radial lines at the corresponding angles. First, it is necessary to choose the grid that will be used to represent the discrete positions in the frequency plane. Then, we define which of these positions will be considered as belonging to the sampled radial lines.

Algorithm 3.3 Calculation of measurements in frequency plane from sinogram.

Input: Sinogram; Positions in which there is a measurement
Output: Measurements in the frequency domain (Cartesian grid)

1: Compute the missing projections by 2D interpolation
2: **for** each position on the Cartesian grid that corresponds to a measurement **do**
3: Calculate the angular coordinate of the position (it indicates which projection should be used to calculate the measurement)
4: Calculate the radial coordinate of the position (it indicates which frequency of the Fourier Transform of the projection should be calculated)
5: Calculate the desired measurement as a single sample of Discrete-Time Fourier Transform of the estimated projection
6: **end for**

The positions on the grid will not necessarily coincide with the angles of the acquired projections.Therefore, it is necessary to interpolate the sinogram columns to estimate the projections at the angles required by the chosen grid. Finally, the frequency domain measurements are obtained from the Fourier Slice Theorem by computing the Fourier

Transform of the projection at the specific frequency of each position [9]. The frequency measurements were calculated on a Cartesian grid with equally spaced samples for the simulations we carried out.

3.6.2.1 Defining the radial lines on the Cartesian grid

To define which positions of the Cartesian grid belong to the radial lines, we proceed as follows. For each angle θ_p that has an acquired projection, we observe every grid entry. Those positions with an angular coordinate θ_c close to θ_p are considered part of the radial line.

A tolerance value is needed to determine more accurately what it is "to be close". In this way, positions that have an angular coordinate θ_c are considered as belonging to the Cartesian radial lines if there is some θ_p such that the following inequality holds

$$|\theta_p - \theta_c| < \frac{tol}{r_c + \epsilon}, \tag{3.37}$$

where tol is the tolerance, r_c is the radial coordinate of the position in the Cartesian grid, and ϵ is a small value added to r_c to avoid division by 0. We have adopted $\epsilon = 10^{-3}$ in all of our experiments. Figure 3.4 shows 16 equiangular radial lines on the 512×512 Cartesian grid obtained for different values of tolerance.

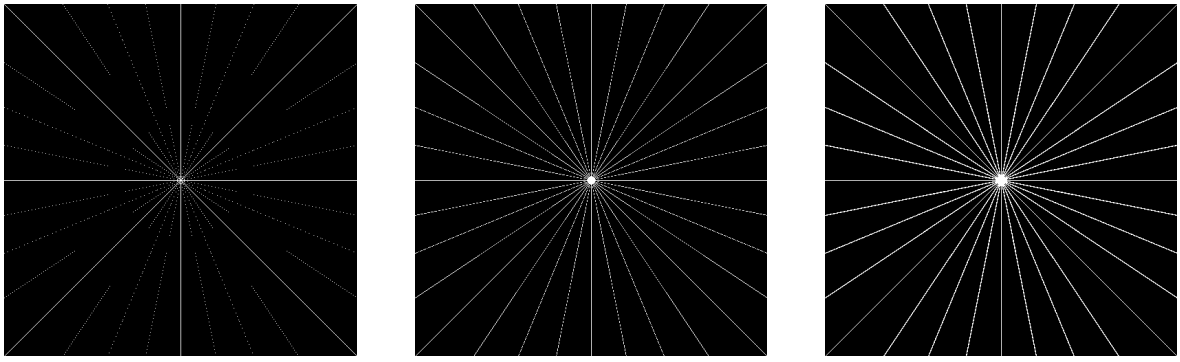

(a) $tol = 0.087$ (5^o) (b) $tol = 0.349$ (20^o) (c) $tol = 0.698$ (40^o)

Figure 3.4 – Radial lines approximation with 20 angles on Cartesian grid taking different tolerances. The white pixels represents the position in the radial lines.

A larger tolerance means more measurements will be available for the minimization algorithm. However, we cannot arbitrarily increase the value of the tolerance because we will consider angular positions farther from the acquired projections. So, the interpolation step adds more error to the measurements. The experiment in Section 5.6 seeks to elucidate that trade-off.

3.6.2.2 The interpolation step

Once the Cartesian positions of the radial lines have been determined, the next step is to interpolate the columns of the sinogram to obtain an estimate of the projections for the angles corresponding to the angular coordinates of the Cartesian radial lines. We have adopted the two-dimensional cubic spline as the method to compute the interpolations. As an example, Figure 3.5 shows the sinogram of the 512×512 Shepp-Logan phantom acquired at 16 angles together with the interpolated projections for the angles required by the Cartesian radial lines taking $tol = 0.698$. Green lines represent the projections of the sinogram that were acquired at angles that exactly coincide with the radial coordinates of the Cartesian radial lines ($\theta_p = \theta_c$). The other projections of the initial sinogram are indicated in red.

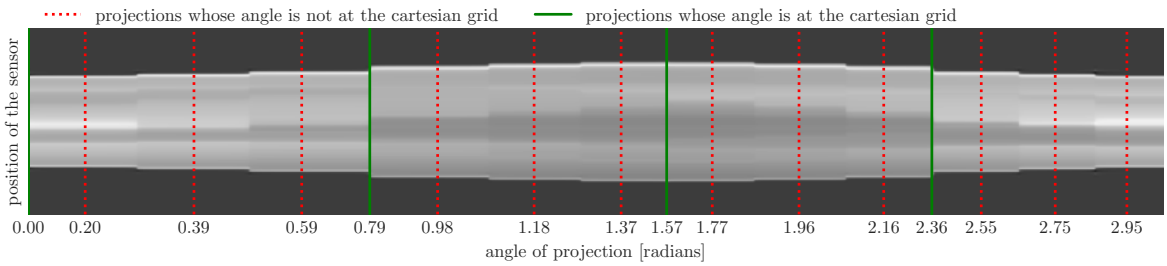

Figure 3.5 – Example of interpolated sinogram of the 512×512 Shepp-Logan phantom for a Cartesian grid taking measurements in 16 angles.

3.6.2.3 The Goertzel algorithm

The last step for computing the measurements in the frequency plane consists of calculating a sample of the DTFT of the projection (line 5 in Algorithm 3.3). The simplest way to do this is by the definition of the DTFT. Thus, the desired measurement is given by

$$X_f = \sum_{n=0}^{N-1} x[n] e^{-j2\pi nf}, \tag{3.38}$$

where $x \in \mathbb{K}^N$ is the vector with the projection and X_f designates its spectral content at the linear frequency f.

The Goertzel algorithm is a more efficient alternative to computing a single sample of the DFT. This method is built on the idea of rewriting the DFT analysis equation as a convolution. This way, a specific DFT coefficient can be calculated from a sample of the result of an IIR filtering process [51, 52].

Recall that the coefficients of the DFT are equally-spaced samples of the DTFT so that the linear frequencies that the DFT can access depend on the sampling frequency

and the length of the discrete signal. The numerical experiments of this work implemented the Generalized Goertzel algorithm proposed in [52]. Their approach expands the standard Goertzel algorithm to calculate DTFT samples for non-integer multiples of the fundamental frequency, i.e., to fractional positions between the samples of the DFT.

3.6.3 Conjugate Gradient method

Images are usually large signals. This fact can be an obstacle to using CS algorithms due to the memory requirements to store the matrices that model the problem. Employing indirect methods for matrix computations is a way to address this issue. For this, it is necessary to have a method to calculate the linear map without directly operating the matrix product. In the case of medical images, where the measurements are modeled as samples in the frequency domain, we can use the FFT algorithm.

The Conjugate Gradient (CG) is a numerical method for solving linear systems that can be used to enable the reconstruction of medical images by CS algorithms. The method starts from an initial guess and iteratively approaches the solution by observing the direction of the gradient of the function. The CG is a key technique for engineering first proposed in [53]. Currently, several other formulations exist for specific applications; in the context of CS, we can cite [54, 55].

In Chapter 4, we will propose a structure for medical image reconstruction that exploits the properties of the measurements to decompose the problem into some lower-dimensional reconstructions to allow the use of the direct method in the matrix computations required by the CS algorithms.

Chapter 4

The Proposed Direct Reconstruction Structure for Medical Imaging

Adopting $p < 1$ to reconstruct a signal by ℓ_p minimization leads to non-convex algorithms. However, decreasing p has the potential to reduce the number of measurements required for reconstruction. This assertion is tested in [17] through two numerical examples. In a more simplistic scenario, the first one consists of reconstructing one-dimensional signals. The second example reconstructs the 256×256 Shepp-Logan phantom using measurements on radial lines in the frequency plane in a setting similar to the reconstruction of medical images.

Reconstructions of better standards are expected to be obtained from the same set of measurements by reducing p when solving the minimization problem. Generally, we cannot simply choose a value of p arbitrarily close to zero. It is observed because of stability issues of the reconstruction algorithms. In addition, below a specific value, there is a slight improvement by reducing p further. In the conditions evaluated in [17], their examples verified no significant improvements for $p < 0.5$. For image reconstruction using IRLS, there is not much margin to reduce p since this potentially implies an ill-conditioned problem from the point of view of the indirect method. That leads to long execution times and convergence problems.

Computed Tomography and Magnetic Resonance images are reconstructed from measurements modeled as samples of their spectral content. For MR, the measurements are directly acquired in the frequency domain; and for CT, the Fourier Slice theorem rules the conversion of the acquired projections into spectral data. The Fourier Transform is the mathematical tool that establishes the relationship between the spatial and frequency domains. The linearity is a convenient feature of this transform that

we will explore in regard to devising a CS technique that uses the direct method in reconstructing CT and MR images. On this basis, we expect to be in a position to verify the effects of adopting lower values of p in the reconstruction of medical images.

4.1 General implementations of the DRS

In the last chapter, we presented an approach for reconstructing medical images using CS algorithms. The idea is to recover the image $f[m,n] \in \mathbb{R}^{M\times N}$ by solving the ℓ_p minimization problem

$$\min_{\hat{x}} \|\hat{x}\|_p^p \text{ subject to } A\hat{x} = b, \tag{4.1}$$

where $b \in \mathbb{C}^m$ is the vector of measurements, $\hat{x} \in \mathbb{R}^{MN}$ is the stacked pixels of the image in a sparse representation, and $A \in \mathbb{C}^{m\times MN}$ is the acquisition matrix that concerns the measurement scheme and the sparsifying transform.

The alternative we propose to implement a CS algorithm using the direct method for computing matrix products is based on finding a decomposition for $A\hat{x} = b$. Instead of reconstructing the image through a single minimization, we can solve several lower-dimensional minimizations. The solution to each of these problems is the contribution of one parcel to the composition of the image. That is, we are looking for a sparse representation of the image pixels in the form

$$\hat{x} = \mathcal{C}_{i=0}^{K-1}\{\hat{x}_i\}, \tag{4.2}$$

where $\mathcal{C}_{i=0}^{K-1}\{\cdot\}$ is an appropriate operator for composing the image from the partial signals $\hat{x}_0, \hat{x}_1, \cdots, \hat{x}_{K-1}$. Thus, each contribution $\hat{x}_i$ can be related to a different parcel b_i of the measurements through the linear system

$$A_i\hat{x}_i = b_i \tag{4.3}$$

where each $b_i \in \mathbb{K}^{m_i}$ contains part of the information of the measurements b, each $\hat{x}_i \in \mathbb{K}^{r_i}$ is part of the sparse signal we want to recover, and $A_i \in \mathbb{K}^{m\times r_k}$ establishes the relationship between these partial signals and the related partial measurements. Naturally, we have interest in the cases that $r_i \leq MN$ and $m_i < m\ \forall i \in \{0,\cdots,K-1\}$.

In summary, what we call Direct Reconstruction Structure (DRS) is this strategy of composing the medical image from the solution of some minimization problems given

by

$$\min_{\hat{x}_i} \|\hat{x}_i\|_p^p \text{ subject to } A_i\hat{x}_i = b_i. \tag{4.4}$$

Modeling the image formation in this manner reduces the size of the reconstructed signals and can make possible the use of the direct method in Compressive Sensing algorithms. Different models for the matrices A_i and the composition operator $\mathcal{C}_{i=0}^{K-1}\{\cdot\}$ are viable, leading to different formulations for the reconstruction scheme. Therefore DRS is not a unique reconstruction method but a way of conceiving the use of CS algorithms with the direct method for medical image reconstruction. Figure 4.1 illustrates the general operation of DRS for an arbitrary model of matrices A_i.

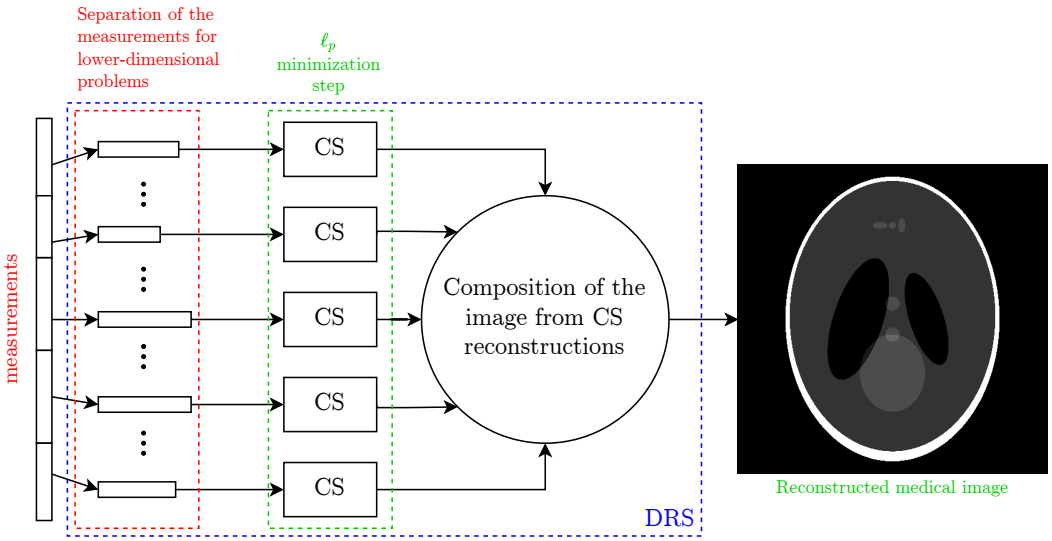

Figure 4.1 – Generic representation of the Direct Reconstruction Structure for an arbitrary decomposition of the relationship between the measurements and the sparse signal to be reconstructed.

4.2 Mathematical model for a DRS formulation based on the reconstruction of rows

Because the measurements available for reconstructing CT and MR images are samples in the frequency domain, we formulate a first implementation of DRS from a decomposition that considers the contribution of each row of the Cartesian frequency plane to form the image in the pixel domain. Let us start by recalling the 2D-IDFT

$$f[m,n] = \sum_{k=0}^{M-1}\sum_{l=0}^{N-1} F[k,l]e^{j2\pi\left(\frac{Km}{M}+\frac{ln}{N}\right)}, \tag{4.5}$$

that computes an image $f[m,n] \in \mathbb{R}^{M\times N}$ from its spectral content $F[k,l] \in \mathbb{C}^{M\times N}$. We aim to find a family of M signals $h_i[m,n] \in \mathbb{C}^{M\times N}$ in the pixel domain, such that each represents the contributions of a single row of the spectrum $F[k,l]$. That is, the DFT $H_i[k,l]$ of $h_i[m,n]$ is defined as

$$H_i[k,l] = \begin{cases} Y_i[l], & \text{if } k = i. \\ 0, & \text{otherwise.} \end{cases}, \tag{4.6}$$

where $Y_i[l] \in \mathbb{C}^N$ is a one-dimensional signal that equals the i-th row of $F[k,l]$,

$$Y_i[l] = F[i,l]. \tag{4.7}$$

Given that the signals $h_i[m,n]$ and $H[k,l]$ are a Fourier Transform pair, we can write $h_i[m,n]$ as a function of $Y_i[l]$ from the definition of the 2D-IDFT

$$h_i[m,n] = \sum_{k=0}^{M-1}\sum_{l=0}^{N-1} H_i[k,l] e^{j2\pi\left(\frac{km}{M}+\frac{ln}{N}\right)}. \tag{4.8}$$

Only the i-th row of $H_i[k,l]$ has non-null elements. We can expand this last Equation to isolate the contribution of these nonzero elements. Thus, we have that

$$\begin{aligned} h_i[m,n] &= \sum_{k=0}^{i-1}\sum_{l=0}^{N-1} H_i[k,l] e^{j2\pi\left(\frac{km}{M}+\frac{ln}{N}\right)} + \\ &\quad \sum_{l=0}^{N-1} H_i[i,l] e^{j2\pi\left(\frac{ki}{M}+\frac{ln}{N}\right)} + \\ &\quad \sum_{k=i+1}^{M-1}\sum_{l=0}^{N-1} H_i[k,l] e^{j2\pi\left(\frac{im}{M}+\frac{ln}{N}\right)} \end{aligned} \tag{4.9}$$

$$h_i[m,n] = \sum_{l=0}^{N-1} H_i[i,l] e^{j2\pi\left(\frac{ki}{M}+\frac{ln}{N}\right)}. \tag{4.10}$$

By definition, the term $H_i[i,l]$ in Equation 4.10 equals $Y_i[l]$. So,

$$h_i[m,n] = \sum_{l=0}^{N-1} Y_i[l] e^{j2\pi\left(\frac{ki}{M}+\frac{ln}{N}\right)} \tag{4.11}$$

$$h_i[m,n] = \sum_{l=0}^{N-1} Y_i[l] e^{j2\pi\left(\frac{im}{M}\right)} e^{j2\pi\left(\frac{ln}{N}\right)} \tag{4.12}$$

$$h_i[m,n] = e^{j2\pi\left(\frac{im}{M}\right)} \sum_{l=0}^{N-1} Y_i[l] e^{j2\pi\left(\frac{ln}{N}\right)}. \tag{4.13}$$

Note that the sum in Equation 4.13 is the 1D-IDFT of $Y_i[l]$. Taking this into account, we can write the signal $h_i[m,n]$ as

$$h_i[m,n] = e^{j2\pi\left(\frac{im}{M}\right)}\mathcal{F}_{1D}^{-1}\{Y_i[l]\} \tag{4.14}$$

$$h_i[m,n] = e^{j2\pi\left(\frac{im}{M}\right)}y_i[n], \tag{4.15}$$

where $\mathcal{F}_{1D}^{-1}\{\cdot\}$ denotes the 1D-IDFT operator and $y_i[n] \in \mathbb{C}^N$ is the Inverse Transform of $Y_i[l]$. Equation 4.15 computes the contribution of the components along a single row of the spectrum in the synthesis of the image pixels. Thus, we have reached a representation that enables a decomposition of the measurements as expected for implementing DRS.

The signal $h_i[m,n]$ has a property that can be used to reduce even more the dimension of the minimization problems in the DRS. Notice in Equation 4.15 that each row of $h_i[m,n]$ is calculated as the product of $y_i[n]$ by a complex exponential. All the signal information is contained in just one of its rows since all of them are equal to the $y_i[n]$ except for a phase compensation term. It is illustrated in Figure 4.2.

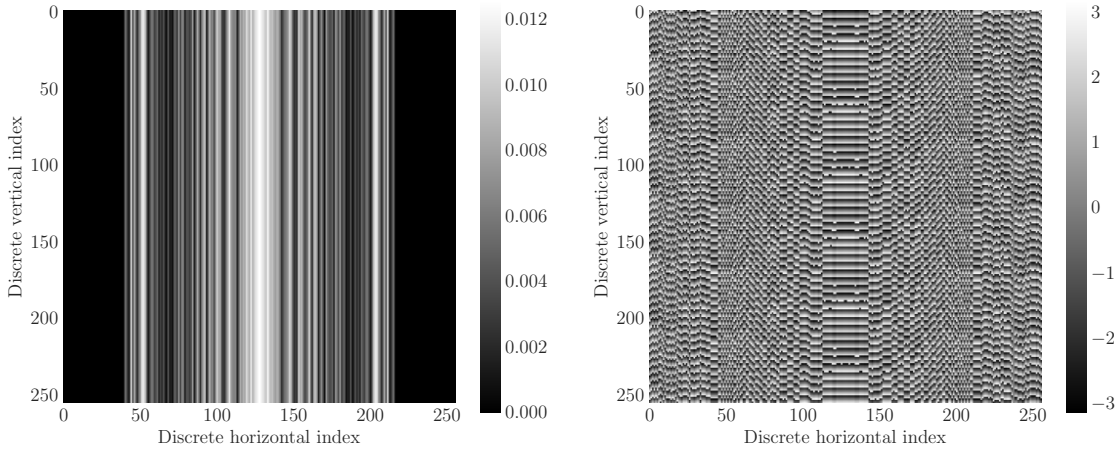

(a) Magnitude.

(b) Phase.

Figure 4.2 – A signal that contains the pixel domain information related to a single row in the frequency plane. This example was calculated from the 50^{th} row of the spectrum content of the 256×256 Shepp-Logan phantom.

So far, we have seen how the spectral information $Y_i[l]$ of row i is represented in the pixel domain as the signal $h_i[m,n]$. However, to define a formulation of DRS, we lack how to compose the image $f[m,n]$ from the signals $h_i[m,n]$. We can derive it by observing that Equation 4.6 gives $F[k,l]$ as the sum of all signals $H_i[k,l]$. Then, due to

the linearity of 2D-DFT, we obtain the image $f[m,n]$ by summing all signals $h_i[m,n]$,

$$f[m,n] = \sum_{i=0}^{M-1} h_i[m,n]. \tag{4.16}$$

We can now define one ℓ_p minimization problem for each row of $F[k,l]$. The measurements b_i are samples of $Y_i[l]$ according to the positions sampled in the medical image acquisition scheme. Eventually, the signals $y_i[n]$ will not meet the sparsity conditions. Therefore, in the general case, an appropriate sparsifying transform $T_i \in \mathbb{K}^{N\times N}$ is used to obtain the sparse representation $\hat{y}_i[n] = T_i y_i[n]$. In outline, the minimization problems for this specific DRS implementation can be written as

$$\min_{\hat{y}_i} \|\hat{y}_i\|_p^p \text{ subject to } W_i T_i^{-1} \hat{y}_i[n] = b_i, \tag{4.17}$$

where $W_i \in \mathbb{C}^{m_i \times N}$ is formed by selecting the rows of the 1D-DFT matrix related to the positions of the measurements b_i in $Y_i[l]$. These minimizations will find estimations for the signals $y_i[m,n]$, from which we can calculate the signals $h_i[m,n]$ and later compose the image $f[m,n]$ using the Equations 4.15 and 4.16.

The strategy of composing the image from successive reconstructions concerning a single row of measurements in the Cartesian frequency plane, can also be understood from the separability property of 2D-DFT. In essence, solving the minimization problem of Equation 4.17 is to estimate the spectral components of a row at the positions where there are no measurements and then compute its 1D-IDFT. After conducting this procedure for all rows, the image composition is a matter of calculating the 1D-IDFT of the columns of the matrix whose rows are the solutions to the minimization problems[1]. Figure 4.3 shows the implementation of this DRS formulation based on the reconstructions from the contribution of each row of measurements.

In contrast to DRS, the approach that uses an indirect method estimates the missing spectral components across the entire frequency plane at once[2], and the inversion of the 2D-DFT does not occur at intermediate steps (first the rows and then the columns). In other words, DRS reconstructs one-dimensional signals whose entries refer to the spectral components of the 1D-DFT of the columns of the image to be reconstructed. Meanwhile, the conventional approach reconstructs signals in a domain concerning the pixel information of the image. Figure 4.4 illustrates this difference.

[1] Recall that the solution to the minimization problem is in a sparse domain. Thus, before the composition step, the signal must be calculated on the proper basis ($y_i[n] = T_i^{-1}\hat{y}_i[n]$).

[2] If prefiltering is the strategy for sparsity representation, a minimization problem will be solved for each filter.

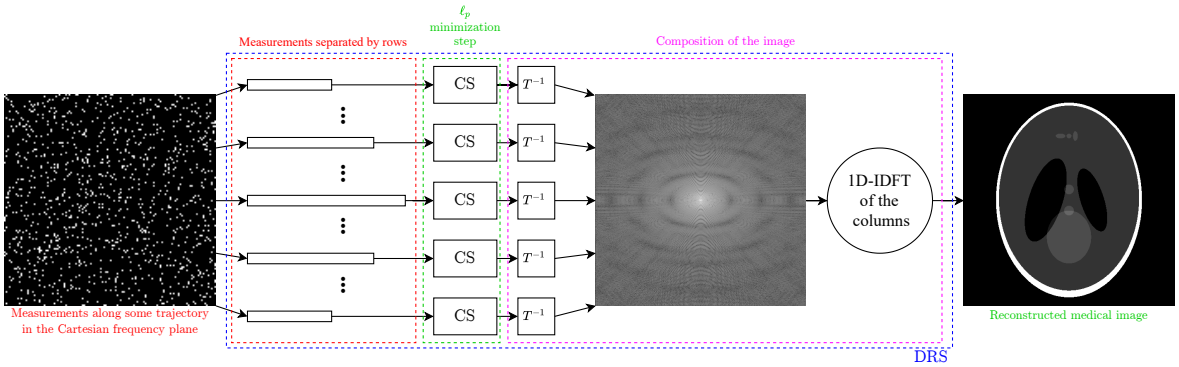

Figure 4.3 – Representation of the DRS formulation based on reconstructions of the contribution of each row of measurements.

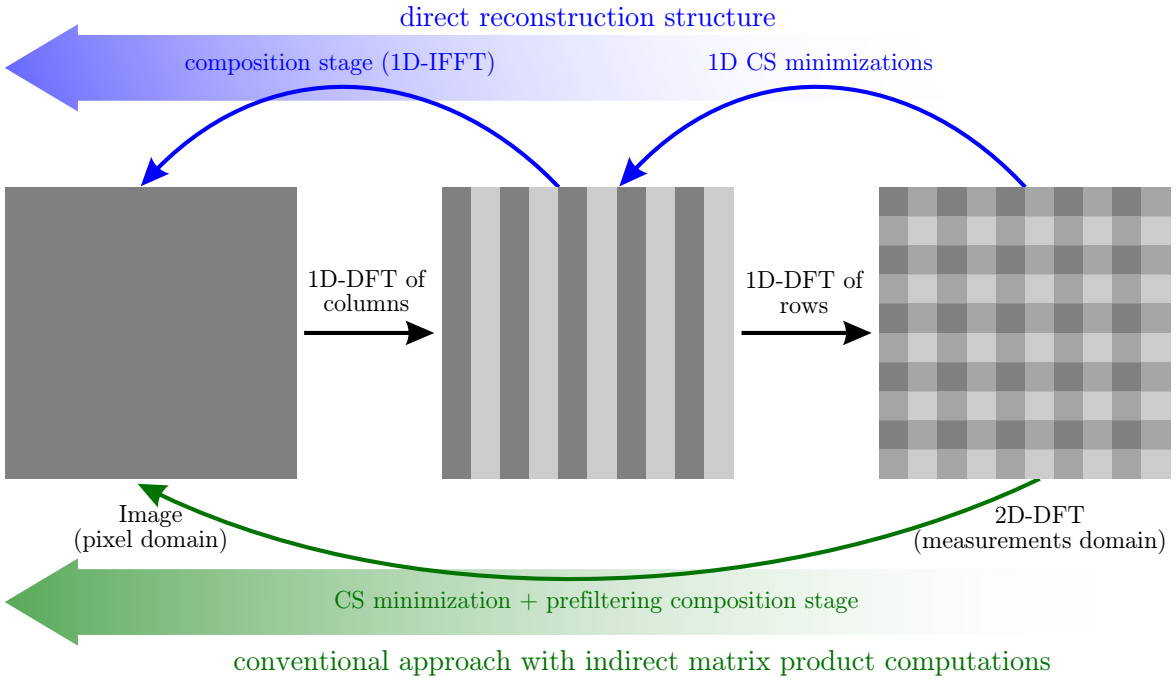

Figure 4.4 – Comparison between the DRS and the conventional CS-based reconstruction approach (with an indirect method) in the design of the ℓ_p minimization problems.

4.3 Limitations of the decomposition by rows for modeling the DRS

The DRS formulation we have just derived is of simple computational implementation since the measurements b_i are straightforward to gather, and the matrices A_i are easily obtained from the DFT matrix W. However, our development does not ensure that a strategy for sparsely representing the image will also be efficient in sparsifying the one-dimensional signals reconstructed in this particular DRS formulation. Thus, sparse representation strategies for models that require an indirect method will not necessarily be appropriate for a specific DRS model. Additionally, despite the mathematical convenience, this formulation does not guarantee that the solutions to the lower-dimensional problems (Equation 4.17) will compose the minimum solution to the image reconstruction problem (Equation 4.1).

Each signal reconstructed by DRS contains information regarding a single row of coefficients in the frequency domain. Note that by solving a minimization problem for each row, we are ignoring some information that lies in the correlation between the rows in favor of exploiting the direct method in the reconstruction algorithm. It occurs because the decomposition chosen in Equation 4.16 does not guarantee the decoupling of the system variables. In this regard, an alternative is to look for composition strategies that model the acquisition of measurements as block diagonal matrices. By doing so, we can divide the acquisition matrix A into submatrices A_i independent of each other in the sense that they have a complete parcel of information.

In summary, the row composition strategy we derived is non-optimal in guaranteeing that the sparsest solutions of the lower-dimensional problems will compose a signal corresponding to the sparsest solution to the complete image reconstruction problem. An alternative strategy that we expect to cope with this issue is to model the DRS with matrices as

$$A = P \begin{bmatrix} A_0 & 0 & \cdots & 0 \\ 0 & A_1 & \cdots & 0 \\ \vdots & \vdots & \ddots & \vdots \\ 0 & 0 & \cdots & A_{K-1} \end{bmatrix} Q, \tag{4.18}$$

where P and Q are change of basis matrices and each matrix A_i defines a lower-dimensional minimization problem.

Designing a DRS formulation of the form of Equation 4.18, as well as the task of defining a sparse representation, is also a problem of finding a convenient basis. In this matter, a formulation based on the Jordan canonical form is a reasonable first

approach to be investigated, given the vast literature available on the topic. To obtain a computational implementation, besides defining the submatrices A_i, it is necessary to understand how to arrange the measurements b_i. In this work, we intend to validate DRS's ability to use a direct method in CS algorithms for medical imaging. For this reason, we chose to perform our numerical experiments using the formulation presented in Section 4.2, owing to its simplicity and ease of implementation. We may pursue more mature and mathematically sophisticated implementations in future work.

4.4 An implementation of DRS with prefiltering

In our first tests to evaluate the performance of the proposed DRS formulation in reconstructing MR images, we employ prefiltering as the sparsity representation strategy, as in the conventional approach using the indirect method. For the prefiltering, we have to choose a set of filters to apply to the measurements in the frequency domain. Then, an image is reconstructed from each set of filtered measurements. Each of these intermediate images has part of the information of the image we want to recover. Since the filters are chosen to ensure that the reconstructed images are sparse in the pixel domain, it is not necessary to define a sparsifying transform. In Equation 4.17, we can set T as the identity matrix.

Algorithm 4.1 Direct Reconstruction Structure based on the reconstruction of rows with prefiltering.

Input: Measurements b in the Cartesian frequency plane; 2D filters g_k for prefiltering.
Output: Recovered image $f[m, n]$.

1: **for** each filter g_k **do**
2: Create a zero matrix M_k of the same shape as the Cartesian frequency plane.
3: Set b_k as the measurements b filtered with g_k.
4: **for** each row i in the Cartesian frequency plane **do**
5: Set $b_{k,i}$ as the entries of b_k that are in the i-th row of the frequency plane.
6: Compute $\hat{y}_{k,i}$ by solving the minimization problem in Equation 4.17 ($b_{k,i}$ as measurements and the identity matrix as the sparsifying transform).
7: Replace the i-th row of M_k with $\hat{y}_{k,i}$.
8: **end for**
9: Obtain the sparse image $f_k[m, n]$ by calculating the 1D-IDFT of each column of the matrix M_k.
10: **end for**
11: Compose the image $f[m, n]$ using the measurements b and all the partial images $f_k[m, n]$ as described in Section 3.6.1

Algorithm 4.1 schematize the general idea of how this DRS implementation operates. Note that there are two stages of composition in this implementation of DRS with prefiltering. The first is to compose the sparse images from the solutions to the min-

imization problems. Moreover, the second, concerning prefiltering, seeks to compose the desired image from the intermediate images computed in the previous stage.

4.4.1 Adapting the MR implementation of DRS to CT

The algorithm we have now derived can be used for CT and MRI image reconstruction. As discussed in Chapter 2, the measurements taken by the CT scanner are modeled as projections and therefore need to be rearranged as samples of the image spectrum along radial lines. The reconstruction scheme for CT images (Figure 4.5) has a step before DRS for conditioning the measurements. We have described this procedure in Algorithm 3.3. In the case of MR, the samples are taken directly in the frequency plane along different possible trajectories.

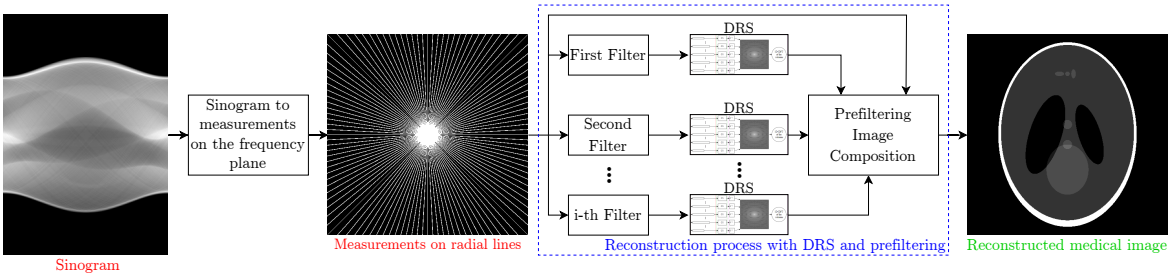

Figure 4.5 – Reconstruction scheme using the DRS with prefiltering for CT images. In the case of MR, the scheme remains the same, but the process starts with the measurements already in the frequency plane, and they can be in other trajectories than radial lines.

Next, we will evaluate this implementation of DRS in the reconstruction of CT and MR images through computational experiments. In this way, we will be in a position to compare the use of direct and indirect methods for reconstructing images with CS algorithms. The examples we will conduct will also help to understand the sources of error in DRS and point out improvements to these techniques.

Chapter 5

Computational Experiments

In the current Chapter, we present numerical examples to assess the performance of the DRS formulation we derived in Section 4.4. First, we evaluate the expected behavior of the quality of reconstructions based on minimizing ℓ_p as we reduce the value of p in reconstructions of one-dimensional artificial signals. Subsequently, we conduct reconstructions of some test images under specific conditions and then compare the results produced by other reconstruction algorithms. We also evaluate the impact that converting the sinogram to frequency plane measurements has on the results in the case of CT. These topics are covered in a total of four numerical experiments:

- Experiment 1: reconstructions of artificial 1D signals varying the value of p.
- Experiment 2: reconstructions of the Shepp-Logan phantom and actual medical images from open databases.
- Experiment 3: reconstructions of artificial images with good sparsity features.
- Experiment 4: reconstructions of the Shepp-Logan phantom with measurements on different Cartesian radial lines.

We compiled the results of the reconstructions into CSV files and made them available at this link. All simulations were conducted with Python scripts on an AMD Ryzen 5 3500U CPU running the Zorin OS 16.1 operating system. The main libraries we used are:

1. phantominator: generation of the Shepp-Logan phantom.
2. Numpy: FFT computation and other vector and matrix manipulations.
3. SciPy: generation of the sinograms, reconstructions with FBP, interpolations in Algorithm 3.3, IIR filter in Goertzel algorithm, and statistical analyses.

4. Pandas: organization of the files containing the simulation results.

5. Matplotlib: visualization of the results and generation of the charts presented throughout this monograph.

We emphasize that we have not implemented the codes optimally in terms of the consumption of computational resources. Our main concern was testing the theoretical reconstruction model we had previously derived. Thus, in-depth discussions about computational complexity are out of the scope of this thesis. Only short comments on the execution time of some of the reconstructions will be given as means of providing a brief notion about these issues.

5.1 Parameters for results evaluation

We have assessed the quality of the results by calculating two parameters: the Signal-to-Noise Ratio (SNR) and the Structural Similarity Index Measure (SSIM). Both indices are measures of how close the information obtained in the reconstruction is to the original signal that was used to compute the measurements used in the reconstruction process. Throughout the discussion of the results, we will also show some reconstructed images to discuss how these quantitative metrics affect some "perceptual characteristics" of the images.

SNR is a measure of the error distributed over all signal entries. In other words, it is calculated as the ratio of the original signal power to the reconstruction error power and is often expressed on the logarithmic decibel scale. Considering that x is the reference signal and x_s is the reconstructed signal[1], the SNR is given by

$$\mathrm{SNR}_{\mathrm{dB}} = 10 \log_{10} \left(\frac{\|x\|_2^2}{\|x_s - x\|_2^2} \right). \tag{5.1}$$

We remark that SNR is a broader concept that applies to many other areas. Commonly, this measure is also called Signal-to-Error Ratio (SER) in contexts where the reconstruction error is evaluated.

On the other hand, SSIM relies on observing contrast and luminance. These concepts are used to compare the similarity between the structures that constitute the original and the reconstructed image. It is derived in [56] and is calculated as

$$\mathrm{SSIM} = \frac{(2\mu_x\mu_{x_s} + C_1)(2\sigma_{xx_s} + C_2)}{(\mu_x^2\mu_{x_s}^2 + C_1)(\sigma_x^2 + \sigma_{x_s}^2 + C_2)}, \tag{5.2}$$

[1] In Experiment 1, x and x_s refer to a one-dimensional synthetic signal and its reconstruction, while in the other experiments, they represent a vector of stacked pixels of the image.

where μ_x, μ_{x_s}, σ_x^2 and $\sigma_{x_s}^2$ are the mean intensity, and the variance of the pixels in the signals x and x_s, respectively; σ_{xx_s} is the covariance of x and x_s, C_1 and C_2 are small constants to stabilize the division. The SSIM is a value between 0 and 1; reconstructions that achieve higher SSIM are those that preserve better the structures of the original testing image.

SNR is a measure that can be computed for both one- and two-dimensional signals, while SSIM is specific to images. For this reason, SNR is evaluated in all experiments, while we only used SSIM in the experiments involving images. We remark that we also computed the Peak Signal-to-Noise Ratio (PSNR) and the Mean Squared Error (MSE), but adding these indices into the discussions does not bring any new conclusions. Thus, we have chosen to present in the text just the analyses with SNR and SSIM. The PSNR and MSE values can be found in the CSV files containing the reconstructions' results.

In addition, in experiment 1, we will conduct some statistical evaluations through Kolmogorov-Smirnov [57], Anderson-Darling [58], and Wilcoxon [59] hypothesis tests. Commonly, the result of a hypothesis test is the probability that the observed realizations conform to a null hypothesis H_0. This statistic is called the p-value. To avoid confusion with the p referring to the ℓ_p metrics, we will always refer to the result of a statistical test by p-value.

5.2 Experiment 1 – investigating the effects of adopting smaller values of p on the reconstruction quality with a 1D toy example

An aspect that we look forward to with DRS to exploit in medical imaging is the potential to use ℓ_p metrics with smaller values of p. It would allow satisfactory reconstructions from less information. Likewise, it is expected to obtain better quality results from the same set of measurements by reducing p. The numerical example presented in this experiment aims to give us a sense of the behavior of the reconstruction quality when reducing the value of p and how the chosen algorithm can affect the ability to obtain such results.

5.2.1 Simulation methodology

We generated 200 synthetic signals of size 256 for this experiment. Half of them have 16 non-null elements in a known domain. The second half of vectors has 128 non-null entries in another domain. To make the signals sparse, we forced to zero the signal coefficients in the transformed domain at drawn positions. Five acquisition schemes

Table 5.1 – Parameters for IRLS the reconstruction of synthetic 1D signals.

Reconstruction scenario	Method for matrix computations	i_{max}
1	Direct	10
2	Direct	30
3	Indirect (CG)	10
4	Indirect (CG)	30

with 60, 70, 80, 90, or 100 acquired measurements were assumed in the case of the sparser signals. While for the less sparse signals, we considered acquisition schemes with 160, 170, 180, 190, or 200 measurements. We create all matrices and signals with a pseudo-random Gaussian generator (zero mean and unit standard deviation). Altogether, there are two-hundred signals, two sparsifying transforms, and ten measurement matrices.

We used IRLS to compute the reconstructions. There are four different reconstruction scenarios, varying the maximum number of iterations in IRLS before reducing the regularization factor[2] and whether the matrix operations are performed with the direct or an indirect method. Table 5.1 shows the settings in each of the scenarios. The other IRLS parameters are the same for all reconstructions ($\mu_0 = 1$, $\mu_{min} = 10^{-8}$)

Although it is not a criterion that evaluates the guarantee of sparse reconstruction, the ratio of the number of measurements to the number of non-null coefficients in the sparse vector is a parameter we can use to compare different reconstruction schemes. The higher this ratio, the more information is available for estimating the coefficients of the solution. In Figure 5.1, we can see that the schemes for signals with 16 entries are more favorable than those defined for signals with 128 non-null entries. In this way, the experiment covers situations in various sparsity conditions.

5.2.2 Results and discussion

The following discussions consist of statistical evaluations of the SNR behavior for the reconstructions of the 200 synthetic signals under different reconstruction conditions, varying the number of measurements, the ℓ_p metric ($p \in \{0.1, 0.2, \cdots, 0.9, 1.0\}$), and some of the IRLS parameters. In each of the scenarios, we performed 10,000 reconstructions. It covers all possible combinations of acquisition matrices and the chosen values of p.

[2] i_{max} in Algorithm 3.2.

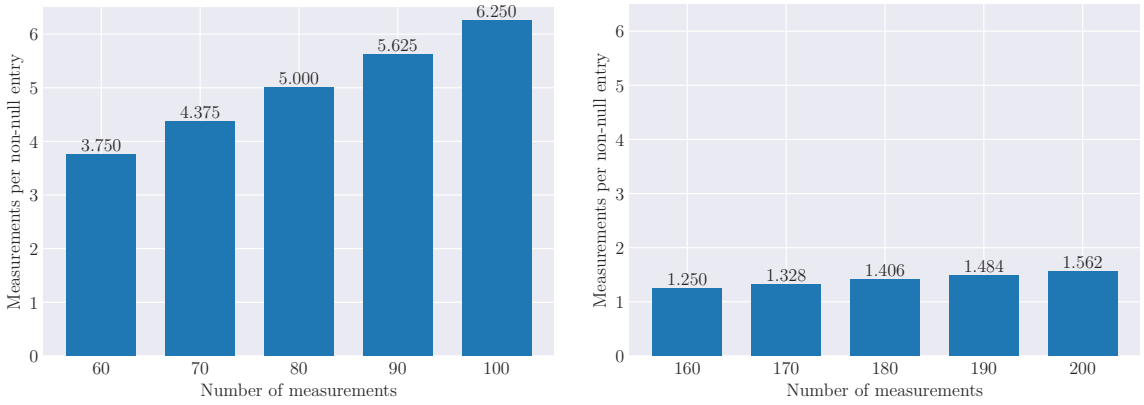

(a) Signals with 16 non-null entries.

(b) Signals with 128 non-null entries.

Figure 5.1 – Ratio of measurements per non-null entry to be estimated by IRLS for each acquisition scheme in reconstructing the synthetic one-dimensional signals.

5.2.2.1 The effect of the number of iterations on the reconstruction quality

The histograms in Figure 5.2 show the distribution of SNR obtained by the reconstructions in each scenario. At first, it is an intuitive expectation that the reconstructions that run more iterations will get closer to the ideal reconstruction and consequently achieve higher SNR levels. Given this perspective, we expect, on average, better reconstructions in scenarios 2 and 4 than in scenarios 1 and 3. Accordingly, when observing the histograms, we notice a higher concentration of reconstructions at the highest SNR levels in the scenarios that allowed more iterations. However, these seem not to be such substantial discrepancies.

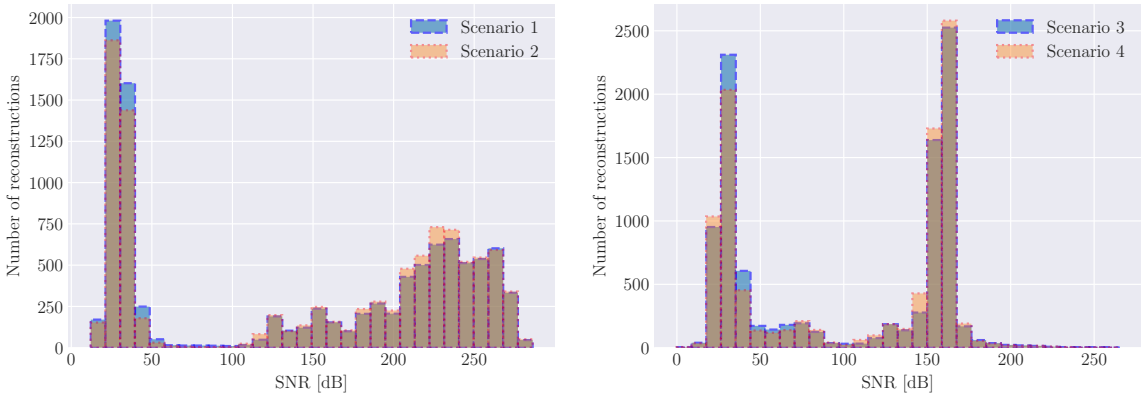

(a) Scenarios 1 and 2 (direct method).

(b) Scenarios 3 and 4 (indirect method).

Figure 5.2 – Histograms of the SNR that reconstructions achieved for each scenario. Each plot contains two histograms. Note that the distributions are similar, so there is a significant overlap between them.

To evaluate if larger values of i_{max} indeed yield better reconstructions, we can

perform a two-sample Kolmogorov-Smirnov test. Here we will consider two random variables, X_{10} concerning the SNR of the reconstructions when $i_{max} = 10$ and X_{30} for the SNR of the reconstructions obtained with $i_{max} = 30$. Their cumulative distributions are $F_{10}(x)$ and $F_{30}(x)$, respectively. Thus, the reconstructions of scenarios 1 and 3 are realizations of X_{10}, while scenarios 2 and 4 correspond to X_{30}. We assume the following hypotheses:

- Null hypothesis (H_0): $F_{10}(x) \leq F_{30}(x)\ \forall x$. Increasing the value of i_{max} in IRLS from 10 to 30 has no significant positive effects on the quality of reconstructions in terms of SNR.
- Alternate hypothesis (H_1): $F_{10}(x) > F_{30}(x)$ for at least one x. Increasing the value of i_{max} in IRLS from 10 to 30 tends to improve the quality of the reconstructions in terms of SNR.

The hypotheses are relative to the cumulative densities. That is, $F_{10} \leq F_{30}$ implies that the realizations of X_{10} tend to be smaller than those of X_{30}. The p-value for the reconstructions we performed is $7.6 \cdot 10^{-17}$, so H_0 is rejected. Therefore, allowing more iterations to be performed before reducing the regularization factor μ tends to improve the quality of the reconstructions, although it is not as apparent when observing the histogram.

Calculating the difference between the SNR of two reconstructions that are distinguished only by the number of iterations is another way to evaluate the contribution of more iterations[3]. Figure 5.3 shows the distribution of these 20,000 differences that can be calculated. Notably, most of the values are concentrated near zero. A negative difference was observed in 35% of them, meaning that by performing more iterations, the quality of the reconstruction worsened. Another 26% registered a null difference, indicating that the stopping criterion for mu reduction was satisfied before ten iterations. Finally, increasing the maximum number of iterations improved the reconstruction in 39% of the cases. These percentages are in accordance with the conclusion of the hypothesis test.

Besides the effects of the number of iterations on the SNR, a second aspect is worth noting in the histograms of Figure 5.2. The reconstructions of scenarios 1 and 2, which used the direct method, are more distributed between 180 and 275 dB. On the other hand, scenarios 3 and 4, which used the indirect method, are mainly concentrated between 145 and 165 dB. It is also reflected in the observed averages. While the mean SNR of the reconstructions with the direct method is 145.4 dB, the indirect method achieved a mean of 101.8 dB.

[3] i.e., both are reconstructions of the same signal that have adopted the same ℓ_p metric and the same method for matrix calculations

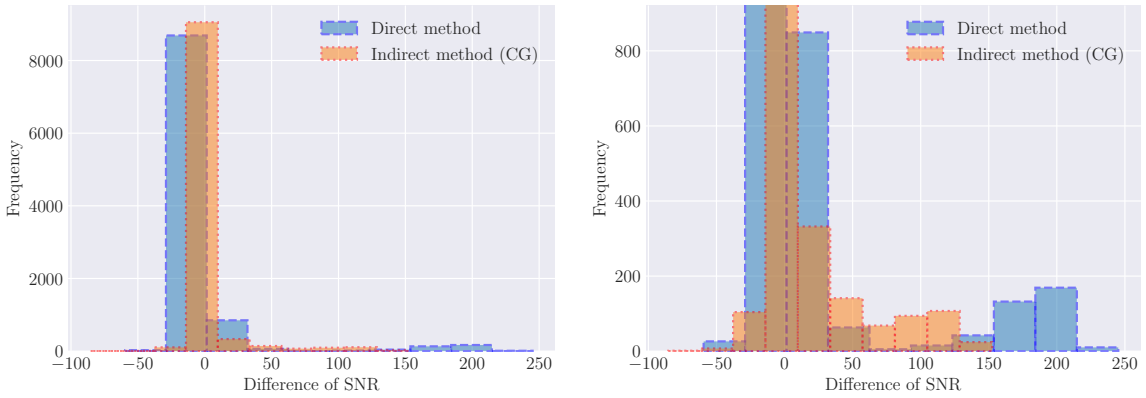

(a) All recostructions.

(b) Less frequent values in detail.

Figure 5.3 – Histogram of the difference between the SNR obtained by reconstructions of the same signal with $i_{max} = 30$ and $i_{max} = 10$. Negative values indicate that reconstruction quality was impaired when running more iterations in IRLS. Cases where the convergence criterion was reached in up to 10 iterations have the same SNR regardless of the value of i_{max}, and the difference is zero.

Among all the evaluated reconstruction cases, in 70 of them, the IRLS did not converge, always in situations using the indirect method. Of these reconstructions that did not converge, 68 occurred for signals with 128 non-null inputs. The two cases in the more sparse signal set occurred with $p = 0.1$. Figure 5.4 shows the distribution of p values for which the reconstructions were not achieved in the case of the less sparse signals. Most of these failed reconstructions occurred for $p \leq 0.2$. It is evidence of the CG stability issues that we expect for lower values of p and more significantly affect the reconstruction of larger signals such as the medical images.

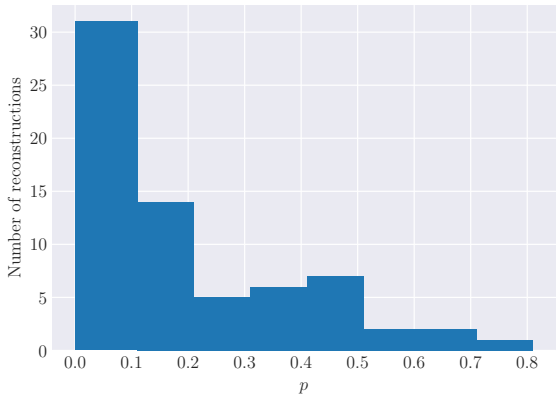

Figure 5.4 – Distribution of the values of p at which the reconstructions of the signals with 128 non-zero entries did not converge.

5.2.2.2 The effect of using ℓ_p with smaller p in reconstruction quality

Up to this point, we have evaluated the effect of the parameter i_{max} on the quality of the reconstructions and verified that reconstructions using the direct method obtained better SNR on average. However, the main goal of this experiment is to study the behavior of the quality of the reconstructions as we adopt ℓ_p metrics with decreasing p. Figure 5.5 presents again the distribution of the SNR achieved by the reconstructions but splitting them into separate histograms according to the value of p used in each reconstruction.

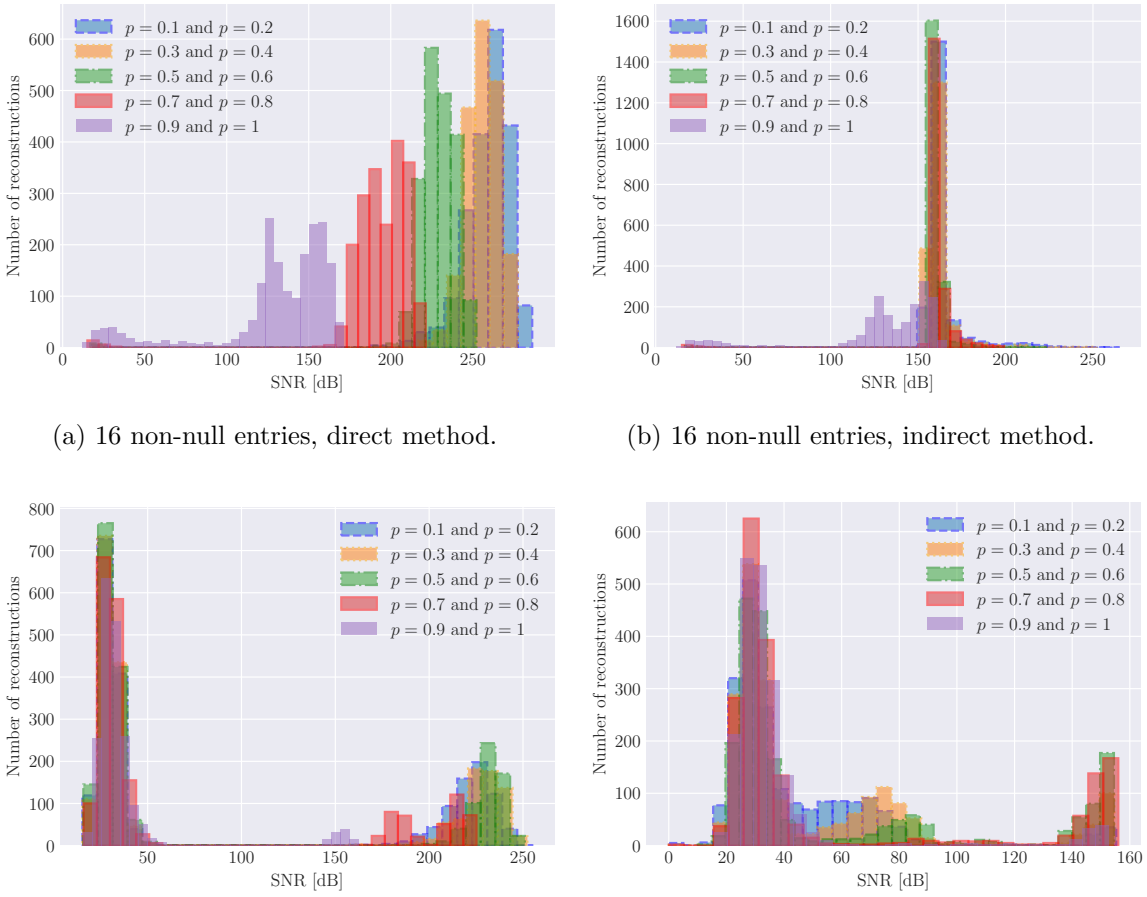

(a) 16 non-null entries, direct method.

(b) 16 non-null entries, indirect method.

(c) 128 non-null entries, direct method.

(d) 128 non-null entries, indirect method.

Figure 5.5 – Histograms of the SNR achieved for each set of signals (16 and 128 non-null entries) separated according to the value of p adopted in the reconstruction and the method for matrix computations in IRLS.

The histograms in Figure 5.5a refer to the direct method reconstructions of the sparsest signals. The cases that adopted lower values of p are concentrated in the regions with the highest SNR. For $p = 1$ and $p = 0.9$, the reconstructions are prevalently up to around 150 dB. The reconstructions with $p = 0.8$ and $p = 0.7$ are mostly distributed in the region between 150 and 200 dB. In the case of $p = 0.6$ and $p = 0.5$,

the reconstructions concentrate in the range from 200 to 250 dB. Finally, for $p \leq 0.4$, most reconstructions reach more than 250 dB.

In the case of reconstructions with the indirect method (Figure 5.5b), the reduction of p is not as evident when looking at the histograms. The reconstructions for $p \geq 0.9$ are mainly concentrated below 150 dB. The reconstructions with the other values of p are all concentrated in a narrower range between 150 and 175 dB. This first visual evaluation of the results in these new histograms indicates that the improvement in the quality of the reconstructions by reducing p is more relevant when using the direct method in IRLS. In the case of the indirect method, reducing p beyond 0.8 does not seem to bring further quality gains.

The gains of reducing p are minimized in the reconstruction of signals with 128 non-zero inputs for both the direct and indirect methods. These signals are less sparse, so there are more reconstructions with SNR below 50 dB. In the case of the direct method, there is a second group of reconstructions concentrated above 150 dB, where we see some quality gain by reducing p down to 0.7. For $p < 0.6$, there are no noticeable quality gains in the histograms of Figure 5.5c. In the indirect case, we also notice two more evident groups of reconstructions. The first is distributed between 20 and 90 dB and the second between 140 and 160 dB. No visual distinction is noticeable between the histograms for the different values of p.

This intuition about how the chosen ℓ_p metric affects the reconstruction quality can be systematically evaluated with hypothesis tests. To this end, we will organize the data into 40 groups, each with $1,000$ reconstructions. Figure 5.6 shows in boxplots the distribution of them. All reconstructions in the same group have in common the ℓ_p adopted, the number of non-null inputs in the sparse domain (16 or 128), and the method used for matrix calculations (direct or indirect). We assume to be zero the SNR of the reconstructions that did not converge. Consider that each of these groups is a set of realizations of a random variable. None of them corresponds to a normal distribution. Table 5.2 shows the results of the Anderson-Darling normality test.

Since the groups of reconstructions do not come from normal distributions, we will use the Wilcoxon test to compare the location of the populations. This non-parametric test evaluates the difference between paired samples coming from X and Y distributions. Thus, we will be able to compare the random variables we have defined in pairs according to the metric adopted in the reconstruction (ℓ_p and $\ell_{p+0.1}$). Let us take the following hypotheses:

- Null hypothesis (H_0): The median of $X - Y$ is negative. It indicates that the samples in Y tend to be larger than the corresponding samples in X, which suggests that the reconstruction conditions in Y yield higher quality results.

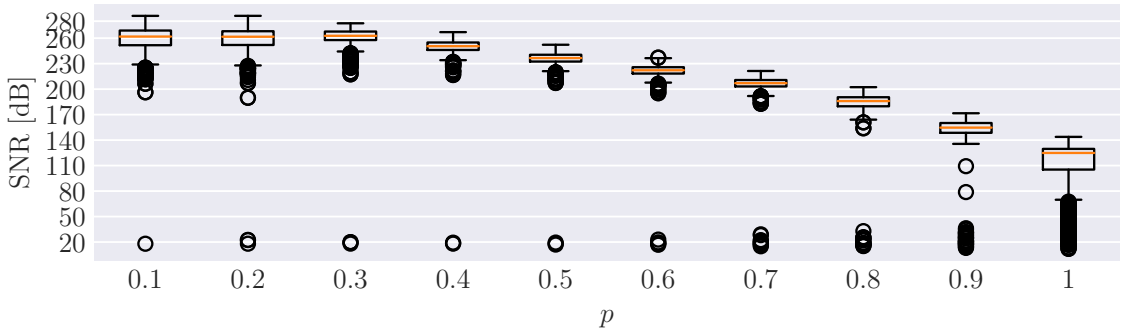

(a) 16 non-null entries, direct method.

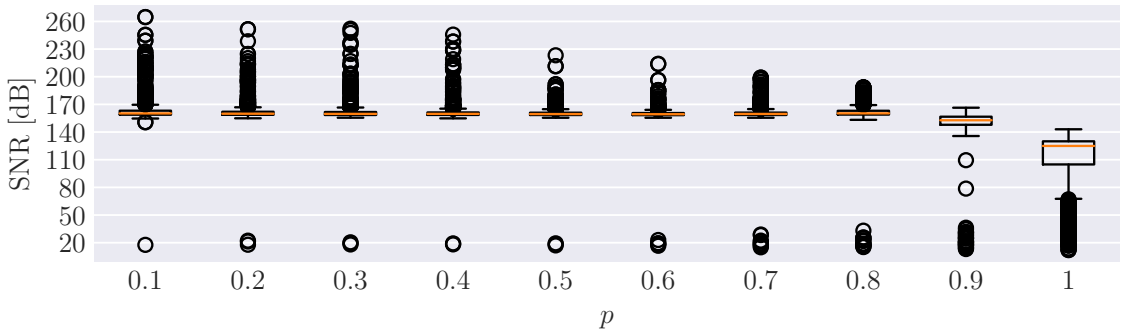

(b) 16 non-null entries, indirect method.

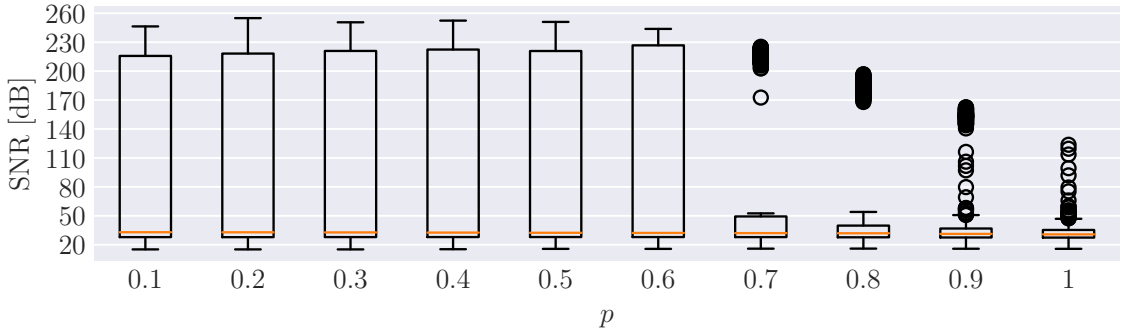

(c) 128 non-null entries, direct method.

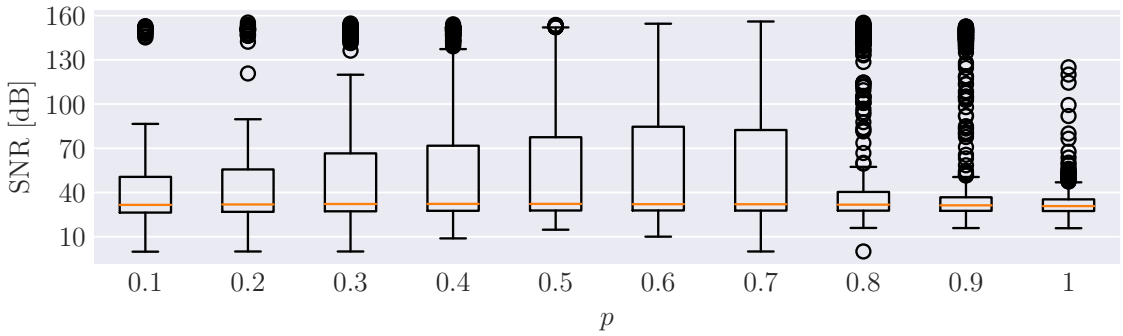

(d) 128 non-null entries, indirect method.

Figure 5.6 – Distribution of the reconstructions into 40 groups defined for the Wilcoxon tests to verify in which conditions the reduction of p reflects in quality gain.

- Alternate hypothesis (H_1): The median of $X - Y$ is positive. It indicates that the samples in X tend to be larger than the corresponding samples in Y, which suggests that the reconstruction conditions of X yield higher quality results.

Table 5.2 – The Anderson-Darling test statistic for each group of 1,000 reconstructions. If the returned statistic is larger than 1.088, then for the significance level of 1%, the null hypothesis that the data come from a normal distribution can be rejected.

metric	Further reconstruction settings			
	sparser signals direct method	sparser signals indirect method	less sparse signals direct method	less sparse signals indirect method
$\ell_{0.1}$	19.1	171.3	161.3	52.9
$\ell_{0.2}$	45.7	175.4	163.5	69.6
$\ell_{0.3}$	87.2	189.6	167.9	83.7
$\ell_{0.4}$	91.9	196.8	171.6	104.5
$\ell_{0.5}$	95.8	188.9	177.5	118.4
$\ell_{0.6}$	131.9	229.1	193.5	139.9
$\ell_{0.7}$	164.8	225.2	202.7	164.2
$\ell_{0.8}$	133.9	203.7	211.7	187.6
$\ell_{0.9}$	154.2	189.1	215.9	203.0
ℓ_1	123.5	123.4	36.2	37.1

We assume that X refers to reconstructions that adopted the metric with the smallest p between the two being compared in each test. Thus, rejecting H_0 is a statistical indication that that particular reduction of p improves the quality of the reconstructions. Table 5.3 shows the p-values returned for each Wilcoxon test we conducted.

Hypothesis tests support that adopting ℓ_p metrics with lower values of p improves the quality of reconstructions when using the direct method under more favorable sparsity conditions. In the case of signals with 16 non-null entries, there is statistical evidence that IRLS set with the parameters we describe achieves better results if we reduce p to 0.3. There are no significant gains when we reduce beyond 0.3. For the same signals, reconstructions with the indirect method exhibit consistent gains if we reduce p up to 0.8. In the case of signals with 128 non-null entries, there are consistent quality gains when reducing p to 0.6 using the direct method and to 0.7 in the indirect case.

This finding is tellingly illustrated in the boxplots of Figure 5.6. In the case of the more sparse signals, this new representation shows more pronounced falls in the medians of the distributions at the same values of p indicated by the hypothesis tests. For the less sparse signals, the quality improvement is seen as the increased distance between the first and third quartiles, indicating that the SNR values are distributed over larger intervals for certain ℓ_p metrics.

At last, we can take into account the number of measurements available for reconstruction when evaluating the quality gain by reducing p. The plots in Figures 5.7 and

Table 5.3 – The Wilcoxon test p-values for each comparison between the metrics adopted in reconstructions. The fields filled in blue are the p-values for which H_0 is rejected for the usual confidence levels. In red are the cases in which we cannot reject the H_0. Moreover, in yellow are the cases that can or cannot be rejected depending on the desired confidence level.

metrics being compared	Further reconstruction settings			
	sparser signals direct method	sparser signals indirect method	less sparse signals direct method	less sparse signals indirect method
$X = \ell_{0.9}$ $Y = \ell_1$	$1.7 \cdot 10^{-165}$	$1.7 \cdot 10^{-165}$	$9.2 \cdot 10^{-90}$	$4.6 \cdot 10^{-85}$
$X = \ell_{0.8}$ $Y = \ell_{0.9}$	$1.7 \cdot 10^{-165}$	$4.4 \cdot 10^{-157}$	$3.9 \cdot 10^{-75}$	$1.6 \cdot 10^{-41}$
$X = \ell_{0.7}$ $Y = \ell_{0.8}$	$1.7 \cdot 10^{-165}$	0.999	$3.1 \cdot 10^{-76}$	$1.1 \cdot 10^{-5}$
$X = \ell_{0.6}$ $Y = \ell_{0.7}$	$1.7 \cdot 10^{-165}$	0.999	$1.5 \cdot 10^{-63}$	0.934
$X = \ell_{0.5}$ $Y = \ell_{0.6}$	$1.7 \cdot 10^{-165}$	0.004	0.044	0.999
$X = \ell_{0.4}$ $Y = \ell_{0.5}$	$1.7 \cdot 10^{-165}$	0.088	0.035	0.999
$X = \ell_{0.3}$ $Y = \ell_{0.4}$	$1.06 \cdot 10^{-148}$	0.184	0.967	0.999
$X = \ell_{0.2}$ $Y = \ell_{0.3}$	0.999	0.182	0.964	1.0
$X = \ell_{0.1}$ $Y = \ell_{0.2}$	0.205	$1.3 \cdot 10^{-4}$	0.999	1.0

5.8 show the SNRs' mean values and standard deviation obtained in each scenario[4]. The curves are arranged according to the number of measurements. Again, the quality gain is readily perceived in the case of the sparser signals reconstructed with the direct method. The average SNRs for the reconstructions with the indirect method is close to 160 dB for $p \leq 0.8$. Furthermore, reconstructions computed from fewer measurements tend to have lower SNR, mainly when reconstructed with the direct method, since the mean SNR is very similar for all amounts of measurements when $p \leq 0.8$ in the indirect case.

The number of measurements most affects the SNR of signals with 128 non-null entries. In Figure 5.8, reconstructions with a maximum of 180 measurements achieved the lowest quality, averaging less than 50 dB. The direct method reconstructions

[4]as defined in Table 5.1

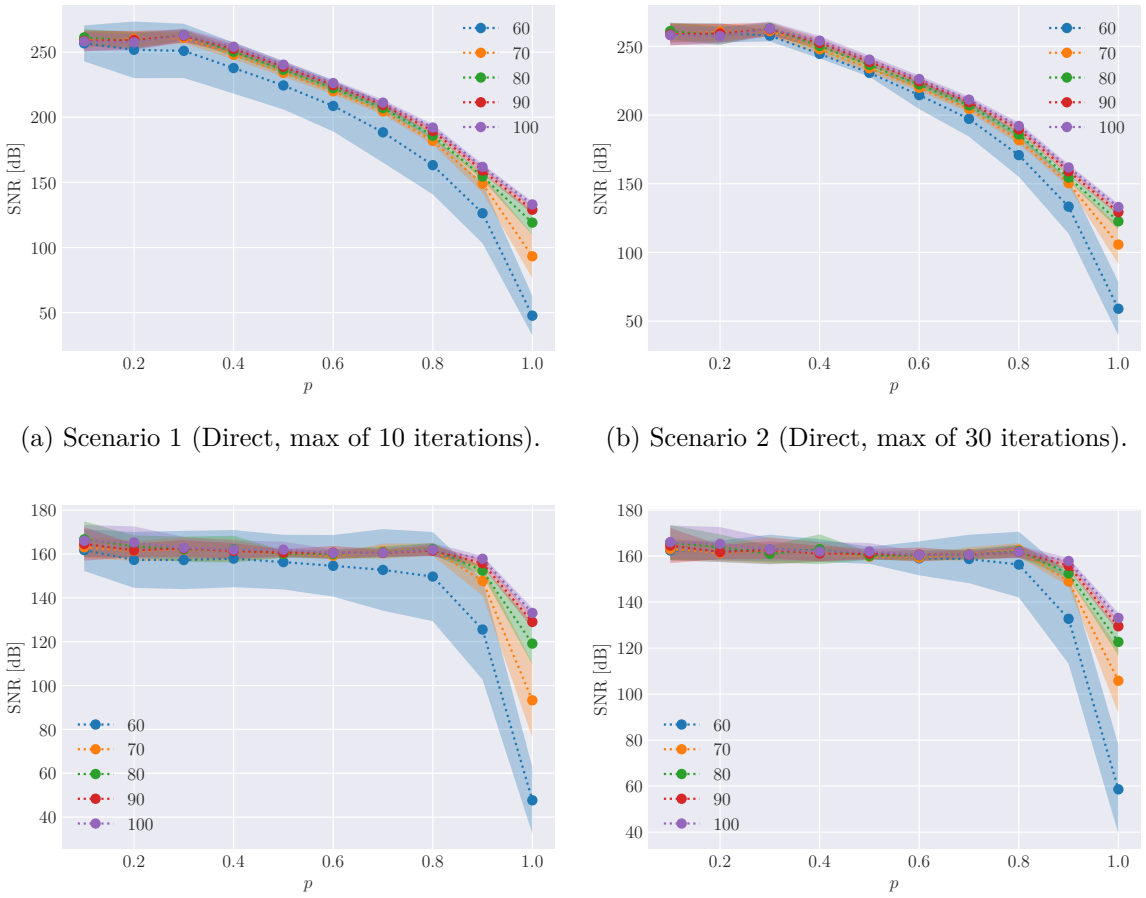

(a) Scenario 1 (Direct, max of 10 iterations).

(b) Scenario 2 (Direct, max of 30 iterations).

(c) Scenario 3 (Indirect, max of 10 iterations).

(d) Scenario 4 (Indirect, max of 30 iterations).

Figure 5.7 – Mean SNR value achieved in reconstructing the sparser synthetic signals (16 non-null entries) for each scenario. The area filled around the curves indicates the range of one standard deviation centered on the mean.

show the behavior we have described so far when we vary the ℓ_p metric. That is, the reconstruction quality tends to be better for a smaller p, but there is a value beyond which the gains are no longer significant. However, this occurs in the curves for 190 and 200 measurements. Reconstructions with fewer measurements keep a similar SNR regardless of the metric ℓ_p.

The reconstructions with 190 and 200 measures using the indirect method are the ones that present more dissonant behavior than we have described so far. In these situations, the reconstruction quality improves by reducing p to some extent and impairs if we keep reducing. While p is closer to 1, the poor conditioning of the matrices did not affect the quality gain provided by the reduction of p. Nevertheless, when approaching the value of p to zero, the instabilities inherent to the indirect method are more significant and affect the quality of the reconstructions. It indicates that in less favorable conditions for sparse reconstruction (lower sparsity and fewer measurements available), adopting ℓ_p metrics closer to ℓ_0 does not necessarily reflect quality gain if

the reconstruction algorithm relies on indirect methods.

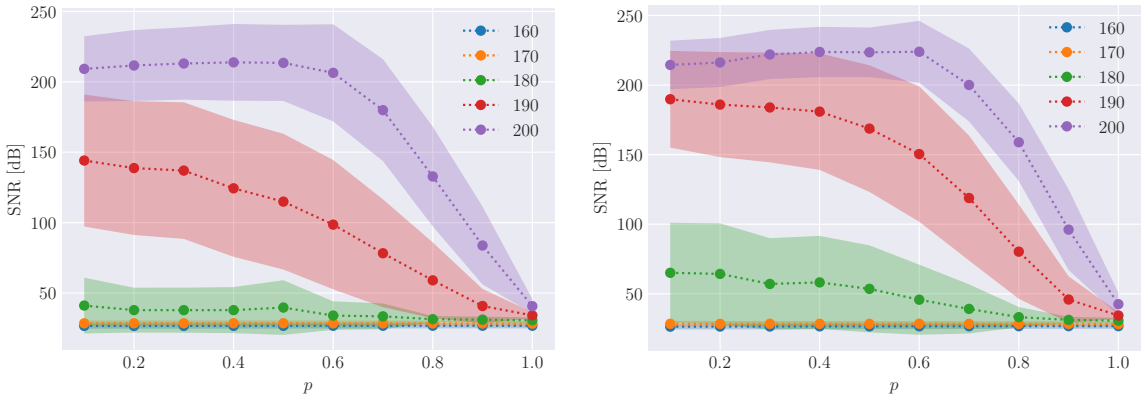

(a) Scenario 1 (Direct, max of 10 iterations).

(b) Scenario 2 (Direct, max of 30 iterations).

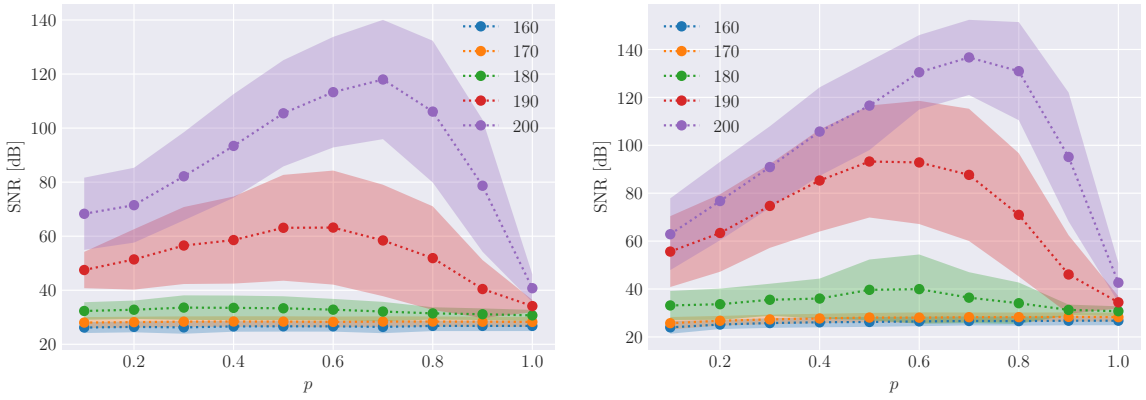

(c) Scenario 3 (Indirect, max of 10 iterations).

(d) Scenario 4 (Indirect, max of 30 iterations).

Figure 5.8 – Mean SNR value achieved in reconstructing the less sparse synthetic signals (128 non-null entries) for each scenario. The area filled around the curves indicates the range of one standard deviation centered on the mean.

5.2.2.3 A remark on sparsity reconstruction conditions

Section 3.3 discussed the Mutual-Coherence index as a theoretical criterion for evaluating whether sparse reconstruction is guaranteed for a particular measurement acquisition matrix. Recall that this is a sufficient but not necessary condition for uniqueness. This experiment computed measurements using ten different acquisition schemes. Figure 5.9 shows the index $\frac{1}{2}(1 + 1/\mu(A))$ for each adopted acquisition matrix in this experiment. According to Theorem 3.2, this value gives the maximum sparsity for which the sparsest solution is guaranteed to be unique.

Reconstruction schemes that acquire more information tend to guarantee reconstruction for less sparse signals. However, the Mutual-Coherence of a matrix depends on the angular distance between its columns, so the amount of measurements is not

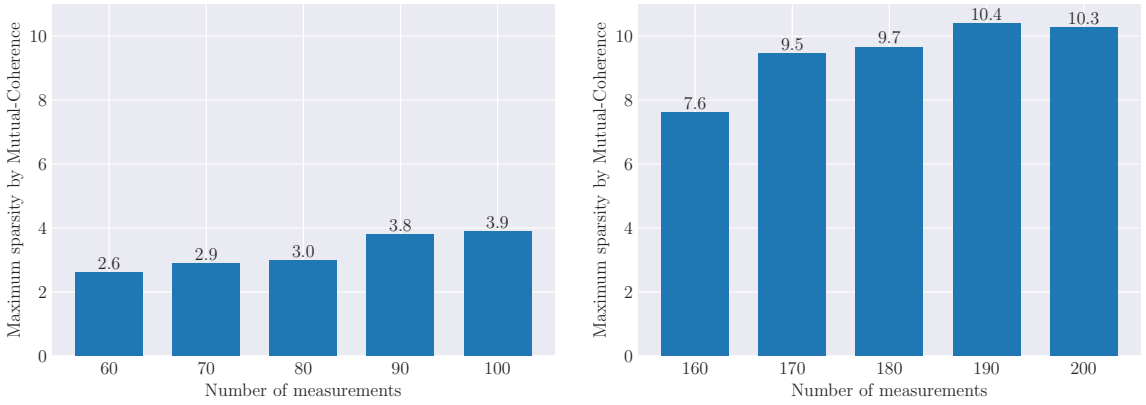

(a) Signals with 16 non-null entries.

(b) Signals with 128 non-null entries.

Figure 5.9 – Mutual-Coherence criteria for each acquisition matrix available for experiment 1.

the only factor affecting the value of this index. In this experiment, the tested schemes that acquire fewer measurements guarantee the reconstruction of signals with 2 or 3 non-null entries. Schemes with more measurements, on the other hand, ensure the reconstruction of signals with up to 7, 9, or 10 non-null entries. These values are considerably below the sparsity of the tested signals (16 and 120 non-null entries).

We sampled each of the 200 tested signals using five acquisition matrices. Thus, we have calculated the reconstructions from $1,000$ different sets of measurements. For each of them, we computed 40 reconstructions under different IRLS settings varying the metric ℓ_p, i_{max}, and whether it used a direct or indirect method. Figure 5.10 shows the distribution of the best reconstructions in terms of SNR obtained for each set of measurements. They are ordered according to the acquisition scheme that generated them. Observe that, for the sparsest signals, the reconstructions are all above 225 dB. It means that there was always some IRLS setting that was able to reconstruct each of the signals with 16 non-null entries satisfactorily.

In the case of the less sparse signals, the reconstructions with 190 and 200 measurements are concentrated between 210 and 250 dB. However, there are many outliers in the 20 to 50 dB interval. The best reconstructions of the reconstruction schemes with 150, 160, and 170 measurements are mostly distributed between 15 and 60 dB. There are some outliers between 200 and 250 dB in the case of the scheme with 170 measurements. Despite being at a lower quality level than those observed for the sparser signals, these could be reasonable levels for applications where SNR is not a critical bottleneck.

This discussion illustrates that despite being a valuable tool in modeling Compressive Sensing problems, Mutual-Coherence may be a criterion that excludes specific

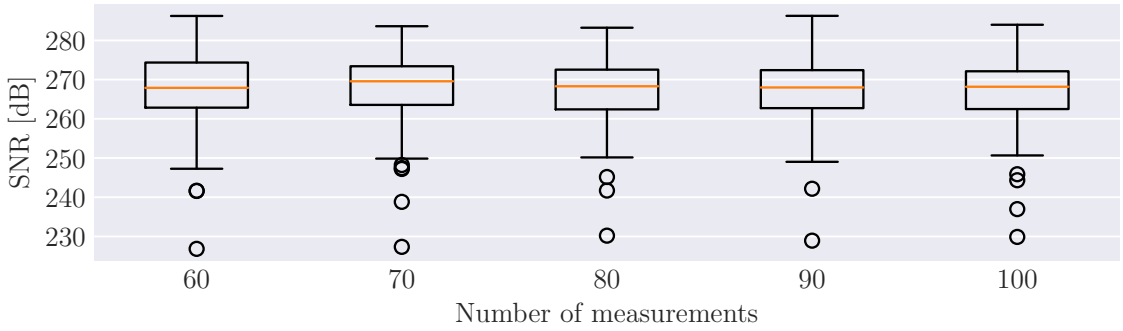

(a) Signals with 16 non-null entries.

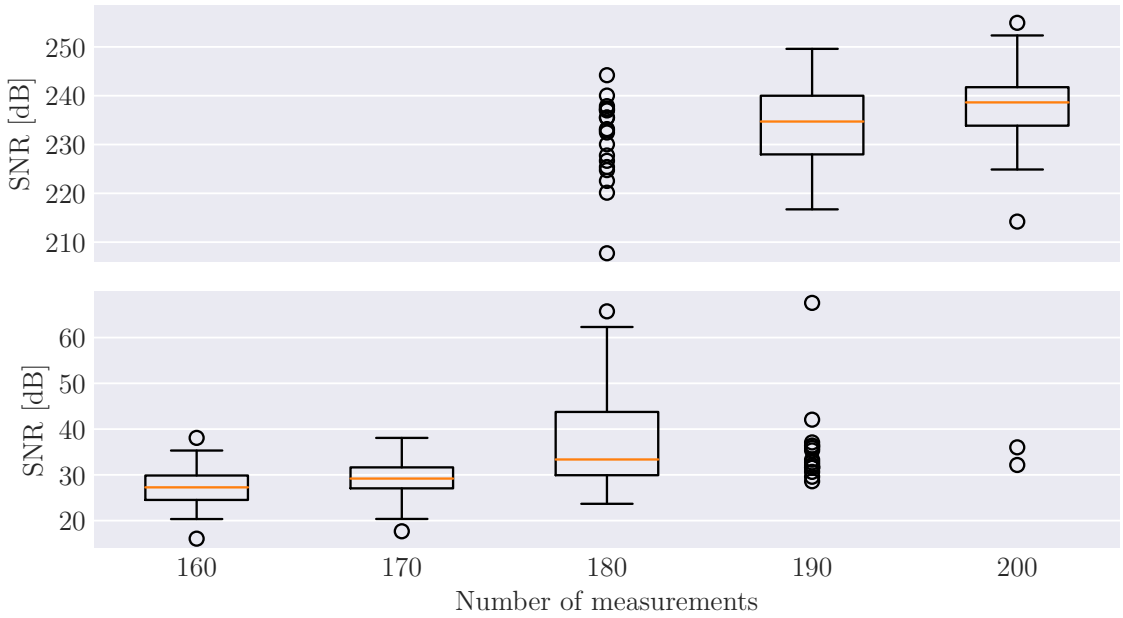

(b) Signals with 128 non-null entries.

Figure 5.10 – Distribution of the best reconstruction for each set of measurements.

conditions in which sparse reconstruction would achieve satisfactory results. Thus, evaluation through numerical examples is an appealing option for validating CS algorithms. The Restricted Isometry Property, another uniqueness criterion discussed in Section 3.3, is often computationally prohibitive. For instance, computing the Mutual Coherence of each acquisition matrices for the sparsest signals in this example involves the computation of $\binom{256}{2} = 32,640$ inner products. The RIP, as stated in Theorem 3.3, would require the eigenvalue decomposition of $\binom{256}{32} \approx 5.8 \cdot 10^{40}$ submatrices.

5.3 Default image reconstruction settings

The following experiments we will discuss consist of reconstructing some testing images under different conditions (such as the number of angles, adopted ℓ_p metric, and algorithm). Many parameters can affect the quality of the results. Therefore, to keep the reproducibility of the work, we will describe here the default values adopted in these parameters. These settings may be changed for some specific simulations, but this will be explicitly mentioned. The reconstructions will be computed using four different algorithms:

1. Filtered Back-Projection (FBP) in reconstructions of the Shepp-Logan phantom or actual CT images.
2. Iteratively Reweighted Least Squares using the Conjugate Gradient to compute the matrix products indirectly as described in Section 3.6. This reconstruction algorithm will also be referred to as IRLS-CG.
3. Iteratively Reweighted Least Squares in the Direct Reconstruction Structure as described in Section 4.4. This reconstruction algorithm will also be referred to as IRLS-DRS.
4. Measurements Inversion (MI). It consists of calculating the image using the 2D-IFFT while assuming the values at positions in the frequency plane zeros where there are no acquired measurements. The idea of using it is to get a sense of how the spectral values computed by the other algorithms contribute to the quality of their results.

The simulations cover acquisition schemes with the following number of equispaced angles: $\{120, 130, \cdots, 210, 220\}$. In cases where measurements are along radial lines, the tolerance adopted when defining which Cartesian positions belong to the radial lines[5] is $tol = \frac{40\pi}{180} \approx 0.698$. Figure 5.11 shows the percentage of the positions considered as measurements for each number of acquired angles in regard to this tolerance value.

For CS algorithms based on ℓ_p minimization, the simulations tested (for each of the different sets of measurements) the ℓ_p metrics for $p \in \{0.1, 0.2, \cdots, 0.9, 1.0\}$. The parameters adopted when using IRLS as the minimization algorithm is described in Table 5.4. At last, when the prefiltering scheme is the sparsity representation strategy, we used the 2D Haar high-pass kernels,

$$g_1 = \begin{bmatrix} 1 & -1 \\ 1 & -1 \end{bmatrix}, \; g_2 = \begin{bmatrix} 1 & 1 \\ -1 & -1 \end{bmatrix}, \text{ and } g_3 = \begin{bmatrix} 1 & -1 \\ -1 & 1 \end{bmatrix}. \tag{5.3}$$

[5]Details of this procedure was given in Section 3.6.2.1

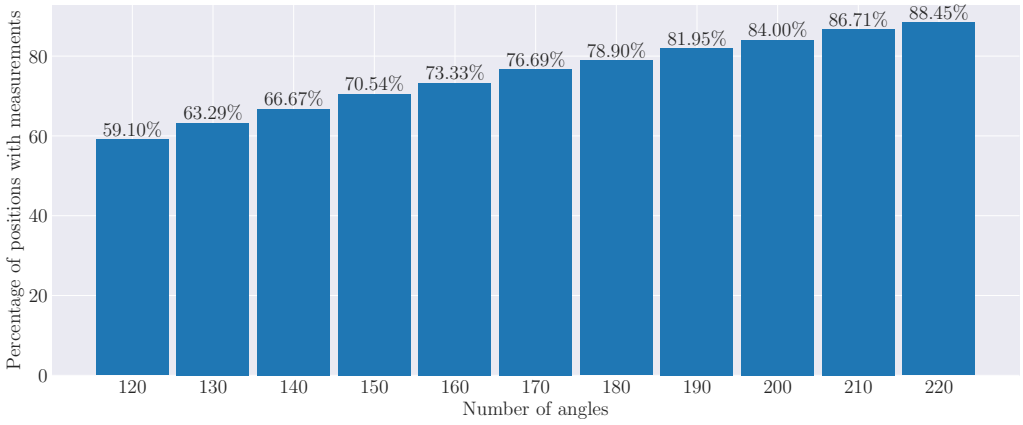

Figure 5.11 – Percentage of positions in the 256×256 grid that is measurements for each number of angles when defining the Cartesian radial lines with $tol = 0.698$.

We have used as testing images the Shepp-Logan phantom and actual images chosen randomly from open databases. In the case of CT, breast images were selected from the "COVID-19 image data collection" [23]. The images in this database are of different shapes, so we resized the selected images by cropping them to a square shape whose side is a power of 2 and then downsampling to 256×256. In the case of MR, anatomical head images provided by the Biomedical Informatics Research Network (BIRN) were chosen [27]. The actual testing images are shown in Figures 5.12 and 5.13, while Table 5.5 presents the identifiers we will use to refer to each selected image. We also carry out some reconstructions using synthetic images created with good sparsity conditions for DRS. The process of the reconstruction simulations occurs in three steps:

1. Simulation of the measurements: in the case of MR, the measurements of the testing image are calculated via 2D-FFT, and only the positions along radial lines trajectory are considered. For the case of CT, where the measurements are projections that form a sinogram, we consider two scenarios. In the first one, the measurements are estimated as the sinogram of the image. In the second scenario, we assume the measurements to be samples on radial lines of the 2D-DFT, as is done for MR. We will refer to the first scenario as "non-ideal" measurements and the second case as "ideal" measurements.

2. Reconstruction process: consists of executing one of the four algorithms mentioned above to obtain a reconstructed image from the simulated measurements.

3. Analysis of the results: comprises comparisons between the testing image and its reconstruction. The parameters for analysis were defined in section 5.1.

Table 5.4 – Parameters used in reconstructions with IRLS.

	Parameter	Description	Default value
Common for IRLS-CG and IRLS-DRS	μ_0	The initial value for the regularization factor	1
	μ_{min}	The minimum value for the regularization factor	10^{-8}
	i_{max}	Maximum of iterations before reducing the regularization factor. The regularization factor is reduced after i_{max} iterations if the threshold criterion is not met	50
IRLS-CG	*tol* (CG)	Tolerance for the convergence of the CG method	10^{-3}
	i_{max} (CG)	Maximum of inner iterations in the CG method	2 times the number of measurements

Table 5.5 – Identifiers of the actual images used in the numerical experiments.

Filename in the original database	Identifier in this text
1-s20-S0929664620300449-gr3_lrg-c	CT1
3ED3C0E1-4FE0-4238-8112-DDFF9E20B471	CT2
191F3B3A-2879-4EF3-BE56-EE0D2B5AAEE3	CT3
1-s20-S0929664620300449-gr3_lrg-d	CT4
000308150214 (slices 5)	MR1
000324094767 (slice 10)	MR2
000308150214 (slices 10)	MR3
000324094767 (slice 5)	MR4

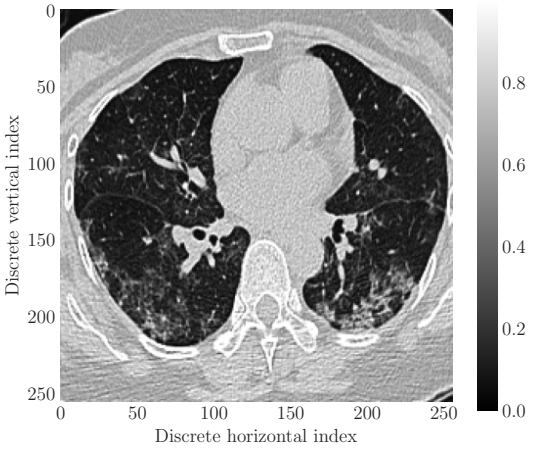

(a) CT1.

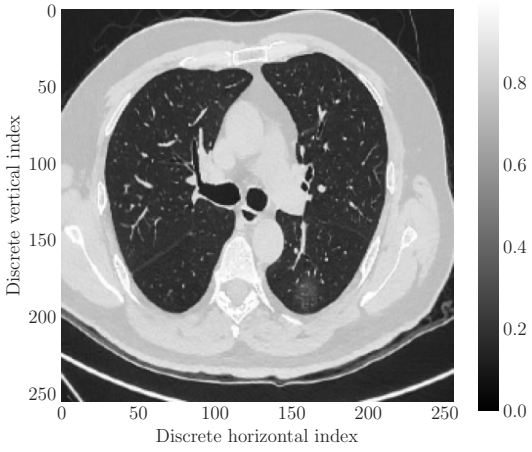

(b) CT2.

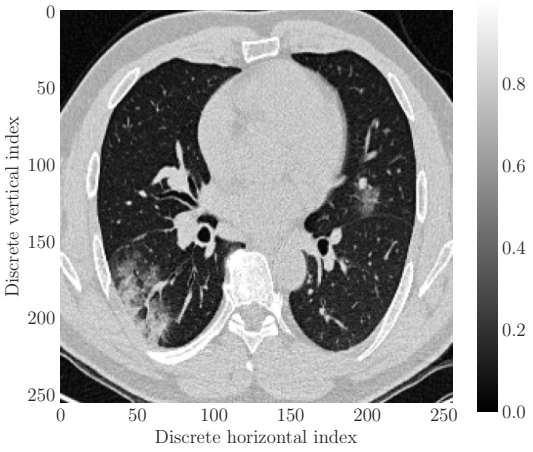

(c) CT3.

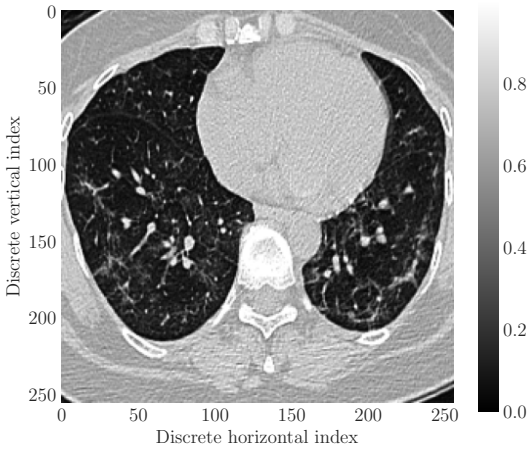

(d) CT4.

Figure 5.12 – The actual CT images used in our experiments from COVID-19 image data collection.

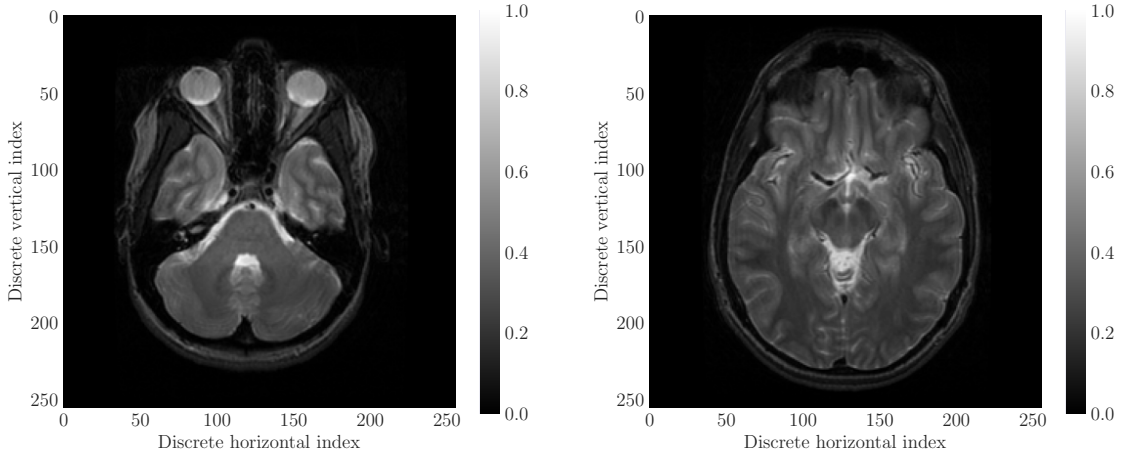

(a) MR1.

(b) MR2.

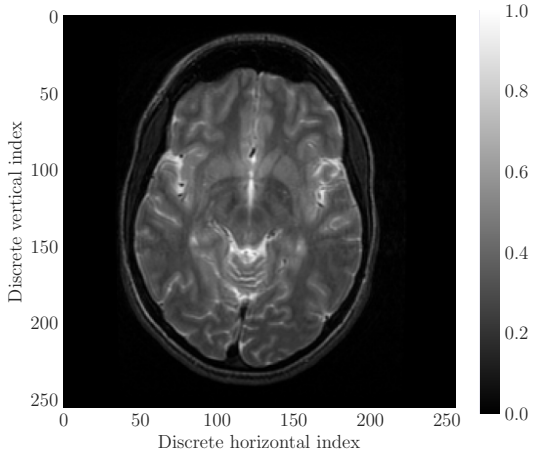

(c) MR3.

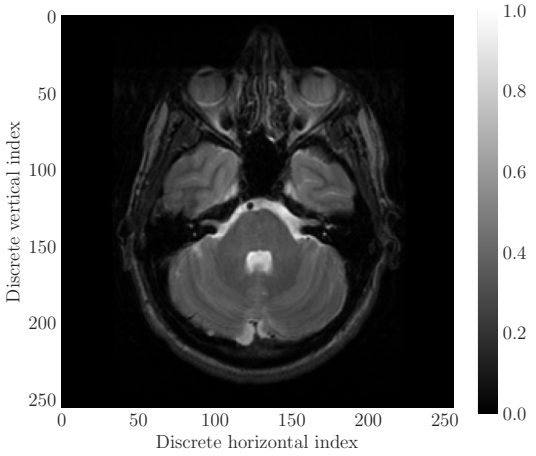

(d) MR4.

Figure 5.13 – The actual MR images used in our experiments from Biomedical Informatics Research Network.

5.4 Experiment 2 – image reconstruction using prefiltering as the sparsity representation strategy

In the previous experiment, we used a generic one-dimensional example to analyze the behavior of the reconstruction quality when changing the metric ℓ_p in the minimization problem specification. The results support that higher quality reconstructions can be achieved for smaller values of p when using the direct method. These gains are not as significant when using the indirect method. In the context of medical imaging, it points out that the IRLS-DRS could require fewer measurements to obtain the same quality as the IRLS-CG. We will now investigate whether this quality gain by reducing p also occurs in the case of reconstructing medical images.

5.4.1 Simulation methodology

In this experiment, we will compute reconstructions of the Shepp-Logan phantom and the actual images CT1, CT2, MR1, and MR2. All of size 256×256. Here we will consider the algorithms, ℓ_p metrics, and measurements as stated in Section 5.3. Prefiltering will be used for sparse representation in the CS-based algorithms. Thus, for IRLS-CG, the image is computed from 3 two-dimensional signals reconstructed by minimizing ℓ_p. In the case of IRLS-CG, each of these two-dimensional signals is computed from 256 one-dimensional signals, totaling 768 CS reconstructions to form a medical image.

Table 5.6 shows the sparsity in the pixel domain of the filtered versions of each of the testing images. Among them, CT images have the worst sparse representation for the chosen filters. The Shepp-Logan phantom has the best sparse representation through prefiltering. The following discussions will primarily consider the results of the Shepp-Logan phantom reconstructions. We will also use some of the reconstructions from the CT2 and MR2 images. Additional plots of the reconstructions of all the testing images that are not covered here are in Appendix A.

Table 5.6 – Percentage of entries whose magnitude is under 10^{-6} for each filtered version of the testing images reconstructed by the CS algorithms

Testing Image	Sparsity obtained with filter		
	g_1	g_2	g_3
Shepp-Logan	96.65%	97.28%	97.80%
CT1	1.43%	1.51%	2.17%
CT2	7.40%	7.59%	11.09%
MR1	26.80%	26.67%	27.05%
MR2	28.23%	28.18%	28.44%

5.4.2 Results and discussion

As we outlined in Section 5.3, we have computed the reconstructions from two types of measurements. The first one, called "non-ideal," concerns measurements estimated by computing the Radon Transform of the test image and then computing the spectral coefficients in the frequency plane using Algorithm 3.3. We have used these measurements for reconstructing the Shepp-Logan phantom and CT images. The second type of measurement, called "ideal," refers to measurements that were estimated as samples of the DFT of the image at Cartesian radial lines. These measurements were used for the reconstruction of all testing images. All reconstructions computed with FBP used the projections given by the Radon Transform as measurements.

Initially, we intended to calculate the reconstructions for p between 0.1 and 1 for all algorithms with all measurement sets. However, we found that IRLS-CG ran very slowly for $p < 0.7$. For example, the reconstruction of the Shepp-Logan phantom with 120 non-ideal measurements and using $p = 0.6$ took almost 7 hours and did not converge. Likewise, we quit running the algorithm after 26 hours when we tried $p = 0.1$. The reconstructions of the Shepp-Logan phantom with ideal measurements are an exception. For all other testing images, it was not feasible to compute the reconstructions with IRLS-CG adopting $p < 0.7$ with either ideal or non-ideal measurements. For this reason, these values are missing in the plots.

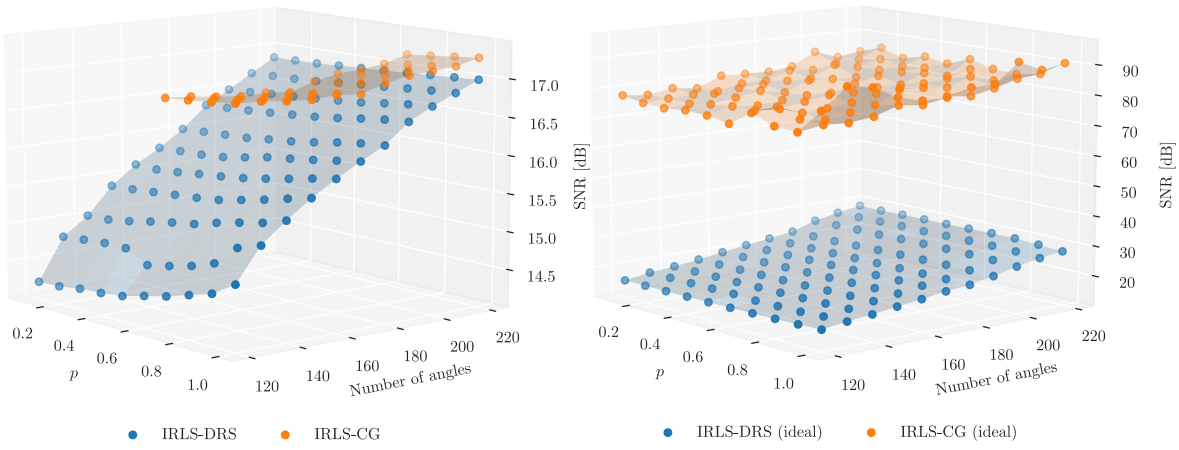

(a) Non-ideal measurements.

(b) Ideal measurements

Figure 5.14 – SNR achieved by the reconstructions of the Shepp-Logan phantom. Each surface corresponds to a reconstructions algorithm.

The SNR observed for every reconstruction of the Shepp-Logan phantom computed by the CS-based algorithms can be seen in the plots in Figure 5.14. The reconstructions with IRLS-CG achieved better SNR levels in all conditions evaluated. In the reconstructions from non-ideal measurements, the difference between the results of the two algorithms is smaller. We can also see that the reconstructions with ideal measure-

ments have a higher quality level than those calculated with non-ideal measurements. This difference reflects the error introduced in the measurements by the interpolations when estimating them from the sinogram.

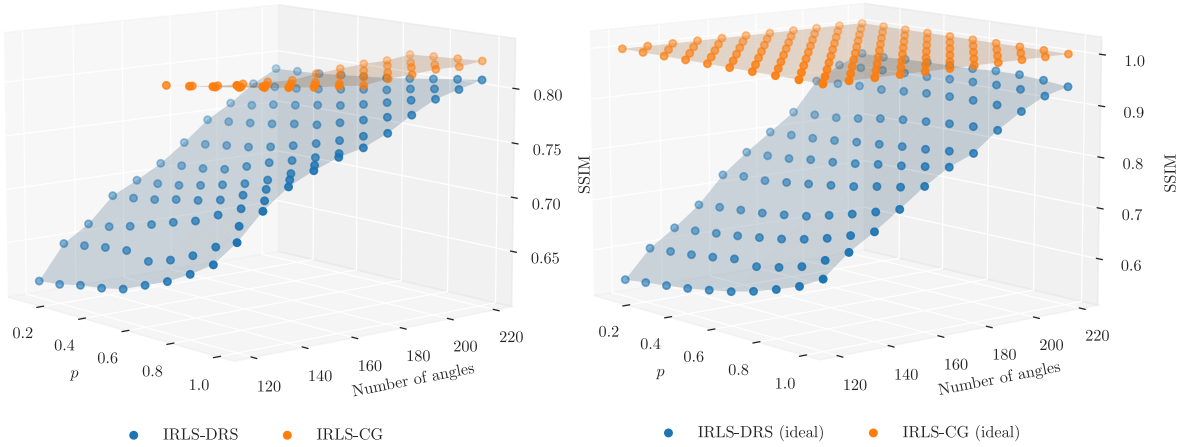

(a) Non-ideal measurements.

(b) Ideal measurements

Figure 5.15 – SSIM achieved by the reconstructions of the Shepp-Logan phantom. Each surface corresponds to a reconstructions algorithm

Similar conclusions are found when evaluating the quality of the reconstructions using SSIM (Figure 5.15).The quality differences between IRLS-DRS and IRLS-CG reconstructions in terms of SSIM seem to be smaller than those observed in terms of SNR. Moreover, SSIM of IRLS-CG reconstructions using ideal measurements varies little with the value of p and the amount of measurement available.

The behavior of the quality of the reconstructions when reducing the value of p is not so evident in the 3D charts we have shown so far. In the plot of Figure 5.16, we can see the SNR of the reconstructions that used measurements on 220 Cartesian radial lines. Figure 5.17 shows the SSIM of these reconstructions. In the case of the non-ideal measurements, both indices indicate a loss of quality for all reconstructions when reducing p. The reconstructions with IRLS-DRS using ideal measurements did not show significant variations in SNR, reaching values just below 30 dB. Regarding SSIM, a small quality gain is noticed if we reduce p to 0.8. On the other hand, IRLS-CG shows SNR variations in the 80 to 90 dB range without a tendency to decrease or increase with p, while SSIM is always very close to 1 regardless of p.

The plots in Figures 5.18 and 5.19 show the quality indices for the reconstructions as a function of the number of angles at which measurements were acquired. In this way, we can compare the performance of the four algorithms used in this experiment. Regarding SNR, IRLS-CG provides the best quality reconstructions, and all algorithms outperform FBP in all tested conditions. IRLS-CG is always close to 17 dB for the non-ideal measurements and 80 dB for the ideal measurements, and in both situations,

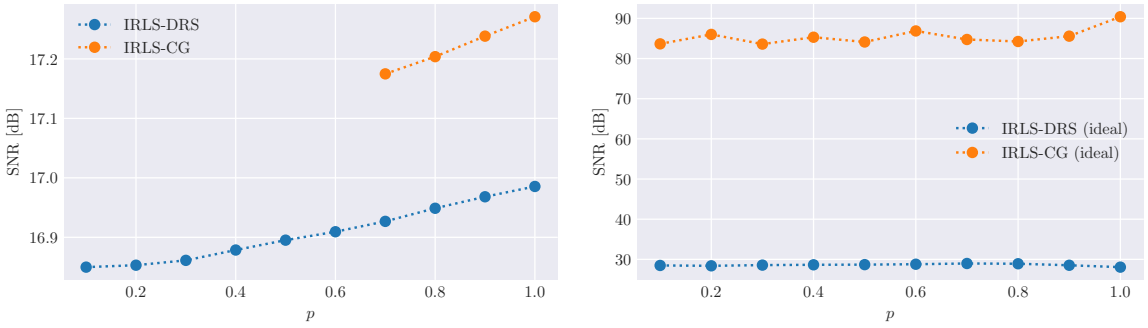

(a) Non-ideal measurements.

(b) Ideal measurements.

Figure 5.16 – SNR achieved by the reconstructions computed using measurements along 220 radial lines of the Shepp-Logan phantom. Each curve corresponds to a reconstruction algorithm.

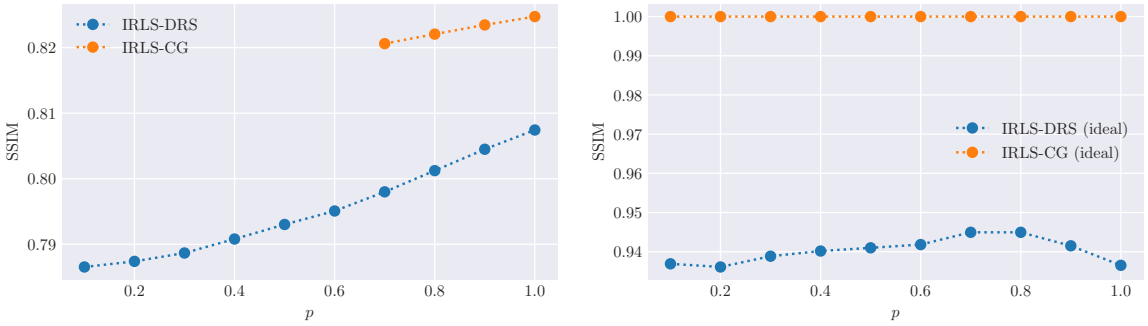

(a) Non-ideal measurements.

(b) Ideal measurements

Figure 5.17 – SSIM achieved by the reconstructions computed using measurements along 220 radial lines of the Shepp-Logan phantom. Each curve corresponds to a reconstruction algorithm.

it does not have significant gains as we increase the number of angles. The MI shows us the reconstruction quality achieved when computing the image using only the measurements acquired on Cartesian radial lines. IRLS-DRS outperforms MI for both types of measurements. This difference indicates the contribution of the coefficients estimated by the CS algorithm to the reconstruction quality.

The SSIM of IRLS-CG reconstructions using ideal measurements is close to 1 regardless of the number of angles. For these measurements, IRLS-DRS outperforms MI, and we notice an improvement in quality as the number of angles increases, with the SSIM going from 0.640 to 0.950. In the case of non-ideal measurements, FBP has a lower SSIM compared to the other algorithms until the reconstruction with 170 angles, when it outperforms IRLS-DRS and MI. After 200 angles, FBP also surpasses IRLS-CG in terms of SSIM.

In some cases, the reconstruction of one algorithm has higher SNR and lower SSIM

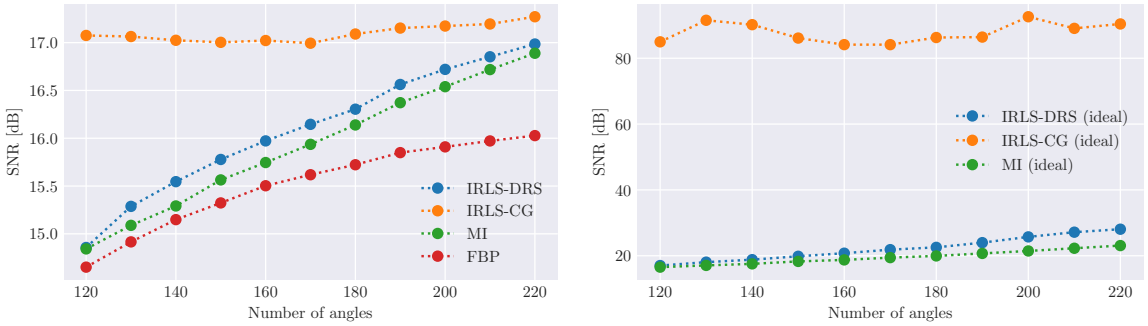

(a) Non-ideal measurements.

(b) Ideal measurements

Figure 5.18 – SNR achieved by the reconstructions of the Shepp-Logan phantom. Each curve corresponds to a reconstruction algorithm. The CS-based approaches used $p = 1$ in the minimization step.

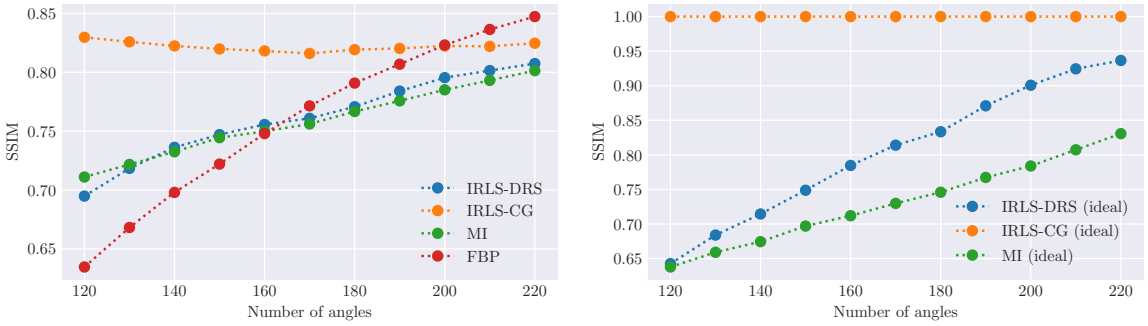

(a) Non-ideal measurements.

(b) Ideal measurements

Figure 5.19 – SSIM achieved by the reconstructions of the Shepp-Logan phantom. Each curve corresponds to a reconstruction algorithm. The CS-based approaches used $p = 1$ in the minimization step.

than a second algorithm's reconstruction under the same conditions. Figure 5.20 shows the reconstruction computed by each algorithm from non-ideal measurements along 200 angles ($p = 1$, in the CS minimizations). These images help us understand how each of the indices translates into visual features. Among these reconstructions, the ones that achieved the lowest SNR (FBP and MI) are those with the most blurred appearance. All images present a textured aspect in areas of the phantom that are originally uniform. The reconstruction of IRLS-CG exhibits this pattern less noticeably. The FBP reconstruction has the biggest artifacts in the region outside the ellipses. Compared to FBP, the IRLS-DRS reconstruction has a more grayish appearance, which is in accordance with their SSIM values. We emphasize that all images are very similar to each other so that these differences are noticed when looking at them more comprehensively.

A second worthwhile visual comparison to discuss is the reconstructions from the smallest amount of measurements we tested, with 120 angles. Under these conditions,

the difference between the images is more noticeable, as can be seen in Figure 5.21. The textured aspect most affects the reconstructions with FBP and MI. Two features distinguish the reconstructions with IRLS-CG and IRLS-DRS more clearly: (i) a more grayish appearance in the reconstruction that used the direct method, as well as (ii) the more pronounced presence of vertical artifacts, which is likely to be a consequence of the CS minimizations being calculated for each row of measurements.

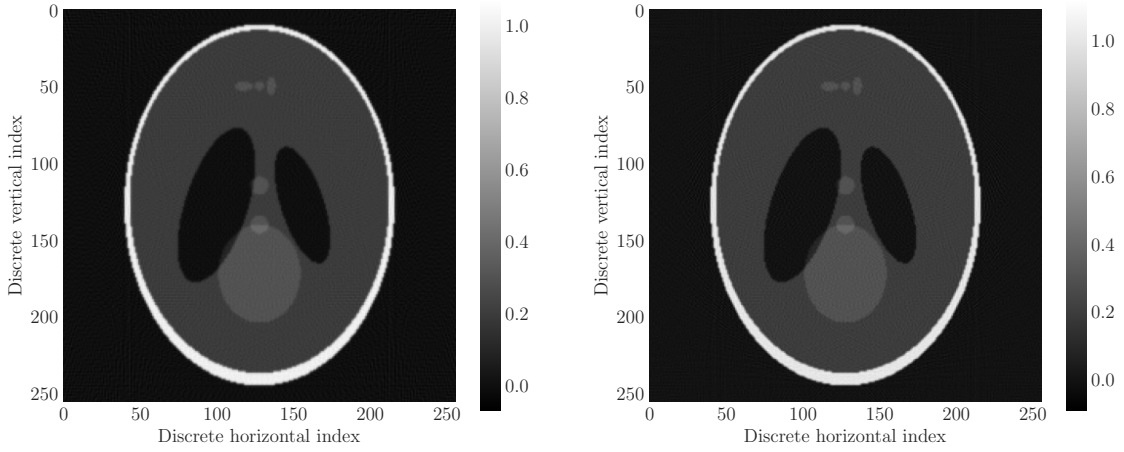

(a) FBP.

(b) MI.

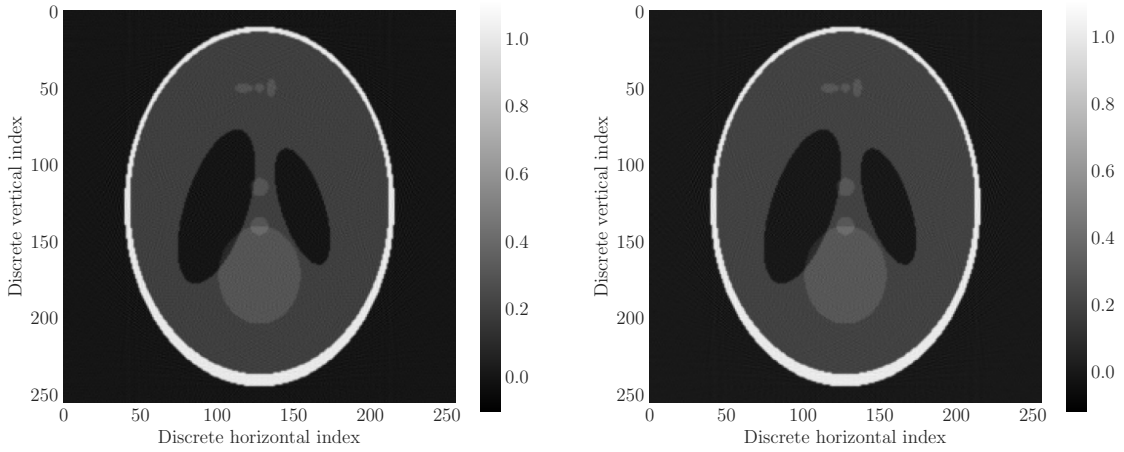

(c) IRLS-DRS ($p = 1$).

(d) IRLS-CG ($p = 1$).

Figure 5.20 – Reconstructions of the Shepp-Logan phantom from non-ideal measurements taken in 200 angles.

Figure 5.22 shows the reconstructions of the actual MR1 image calculated with ideal measurements taken at 170 angles. They all have an SSIM above 0.9. Thus, the main structures of the image are well preserved in all reconstructions, so looking carelessly at them will not reveal much difference between them. However, this slight difference in SSIM is enough to realize that the reconstructions with FBP and MI are more grayish and present less contrast than reconstructions with IRLS-DRS and IRLS-CG.

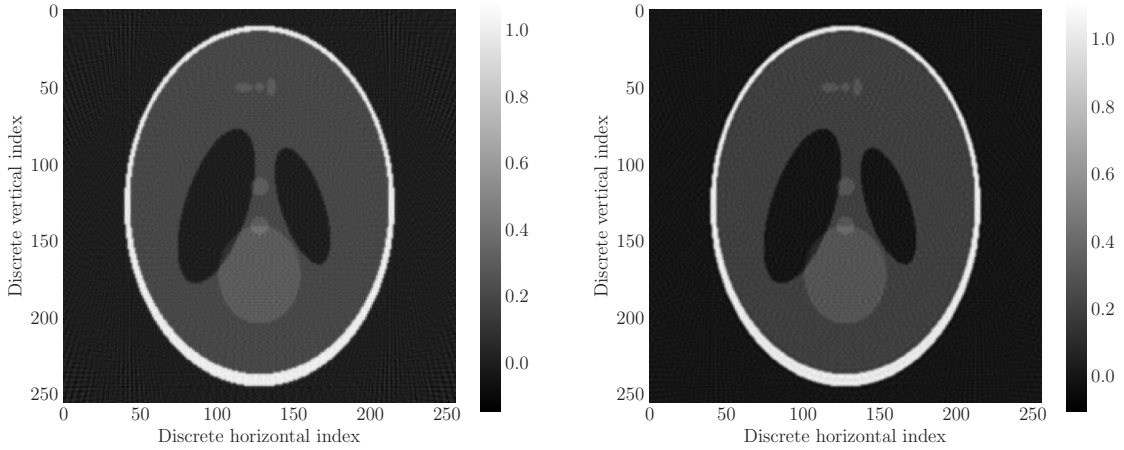

(a) FBP.

(b) MI.

(c) IRLS-DRS ($p = 1$).

(d) IRLS-CG ($p = 1$).

Figure 5.21 – Reconstructions of the Shepp-Logan phantom from non-ideal measurements taken in 120 angles.

In addition, reconstruction artifacts in the form of radial lines are more pronounced in the FBP reconstruction, which showed lower quality scores.

Staying with the examples in Figure 5.22, the SNR indicates higher quality differences between the reconstructions. It again is easier to see the image degradation in the case of the FBP reconstruction. In general, reconstructions with lower SNR show a more granulated texture in more uniform regions of the original image. Appendix B provides images of further examples of reconstructions.

In the following, we will comment on further aspects that can be noticed when analyzing the reconstructions of the actual images. More plots regarding these reconstructions can be found in Appendix A. Prefiltering generates signals with 95% null values for the Shepp-Logan phantom. In the case of CT2, the achieved sparsity is considerably lower, with no more than 12% of null entries. Thus, the actual im-

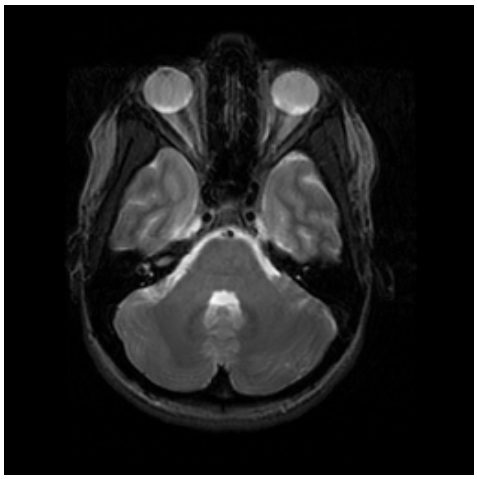

(a) Testing image.

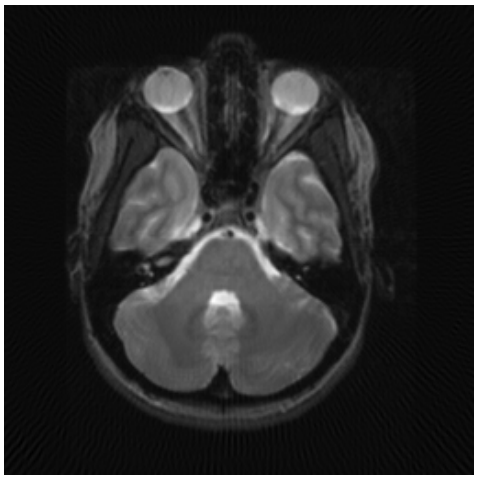

(b) FBP.
SNR = 23.3 dB
SSIM = 0.946

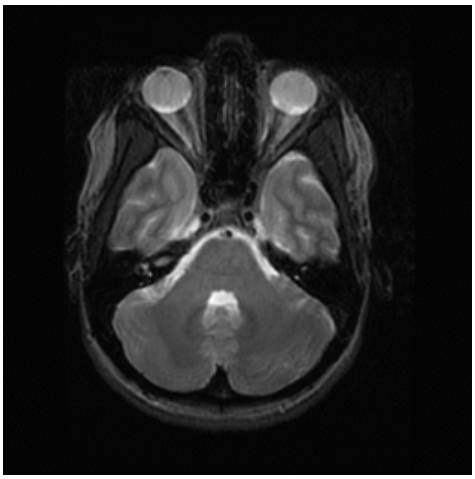

(c) MI.
SNR = 31.6 dB
SSIM = 0.985

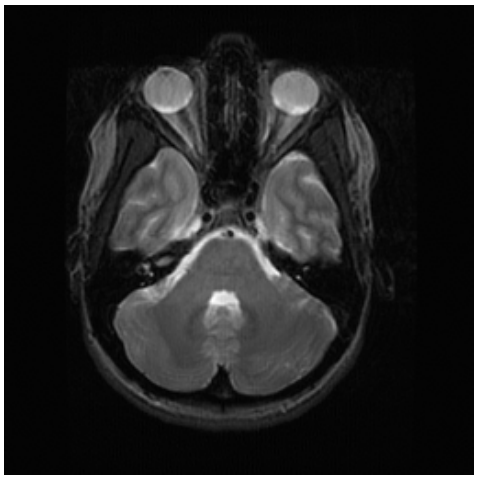

(d) IRLS-DRS ($p = 1$).
SNR = 33.4 dB
SSIM = 0.992

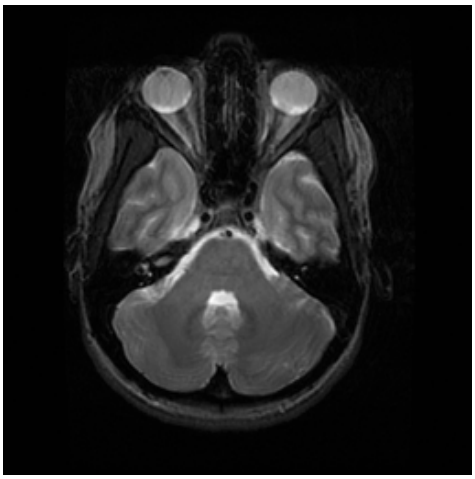

(e) IRLS-CG ($p = 1$).
SNR = 40.7 dB
SSIM = 0.998

Figure 5.22 – Reconstructions of the MR1 actual image from measurements taken in 170 angles. We chose to omit the axes in the representation of the images so that they would all fit on a single page.

age reconstructions are expected to have lower-quality levels than the phantom when computed by CS approaches.

Figure 5.23 presents the SNR of the CT2 image reconstructions ($p = 1$ in IRLS-CG and IRLS-DRS). A fact that draws attention is that the reconstructions by MI outperform those by IRLS-DRS, while IRLS-CG continues to obtain the best SNRs in all scenarios. It suggests that the lower sparsity prefiltering generated for CT2 affected IRLS-DRS more significantly than IRLS-CG. For the ideal measurements, the curves of CT2 reconstructions are indeed in a region of lower SNR than those of the Shepp-Logan phantom, especially IRLS-CG. Intriguingly, the SNRs observed for CT2 are higher than those of the phantom for the non-ideal measurements, exceeding 27 dB in the best cases. In addition, the increasing behavior of SNR with the number of angles is observed in all algorithms for ideal and non-ideal measurements.

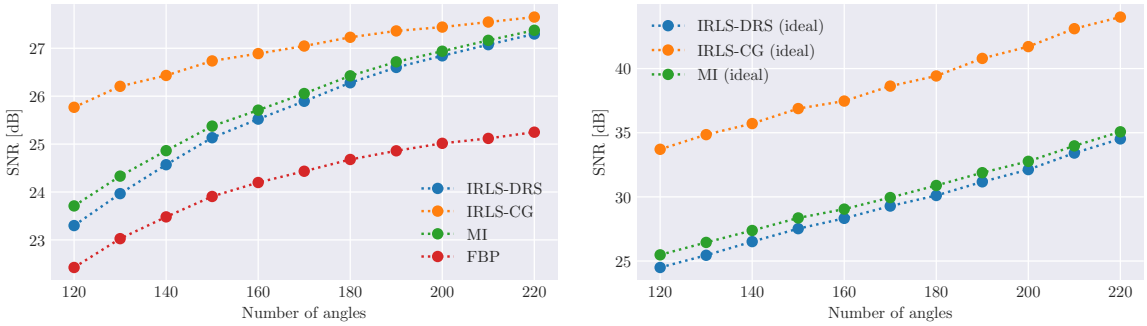

(a) Non-ideal measurements.

(b) Ideal measurements

Figure 5.23 – SNR achieved by the reconstructions of the CT2 actual image. Each curve corresponds to a reconstruction algorithm. The CS-based approaches used $p = 1$ in the minimization step.

In Figure 5.24, SSIM increases when more information is available for the CT2 reconstructions, which is consistent with the discussions based on SNR. Unlike what happened with the phantom, the SSIMs of the FBP reconstructions are always below all the other algorithms. One hypothesis to explain this behavior is that the phantom has larger uniform regions, so the reconstruction artifacts in these areas affect the perception of the image elements more than in the case of CT2, which has more information in high-frequency coefficients. The question remains as to why the FBP is less affected than the CS-based algorithms by this issue.

The SNR and SSIM values for MR2 actual image are shown in Figure 5.25. These reconstructions were computed from ideal measurements, and the CS algorithms adopted $p = 1$. The testing MR images achieved with prefiltering a sparsity level higher than that of the CT images but lower than that of the Shepp-Logan phantom (about 28% null inputs). Accordingly, the IRLS-DRS outperformed the MI in all conditions we

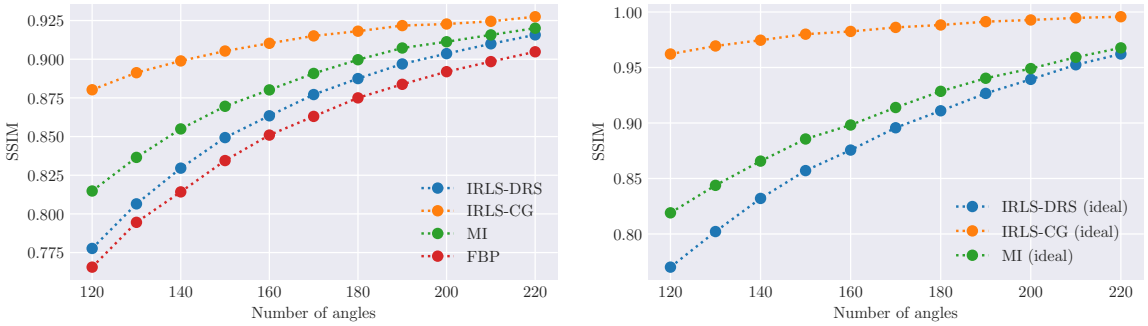

(a) Non-ideal measurements.

(b) Ideal measurements

Figure 5.24 – SSIM achieved by the reconstructions of the CT2 actual image. Each curve corresponds to a reconstruction algorithm. The CS-based approaches used $p = 1$ in the minimization step.

tested for the reconstructions of MR2. The SNR and SSIM levels are better than those observed for the CT2 image, but we also see a quality improvement in the results for all algorithms as the number of angles increases. It indicates that the margin for reducing the number of measurements is as wide as the sparsity of the signals computed in the minimization step.

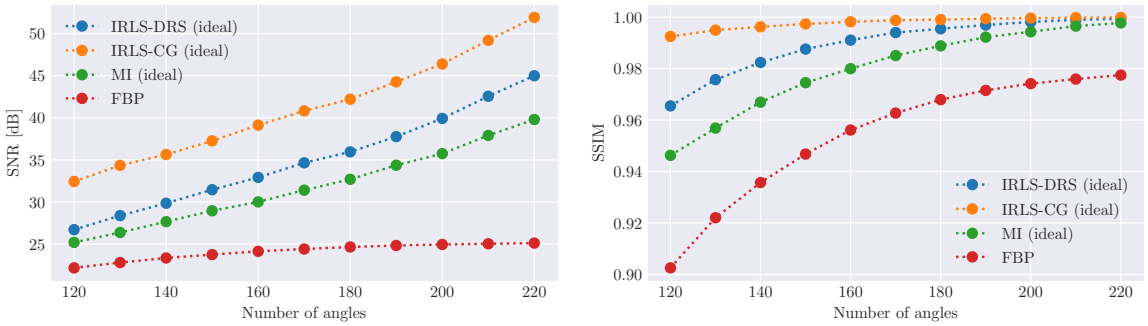

(a) SNR.

(b) SSIM.

Figure 5.25 – Quality indices achieved by the reconstructions of the MR2 actual image. Each curve corresponds to a reconstruction algorithm. The CS-based approaches used $p = 1$ in the minimization step.

Lastly, Figures 5.26 and 5.27 show the times for running some of the reconstructions of the Shepp-Logan phantom and CT2. The plots comprise reconstructions with 120 measurements computed by IRLS-DRS and IRLS-CG. In general, the execution time tends to decrease by reducing p when using the direct method. For the indirect method, the algorithm takes longer for smaller values of p. Thus, IRLS-CG is faster than IRLS-DRS for higher p, but for lower values, this reverses. We reiterate that we have presented these runtime values to get a rough idea of the computational effort required by the algorithms we tested. More extensive evaluations with more testing signals and

repetitions should be conducted to understand this topic satisfactorily.

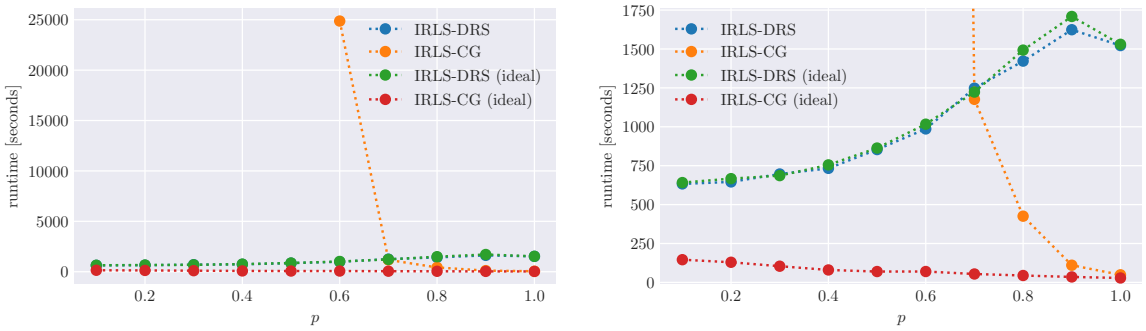

(a) For all reconstructions.

(b) In detail.

Figure 5.26 – Runtime for each CS-based algorithm when reconstructing the Shepp-Logan phantom using ideal and non-ideal measurements along 120 angles.

The results of this experiment show that IRLS-CG outperforms IRLS-DRS in terms of SNR and SSIM in all tested conditions. We believe this is because prefiltering is a more efficient sparsity representation for the signals computed by ℓ_p minimization in the case of IRLS-CG. Thus, the IRLS-DRS reconstructions achieve lower quality because the one-dimensional signals do not have a sparsity representation through prefiltering. Experiment 3 will investigate this hypothesis.

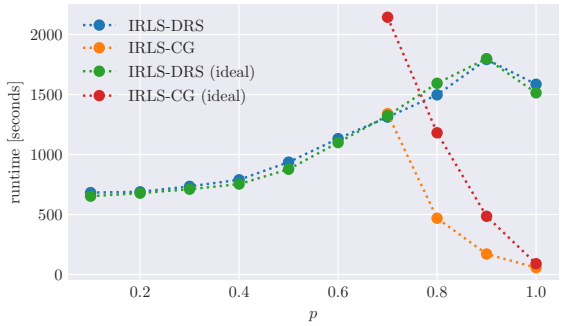

Figure 5.27 – Runtime for each CS-based algorithm when reconstructing the CT2 actual image using ideal and non-ideal measurements along 120 angles.

The reconstructions with non-ideal measurements achieved lower quality than those with ideal measurements. This difference illustrates the impact that the conversion procedure from sinogram projections to measurements in the frequency plane has on the quality of CT images. Experiment 4 will address this conversion error introduced into the reconstructions.

5.5 Experiment 3 – reconstructions of synthetic images sparse on 1D domain

As discussed in the previous section, the results obtained using IRLS-CG are better than those obtained by IRLS-DRS, considering that prefiltering is used in both situations. A starting hypothesis to explain these results is that prefiltering is a more efficient strategy to represent the sparsity of signals that IRLS-CG reconstructs than the one-dimensional signals reconstructed by IRLS-DRS. In this manner, the conditions for sparse reconstruction would be more favorable in the indirect case, and another strategy for representing sparsity more efficiently should be adopted in the DRS.

As an example, consider the formation of the Shepp-Logan phantom using prefiltering. One step consists of reconstructing a version of the image filtered with the diagonal Haar high-pass kernel. When using the indirect method, the signal obtained in the minimization stage is the filtered image itself. In contrast, the DRS computes a CS minimization for each row in the frequency plane. Figure 5.28 shows examples of signals reconstructed in each of the approaches. In this example with the Shepp-Logan phantom, the signal reconstructed with the indirect method has 97.8% of its values below 10^{-6} (in magnitude), whereas, for the signal reconstructed with the direct method, only 31.25% of its inputs have a magnitude less than 10^{-6}. It illustrates that prefiltering is more efficient in sparsifying the signals reconstructed by the indirect method approach.

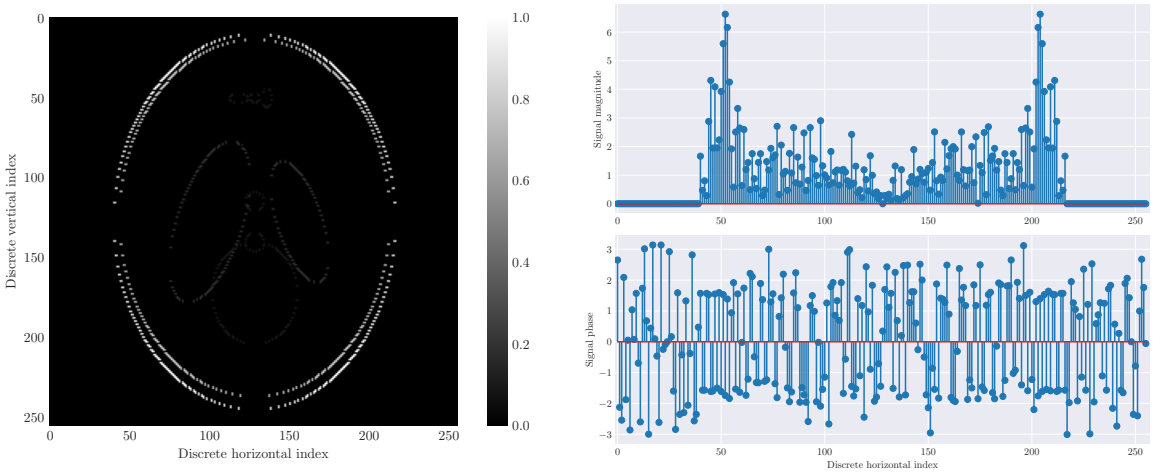

(a) Shepp-Logan phantom sparsified by the diagonal Haar kernel (inderect method).

(b) The 1D signal related to the 50$^{\text{th}}$ row of the same sparsified phantom (direct method).

Figure 5.28 – Examples of signals reconstructed by CS minimization using direct and indirect methods to form the Shepp-Logan phantom using prefiltering as the sparsity representation strategy.

To verify the performance of IRLS-DRS in a scenario with an efficient sparse rep-

resentation for the one-dimensional signals, we have elaborated synthetic images with such one-dimensional signals sparse in any known domain. Thus, we can evaluate the hypothesis we raised to explain the better performance of IRLS with the direct method. Furthermore, if the sparsity representation indeed impairs the performance of DRS, its results can be improved by developing more efficient strategies than prefiltering for one-dimensional signals.

5.5.1 Synthetic image generation

The synthetic images are created from actual medical images. The procedure to generate them consists in calculating the one-dimensional signals and setting part of their components to zero in a transformed domain. The definition of the sparsifying transform and the selection of which positions are part of the support are done using random distribution generators. The image is recomposed again from the one-dimensional sparsified signals.

The resulting signal in the frequency plane loses the spectral symmetry expected for real-valued images because of zeroing out some elements of the one-dimensional signals in the transformed domain. So, the inversion of this spectrum into the pixel domain results in a complex signal. As we verified experimentally, the real part of this resulting signal preserves the intended sparsity features. Thus, the real part of this complex signal can be adopted as the desired synthetic image. Finally, the image is normalized, so all of its pixels will be between 0 and 1. Algorithm 5.1 shows how we implemented this synthetic image generator.

5.5.2 Simulation methodology

We selected 4 CT images and 4 MR images for generating the synthetic images. All of them are of shape 256×256. Four synthetic images were created for each of the actual medical images, each with a different support size ($60\%, 70\%, 80\%$ and 90% of null values), totaling 32 phantoms for performing the reconstruction tests. Observe that images created by zeroing 90% of the entries in the transformed domain are the sparsest, while those that zeroed 60% of the elements are the less sparse. We compute reconstructions with IRLS-DRS from ideal measurements under the conditions reported in Section 5.3. Figure 5.29 shows an example of an image used in this simulation and the actual image used to generate it.

Algorithm 5.1 Generation of a synthetic image that is sparse in a one-dimensional transformed domain.

Input: Actual medical image I, percentage p of values to be zeroed
Output: The synthetic image S and the sparsifying transform matrix T

1: Set M as the matrix whose columns are the DFT of the corresponding column in the actual medical image I
2: Create a zero matrix H of the same shape as I
3: Set the sparsifying transform by choosing a matrix T using a random generator (Gaussian distribution with zero mean and unit variance)
4: **for** each row y_i of the matrix M **do**
5: Calculates the row in the sparse domain ($\hat{y}_i = Ty_i$)
6: Replace some elements of $\hat{y}_i$ with zeros in random positions according to the percentage p
7: Replace the i-th row of H with $T^{-1}\hat{y}_i$
8: **end for**
9: Set G as the matrix whose columns are real part of the IDFT of the corresponding column in the matrix H
10: The desired synthetic image S is the matrix G with its values linearly remapped to the $[0, 1]$ interval

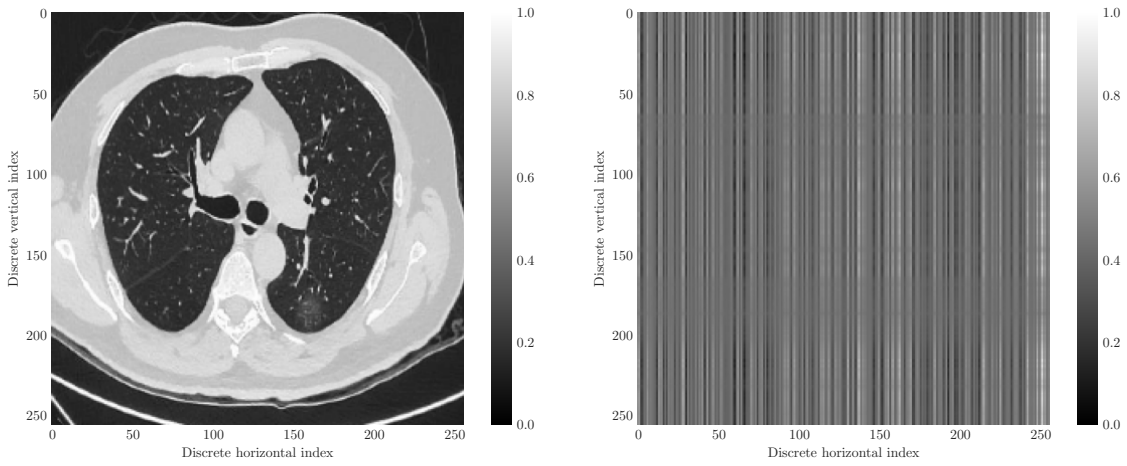

(a) Original CT image

(b) Synthetic image

Figure 5.29 – Example of a synthetic image created by replacing with zeros 60% of the entries of the one-dimensional signals of an actual 256×256 CT image.

5.5.3 Results and discussion

The procedure that generates the synthetic images mischaracterizes them in the pixel domain so that the resulting image has a vertical noise aspect and no visual meaning (no shape is easily identified). So, the discussion of the results we will present here concerns only the analysis of the SNR achieved by the reconstructions. The results of every reconstruction of a synthetic image are displayed in Figures 5.30 and 5.31.

Reconstructions of the same testing image form a single surface on the charts. In general, these curves behave as expected: the quality of the reconstruction increases as the amount of measurements increases or as the value of p reduces.

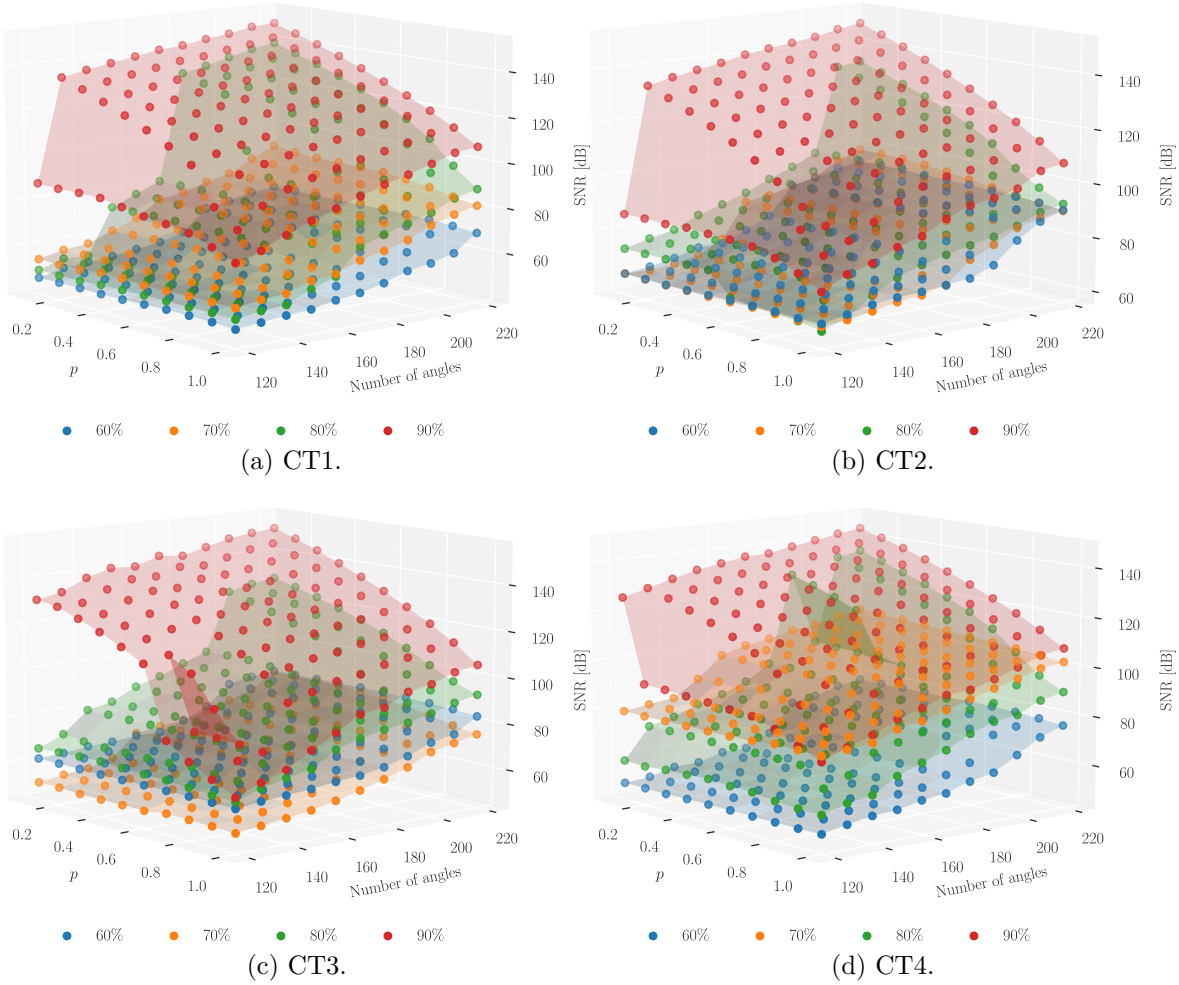

(a) CT1.

(b) CT2.

(c) CT3.

(d) CT4.

Figure 5.30 – SNR achieved by the reconstructions of the synthetic images generated from actual CT images. Each surface corresponds to every reconstruction of the same synthetic image (the colors identify the percentage of null elements in the sparse one-dimensional signals). Each chart gathers data from artificial images generated from the same actual image (indicated in the caption beneath).

Another behavior that becomes apparent in the graphics is the tendency for better results for the images whose one-dimensional signals are more sparse in the transformed domain. There are some exceptions; in Figure 5.31d, for example, it is noticeable that the reconstructions of the image with 70% of null values in the sparse domain are worse than the image with 60% of null values. Nevertheless, the quality of the reconstructions of the synthetically sparse images surpasses what was observed in the reconstructions of the actual medical images using prefiltering. This simulation's worst results (highest p and fewer angles) have an SNR close to 40 dB, while the best (lowest p and more angles) exceed 120 dB.

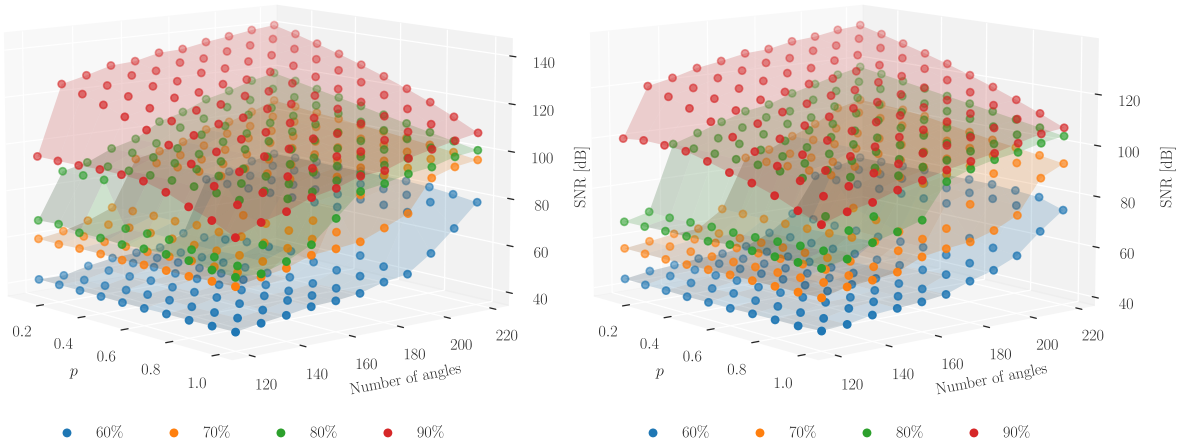

(a) MR1.

(b) MR2.

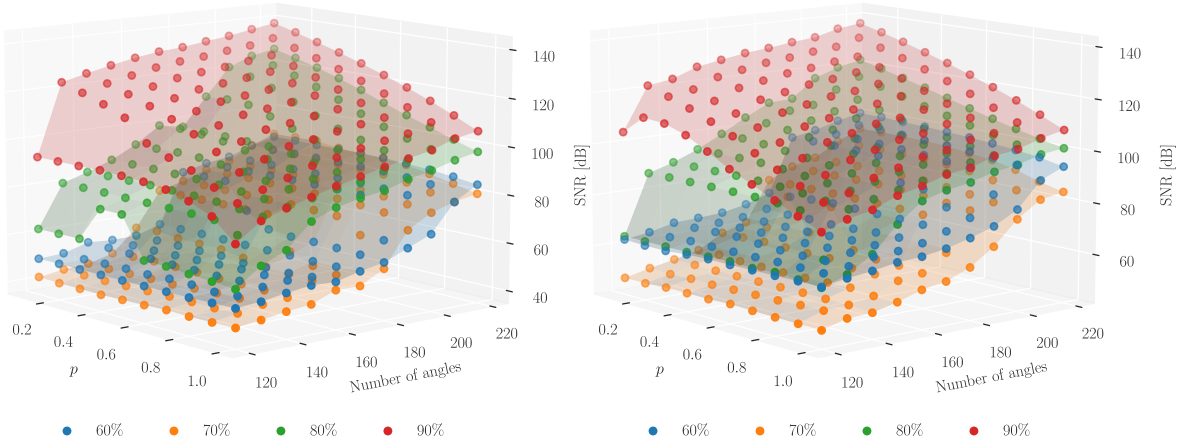

(c) MR3.

(d) MR4.

Figure 5.31 – SNR achieved by the reconstructions of the synthetic images generated from actual MR images. Each surface corresponds to every reconstruction of the same synthetic image (the colors identify the percentage of null elements in the sparse one-dimensional signals). Each chart gathers data from artificial images generated from the same actual image (indicated in the caption beneath).

Figure 5.32 shows in detail the SNR of reconstructions of the synthetic images generated from the actual image CT1 for some specific number of angles. It means these plots are a few planes from Figure 5.30a for fixed values of angles. In this way, it is possible to notice more easily that as we increase the number of angles, the value of p becomes more significant in the quality of the reconstructions, especially in those images composed of sparser signals (80% and 90% of null values in the sparse domain).

In the reconstructions computed from measurements taken in 120 angles, the ℓ_p metric adopted does not make a significant difference for images with lower sparsity (60%, 70%, and 80%) since there is a minimal variation in SNR as the value of p changes. In the case where the measurements are along 150 angles, the image with a sparsity level at 80% has better reconstructions for $p \leq 0.8$, although there is no significant variation from that point. In the graphs for 180 and 210 angles, this increasing behav-

ior of the SNR by reducing p becomes more pronounced for all images. It indicates that in better-conditioned situations (greater sparsity and quantity of measurements), adopting metrics with lower p leads to higher quality reconstructions.

The experiment of reconstructing the synthetic images with the sparsity characteristics as expected by DRS showed that this is a possible strategy for medical imaging. However, this requires developing a sparsity representation strategy appropriate for the one-dimensional signals. Furthermore, the results we presented indicate that the more efficient the sparse representation is, the more advantage can be obtained in reducing the value of p. In this sense, we can mention a better reconstruction quality and reduced execution time (IRLS tends to converge in fewer iterations to lower values of p, and the matrix products no longer rely on indirect methods).

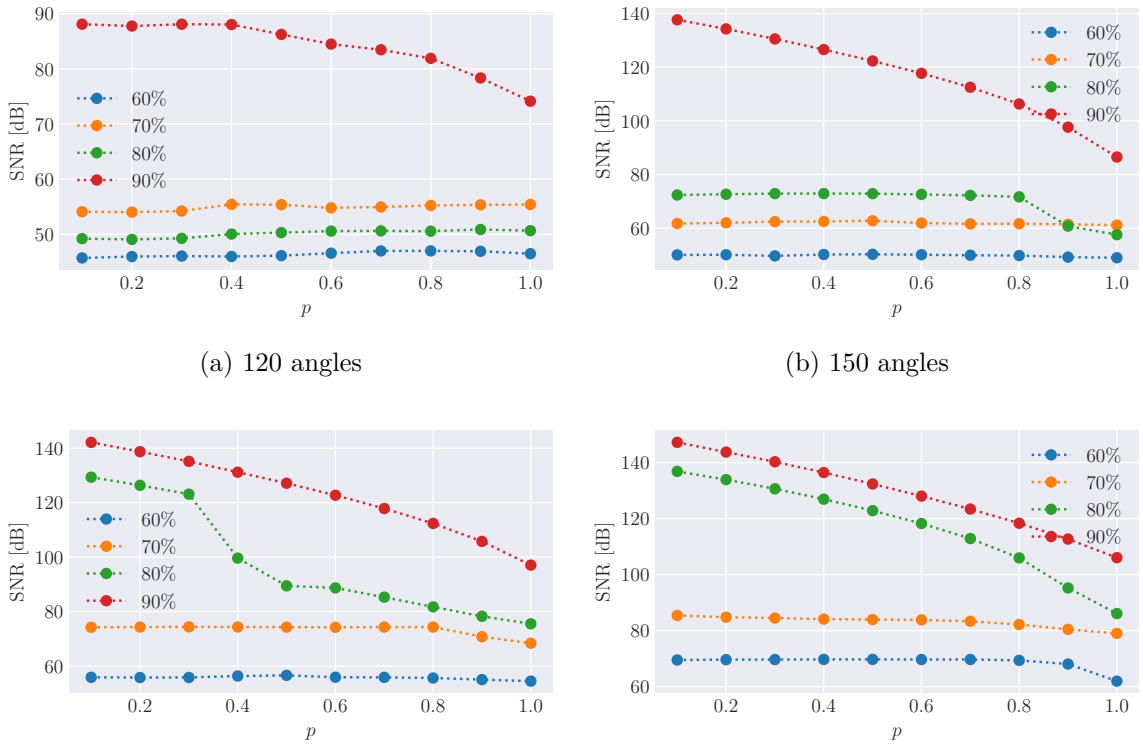

(a) 120 angles

(b) 150 angles

(c) 180 angles

(d) 210 angles

Figure 5.32 – SNR achieved by some reconstructions of the synthetic images generated from the actual image CT1. Each curve corresponds to every reconstruction of the same synthetic image (the colors identify the percentage of null elements in the sparse one-dimensional signals). Each chart gathers data from reconstructions from measurements taken in the same amount of angles (indicated in the caption beneath).

5.6 Experiment 4 – the effect of the interpolations on the computation of the measurements on the Cartesian grid from a sinogram

As discussed in Section 3.6.2, in the case where non-ideal measurements are used for CT image reconstruction, we estimate part of the spectral content of the images from interpolations of the sinogram columns and the FST. The CS algorithms use these interpolated measurements to compute the spectral components at the remaining positions in the frequency plane. Thus, the Cartesian positions whose angular coordinates are closest to the angles at which the projections were acquired have their spectral content estimated from the sinogram. Equation 3.37 shows the criterion we adopted, which relies on a tolerance variable (tol). The higher tol is, the more positions are calculated directly from the sinogram. In principle, the larger the tolerance, the more information is available to the CS algorithm, and better results are obtained. However, the interpolation step adds error to the measurements so that after particular tolerance values, the reconstruction quality is impaired.

5.6.1 Simulation methodology

In this experiment, we conducted new reconstructions of the 256×256 Shepp-Logan phantom. We took into account different values for the tolerance when choosing which positions in the Cartesian frequency plane is a measurement estimated from interpolation of the sinogram columns. Moreover, we have also observed the error behavior as the tolerance varies when estimating the measurements from the sinogram. Only FBP was not evaluated in this simulation since it does not require the measurements to be in the frequency plane. All reconstructions used measurements taken at 120 angles with $tol \in \{0.1, 0.2, \cdots, 1.2, 1.3\}$. Figure 5.33 shows how many of the positions in the Cartesian grid are measurements for each value of tol.

5.6.2 Results and discussion

Before moving on to the reconstructions, we examine how much error is added to the measurements due to the interpolations. To that end, we compute the measurements for each tolerance value according to Algorithm 3.3. Then, we calculate the difference between these estimated measurements and the 2D-DFT coefficients at the positions of the Cartesian radial lines. The normalized mean error in Figure 5.34 is the mean of the magnitude of these differences divided by the mean of the magnitude of the phantom spectrum at the Cartesian radial lines. As expected, larger tolerances lead to higher interpolation error, which is seen in the impairment of the reconstructions quality.

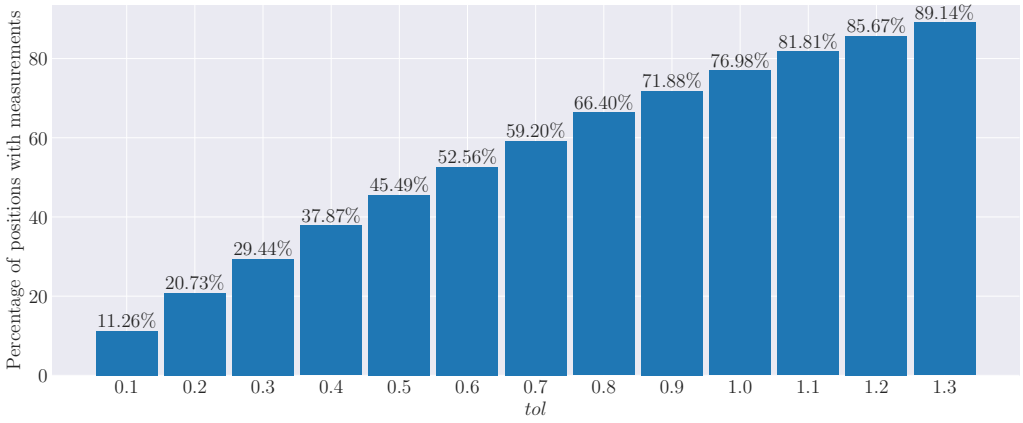

Figure 5.33 – Percentage of positions in the 256×256 grid that are measurements for each tolerance value when defining the Cartesian radial lines with 120 angles.

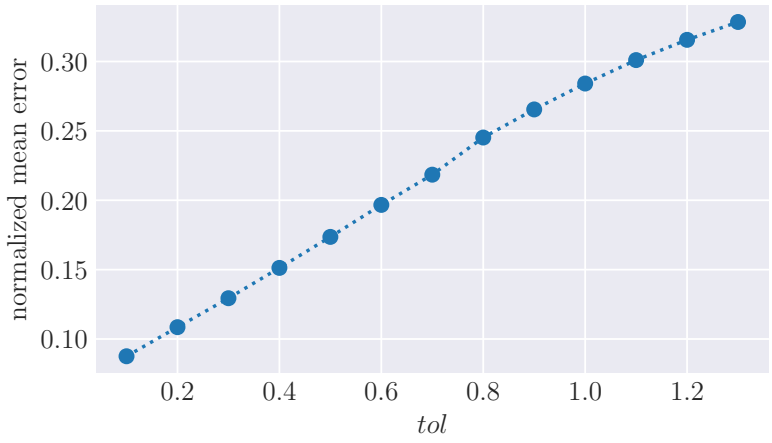

Figure 5.34 – Error in the estimation of measurements of the 256×256 Shepp-Logan phantom in the Cartesian radial lines from 120 projections for different values of tolerance.

The algorithm that interpolates projections to estimate spectral information at locations on the Cartesian grid can also be understood as a method for reconstructing CT images per se. We can simply calculate all the coefficients of the frequency plane instead of computing only for some positions on radial lines, as is done to estimate the measurements used in the CS algorithms. In the case where all the spectrum is estimated from the sinogram by Algorithm 3.3, the reconstructed image achieves SNR = 15.4 dB and SSIM = 0.762.

When combining the measurement interpolation algorithm with a CS algorithm, we are assuming that the ℓ_p minimization is a more accurate method for estimating the spectral information at the Cartesian positions more distant from the angles at which the projections were taken. Indeed, this is what we see in the SNR and SSIM plots in Figure 5.35 for the IRLS-CG reconstructions. For $tol = 0.1$, the IRLS-CG

obtained better-quality images than the reconstruction with only the interpolations of the projections (SNR = 16.4 dB and SSIM = 0.807). The quality of the reconstruction increases until $tol = 0.3$; from then on, the quality decreases until stabilizing at the indices achieved by reconstructing just interpolating the projections.

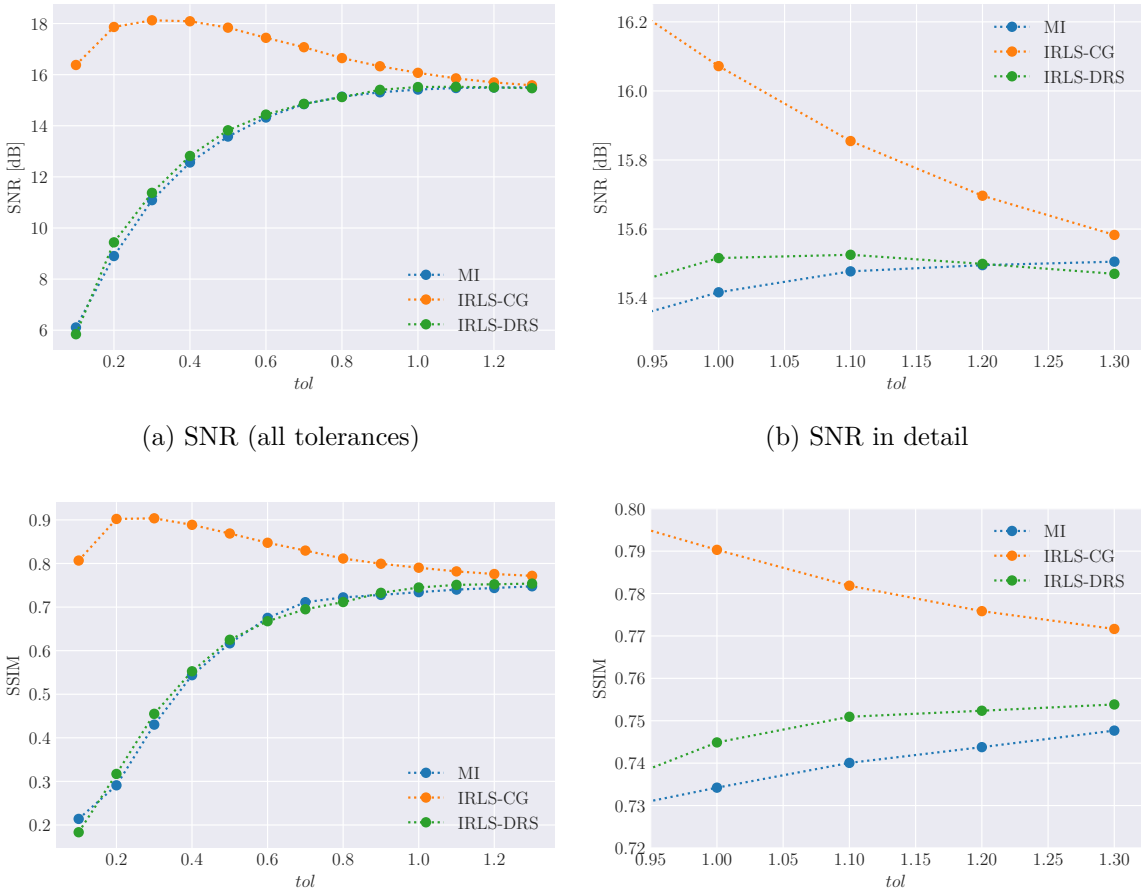

(a) SNR (all tolerances)

(b) SNR in detail

(c) SSIM (all tolerances)

(d) SSIM in detail

Figure 5.35 – Quality of reconstructions of the Shepp-Logan phantom in terms of SNR and SSIM when using Cartesian radial lines defined with different tolerance values.

In the case of MI and IRLS-DRS, the reconstructions start from inferior quality and approximate the standard of the reconstruction only by interpolation. Therefore, both algorithms are less effective in estimating the spectral components at positions outside the Cartesian radial lines. That is consistent with the discussion in Section 5.4, given that IRLS-DRS does not have an efficient sparse representation with prefiltering and is, therefore, more affected by interpolation errors. In this regard, MI completes with zeros the positions where there are no measurements. Finally, it is of particular interest to note that IRLS-DRS has its best reconstruction in terms of SNR for $tol = 1.1$, then the SNR gradually decays for larger values of tolerance until it reaches 15.4 dB.

5.7 Compilation of the discussion of all experiments

Our investigations began from the assumption that reducing the value of p in the definition of the ℓ_p minimization problem allows CS algorithms to recover signals from less information. This premise, if proven true, would support the development of faster and safer medical imaging techniques. The first experiment verifies this intuition that smaller p values lead to higher quality reconstructions. The sparsity conditions must be favorable for this to be well exploited. Moreover, we found more margin for reduction of p when using the direct method. We also point out that the settings of the reconstruction algorithm affect the ability to improve the quality of the results by reducing p.

The second experiment compares the direct and indirect methods for reconstructing medical images. Prefeiltering was the strategy for sparse representation adopted in this experiment. The approach using the indirect method outperformed the direct method due to sparsity conditions that were more favorable for the signals reconstructed by the formulation using the indirect method. The third experiment shows that IRLS-DRS obtains better reconstructions under more favorable sparsity conditions. So, the gains seen in the first experiment can be achieved in medical imaging as long as there is an efficient sparsity strategy for the one-dimensional signals reconstructed in the proposed DRS model.

In the case of CT, the measurements correspond to samples of the Radon Transform of the image. Since the IRLS-CG and IRLS-DRS expect the measurements to be in the Fourier domain, we used Algorithm 3.3 to arrange the measurements in the Cartesian frequency plane. In this process, we must define which discrete positions belong to the radial lines, which we did through a tolerance criterion. The fourth experiment gave a better sense of how the errors of this conversion impair reconstruction quality.

We remind that CS reconstructions have always used IRLS as the minimizer. As verified in the experiments, this iterative algorithm depends on some parameters, and the results are pretty sensitive to them. Changing such parameters may favor or impair the reconstruction in some contexts. Therefore, adjusting the CS-solver is important for satisfactory results in the applications of interest. Furthermore, the chosen images allowed an initial analysis of the IRLS-DRS performance, but they contemplated a limited number of structures found in medical images (breast and head). Future evaluations of the algorithm should cover a more significant number of testing images to consider structures observed in different regions of the human body.

Chapter 6

Conclusion

The design of medical imaging algorithms that rely on small quantities of measurements is a pertinent contribution to the subject. As a result, measurement acquisition schemes become faster and safer. In recent years Compressive Sensing has been used as a strategy for the development of new image reconstruction techniques. However, indirect methods are often used due to the size of the signals that represent images. In this thesis, we are concerned with investigating the gains of reconstructing medical images using direct methods in the CS algorithm.

The main result of the present research is the proposed Direct Reconstruction Structure for CT and MR images. It is a flexible approach for designing CS-based medical imaging algorithms that use a direct method in the minimization step. We claim such flexibility in the sense that distinct algorithms can be devised by changing the image composition strategies or the CS-solver. We have modeled a specific formulation of DRS, where the reconstructed signals concern the contributions of a single row of measurements to the formation of the image in the pixel domain. We have implemented this DRS derivation using IRLS as the CS-solver, which we denoted as IRLS-DRS. The discussions we have presented are based on comparisons of objective parameters for reconstructions from IRLS-DRS, IRLS-CG, FBP, and MI.

At the first moment, we have adopted prefiltering as a strategy for sparsity representation. We found that this approach is more efficient for generating sparse signals in the case of IRLS-CG. Hence, the results using the CG method were more satisfactory than those of IRLS-DRS in reconstructing the Shepp-Logan phantom and the actual images. We then produced synthetic images whose one-dimensional signals that form them are sparse in a known domain. With this, we were able to evaluate the performance of IRLS-DRS in the situation where there is a more appropriate sparse representation. For these new images, the results indicate that better reconstruction qualities can be achieved for the same set of measurements by reducing p. This behav-

ior is best observed especially in situations where the sparse reconstruction conditions are the more favorable, i.e., higher sparsity level and more measurements available.

In the case of MR, there is more freedom regarding the arrangement of the measurements since different trajectories are obtained by changing the sequence of pulses emitted during the acquisition. For CT, the measurements are projections that, to be used by IRLS-DRS and IRLS-CG, must be converted into samples in the frequency domain arranged in radial lines. This process employs the Fourier Slice Theorem and interpolations, which introduces error to the measurements. One of the computational experiments showed the impact of this step on the quality of the reconstructed images as a function of the tolerance parameter used to define which Cartesian positions would have their coefficients calculated directly from the projections. Since prefiltering is more appropriate for signals reconstructed with IRLS-CG, we verified only in this algorithm the expected behavior. The reconstruction quality increases up to a given tolerance value, after which the effect of the error becomes more significant than the information provided by more interpolated measurements.

6.1 Summary of contributions

In view of the research objectives outlined in Section 1.3, we now list the scientific contributions achieved in the course of developing the DRS:

1. Investigation of the effect of reducing the value of p in a general case of ℓ_p minimization for CS signal reconstruction. We have shown with a numerical experiment that better results are obtained as the value of p is reduced in situations where there are good conditions for sparse reconstruction. Our analyzes also found that the algorithm settings may interfere with the ability to achieve such behavior.

2. The development of mathematical formalism for general DRS implementations and for a specific formulation based on the reconstruction of one-dimensional signals that contain the spectral information in a single row of measurements in the frequency plane.

3. Through that particular implementation of DRS, we were able to evaluate the use of a direct method for medical imaging using IRLS as the ℓ_p minimization algorithm. We made comparisons with reconstructions using CG. In the examples with the Shepp-Logan phantom and with actual images, IRLS-CG outperformed IRLS-DRS because prefiltering proved to be a more efficient sparse representation strategy for the signals reconstructed in the model using the indirect method.

When reconstructing artificial images with good sparsity characteristics for DRS, the reconstructions with the direct method achieved a higher quality level in terms of SNR.

4. We have proposed modifications to the algorithm for calculating measurements in the frequency plane from the sinogram, used in CT reconstruction by IRLS-CG and IRLS-DRS. We made two changes in the original formulation (introduced in [9]), which accelerated the runtime: (i) two-dimensional interpolation and (ii) the use of the Goertzel algorithm to calculate specific samples of the DTFT.

5. Evaluation of the effect of the tolerance variable when defining which positions of the Cartesian grid will be estimated from projection interpolations and which are computed using the CS algorithm.

6.2 Published works

Part of the results presented in this thesis was previously published in a paper in the proceedings of the 10th International Conference on Bioinformatics and Biomedical Science (ICBBS 2021). On this occasion, we presented results of Shepp-Logan phantom reconstructions with IRLS-DRS focusing on CT images. The manuscript is at:

- FREITAS, G. L. A.; MENDES, C. J. M. R.; GONCALVES, V. P. *The Formation of Computed Tomography Images from Compressed Sampled One-dimensional Reconstructions*. 10th International Conference on Bioinformatics and Biomedical Science. *Proceedings*. In: ICBBS 2021: 2021 10TH INTERNATIONAL CONFERENCE ON BIOINFORMATICS AND BIOMEDICAL SCIENCE. Xiamen China: ACM, 29 out. 2021.

6.3 Future works

Equations 4.2 and 4.4 describe a set of CS-based medical imaging algorithms that use the direct method. In this work, we have made an initial assessment regarding one possible formulation, which still requires developing an adequate sparse representation strategy. Thus, based on the results we have presented, the following issues can be addressed in future research:

1. Other criteria for defining which discrete positions belong to the Cartesian radial lines can be tested in the algorithm for calculating frequency measurements from the sinogram. For example, instead of using the criterion based on the threshold

of a tolerance value, choose the closest Cartesian positions to each sample in the projections.

2. Definition of an efficient sparsifying transform for the one-dimensional signals reconstructed by IRLS-DRS. Some techniques, such as AI and dictionary learning, can be exploited in this context. Then, it is significant to conduct statistical analysis and qualitative evaluations in order to have more robust evidence for possible clinical application.

3. The analyses developed in this work did not consider how noisy measurements can interfere with reconstructed images. Thus, it is worth analyzing the DRS behavior in the presence of noise.

4. IRLS-DRS reconstructs each one-dimensional signal without taking into account the reconstructions of the other rows. Using prior information from one row in the reconstruction of another can speed up convergence and increase the quality of the results.

5. Other formulations of the DRS can be studied and tested. In Section 4.3, we pointed out that we expect to get more efficient DRS formulations if we can model the acquisition of measurements as a block diagonal matrix. However, future research can assess many other composition strategies. As further examples, we mention: (i) the reconstruction from the sinogram, exploring DFT formulations in polar coordinates, (ii) reconstruction of the image by blocks, and (iii) selection of certain positions of the spectrum so that the signals for image composition are in the real domain (note that in the IRLS-DRS case the reconstructed signals are complex). In MR, it is still possible to elaborate trajectories that may favor some specific DRS formulation.

6.4 Final Considerations

Medical imaging comprises very mature technologies. Thus, changes in the conception of such techniques are, and should be, cautious. In the bigger picture, new CS-based approaches may lead to safer and faster acquisition schemes, implying reduced manufacturing and operating costs for medical imaging equipment. Naturally, more efforts must be expended to enable such technological advances. Here, we have taken a few steps forward on a potential research direction: adopting direct methods in CS algorithms with a view to reducing the measurement requirement.

In summary, we have developed a CS algorithm that uses a direct method for medical image reconstruction. It gives more freedom to adopt smaller values of p

in the definition of the minimization problem, enabling a reduction in the number of measurements needed to obtain a good quality image. IRLS-DRS is indeed an algorithm that can reconstruct medical images from a smaller amount of measurements. However, developing an efficient sparsity representation strategy is still necessary to describe the typical structures of actual tomographic images, enabling the use in a real scenario.

Bibliography

[1] E. Bercovich and M. C. Javitt, "Medical imaging: From roentgen to the digital revolution, and beyond," *Rambam Maimonides Medical Journal*, vol. 9, 2018.

[2] G. Frija, I. Blažić, D. P. Frush, M. Hierath, M. G. Kawooya, L. Donoso-Bach, and B. Brkljačić, "How to improve access to medical imaging in low- and middle-income countries?" *EClinicalMedicine*, vol. 38, 2021.

[3] *Ethics and medical radiological imaging: a policy brief for health-care providers*, World Health Organization, Geneva, 2022. [Online]. Available: https://apps.who.int/iris/handle/10665/353046

[4] *Diagnostic imaging : what is it? When and how to use it where resources are limited?*, World Health Organization, Geneva, 2001. [Online]. Available: https://www.who.int/publications/i/item/diagnostic-imaging-what-is-it

[5] "Strengthening medical imaging," World Health Organization, accessed May 19, 2022. [Online]. Available: https://www.who.int/activities/strengthening-medical-imaging

[6] "Medevis (priority medical devices information system)," World Health Organization, accessed May 19, 2022. [Online]. Available: https://medevis.who-healthtechnologies.org/

[7] A. S. Panayides, A. Amini, N. D. Filipovic, A. Sharma, S. A. Tsaftaris, A. Young, D. Foran, N. Do, S. Golemati, T. Kurc, K. Huang, K. S. Nikita, B. P. Veasey, M. Zervakis, J. H. Saltz, and C. S. Pattichis, "Ai in medical imaging informatics: Current challenges and future directions," *IEEE Journal of Biomedical and Health Informatics*, vol. 24, no. 7, pp. 1837–1857, 2020.

[8] M. L. de Leeuw den Bouter, M. B. V. Gijzen, and R. F. Remis, "Conjugate gradient variants for ℓ_p-regularized image reconstruction in low-field mri," *SN Applied Sciences*, vol. 1, pp. 1–15, 2019.

[9] Y. Garcia, C. Franco, and C. J. Miosso, "Method for improved image reconstruction in computed tomography and positron emission tomography, based on compressive sensing with prefiltering in the frequency domain." CBEB 2020 - XXVII Congresso Brasileiro de Engenharia Biomédica, 2020.

[10] W. Xia, Z. Lu, Y. Huang, Z. Shi, Y. Liu, H. Chen, Y. Chen, J. Zhou, and Y. Zhang, "Magic: Manifold and graph integrative convolutional network for low-dose ct reconstruction," *IEEE Transactions on Medical Imaging*, vol. 40, pp. 3459–3472, 2021.

[11] C. Graff and E. Sidky, "Compressive sensing in medical imaging." *Applied optics*, vol. 54 8, pp. C23–44, 2015.

[12] D. L. Donoho, "Compressed sensing," *IEEE Transactions on information theory*, vol. 52, no. 4, pp. 1289–1306, 2006.

[13] S. Foucart and H. Rauhut, *A Mathematical Introduction to Compressive Sensing*, 2013.

[14] E. Candès, J. Romberg, and T. Tao, "Robust uncertainty principles: exact signal reconstruction from highly incomplete frequency information," *IEEE Transactions on Information Theory*, vol. 52, no. 2, pp. 489–509, 2006.

[15] G. Chen, D. Li, and J. Zhang, "Iterative gradient projection algorithm for two-dimensional compressive sensing sparse image reconstruction," *Signal Processing*, vol. 104, pp. 15–26, 2014. [Online]. Available: https://www.sciencedirect.com/science/article/pii/S0165168414001443

[16] C. Zhang, T. Zhang, M. Li, C. Peng, Z. Liu, and J. Zheng, "Low-dose ct reconstruction via l1 dictionary learning regularization using iteratively reweighted least-squares," *BioMedical Engineering OnLine*, vol. 15, 2016.

[17] R. Chartrand, "Exact reconstruction of sparse signals via nonconvex minimization," *IEEE Signal Processing Letters*, vol. 14, no. 10, pp. 707–710, 2007.

[18] H. Li, W. Guo, Z. Sun, and W. Wang, "Adaptive kalman filtered compressive sensing for streaming signals," *2013 IEEE 78th Vehicular Technology Conference (VTC Fall)*, pp. 1–5, 2013.

[19] D. Y. M. Y. Abdallah, "History of medical imaging," *Archives of Medicine and Health Sciences*, vol. 5, p. 275, 2017.

[20] A. C. Kak and M. Slaney, *Principles of computerized tomographic imaging*. SIAM, 2001.

[21] J. Hsieh, *Computed tomography: Principles, design, artifacts, and recent advances*. Wiley Interscience, 2009.

[22] R. Brown, Y. Cheng, E. Haacke, M. Thompson, and R. Venkatesan, *Magnetic Resonance Imaging: Physical Principles and Sequence Design*. Wiley, 2014.

[23] J. P. Cohen, P. Morrison, and L. Dao, "Covid-19 image data collection," *arXiv 2003.11597*, 2020. [Online]. Available: https://github.com/ieee8023/covid-chestxray-dataset

[24] M. J. Willemink and P. B. Noël, "The evolution of image reconstruction for CT—from filtered back projection to artificial intelligence," *European Radiology*, vol. 29, no. 5, pp. 2185–2195, 2019.

[25] A. E. Campbell-Washburn, R. Ramasawmy, M. C. Restivo, I. Bhattacharya, B. Basar, D. A. Herzka, M. S. Hansen, T. Rogers, W. P. Bandettini, D. R. McGuirt, C. Mancini, D. M. Grodzki, R. Schneider, W. Majeed, H. Bhat, H. Xue, J. Moss, A. A. Malayeri, E. C. Jones, A. P. Koretsky, P. Kellman, M. Y. Chen, R. J. Lederman, and R. S. Balaban, "Opportunities in interventional and diagnostic imaging by using high-performance low-field-strength mri." *Radiology*, p. 190452, 2019.

[26] W. Hinshaw and A. Lent, "An introduction to nmr imaging: From the bloch equation to the imaging equation," *Proceedings of the IEEE*, vol. 71, no. 3, pp. 338–350, 1983.

[27] B.-C. FBIRN, MBIRN, S. Gadde, N. Aucoin, J. S. Grethe, D. B. Keator, D. S. Marcus, and S. Pieper, "Xcede: An extensible schema for biomedical data," *Neuroinformatics*, vol. 10, no. 1, p. 19–32, Jan 2012. [Online]. Available: http://link.springer.com/10.1007/s12021-011-9119-9

[28] M. S. Hansen and P. Kellman, "Image reconstruction: An overview for clinicians," *Journal of Magnetic Resonance Imaging*, vol. 41, 2015.

[29] A. Ware, "Fast approximate fourier transforms for irregularly spaced data," *SIAM Rev.*, vol. 40, pp. 838–856, 1998.

[30] D. Ruiz-Antolín and A. Townsend, "A nonuniform fast fourier transform based on low rank approximation," *SIAM Journal on Scientific Computing*, vol. 40, no. 1, pp. A529–A547, 2018.

[31] G. E. Sarty, R. Bennett, and R. W. Cox, "Direct reconstruction of non-cartesian k-space data using a nonuniform fast fourier transform," *Magnetic Resonance in Medicine*, vol. 45, 2001.

[32] J. A. Fessler, "On nufft-based gridding for non-cartesian mri," *Journal of Magnetic Resonance*, vol. 188, no. 2, pp. 191–195, 2007. [Online]. Available: https://www.sciencedirect.com/science/article/pii/S1090780707002054

[33] L. A. Shepp and B. F. Logan, "The fourier reconstruction of a head section," *IEEE Transactions on Nuclear Science*, vol. 21, no. 3, pp. 21–43, 1974.

[34] E. Abadi, W. P. Segars, B. M. W. Tsui, P. Kinahan, N. Bottenus, A. F. Frangi, A. D. A. Maidment, J. Y. Lo, and E. Samei, "Virtual clinical trials in medical imaging: a review," *Journal of Medical Imaging*, vol. 7, 2020.

[35] C. E. Shannon, "A mathematical theory of communication," *Bell Syst. Tech. J.*, vol. 27, pp. 623–656, 1948.

[36] H. Nyquist, "Certain topics in telegraph transmission theory," *Transactions of the American Institute of Electrical Engineers*, vol. 47, pp. 617–644.

[37] M. Elad, *Sparse and Redundant Representations: From Theory to Applications in Signal and Image Processing*, 1st ed. Springer Publishing Company, Incorporated, 2010.

[38] L. Stankovic, D. P. Mandic, M. Dakovic, and I. Kisil, "Demystifying the coherence index in compressive sensing [lecture notes]," *IEEE Signal Processing Magazine*, vol. 37, no. 1, pp. 152–162, 2020.

[39] S. S. Chen, D. L. Donoho, and M. A. Saunders, "Atomic decomposition by basis pursuit," *Siam Review*, vol. 43, pp. 129–159, 2001.

[40] Y. Shen and S. Li, "Restricted p–isometry property and its application for nonconvex compressive sensing," *Advances in computational mathematics*, vol. 37, no. 3, pp. 441–452, 2011.

[41] C. Emmanuel, J. Romberg, and T. Tao, "Stable signal recovery from incomplete and inaccurate measurements," 2005.

[42] E. J. Candès, "The restricted isometry property and its implications for compressed sensing," *Comptes Rendus Mathematique*, vol. 346, no. 9, pp. 589–592, 2008. [Online]. Available: https://www.sciencedirect.com/science/article/pii/S1631073X08000964

[43] J. D. Blanchard, C. Cartis, and J. Tanner, "Compressed sensing: How sharp is the restricted isometry property?" *SIAM Review*, vol. 53, no. 1, pp. 105–125, 2011.

[44] R. Chartrand and V. Staneva, "Restricted isometry properties and nonconvex compressive sensing," *Inverse Problems*, vol. 24, no. 3, p. 035020, may 2008. [Online]. Available: https://doi.org/10.1088/0266-5611/24/3/035020

[45] B. Chen and A. Wan, "General rip bounds of δ_{tk} for sparse signals recovery by ℓ_p minimization," *Neurocomputing*, vol. 363, pp. 306–312, 2019. [Online]. Available: https://www.sciencedirect.com/science/article/pii/S0925231219309300

[46] S. Dirksen, G. Lecué, and H. Rauhut, "On the gap between restricted isometry properties and sparse recovery conditions," *IEEE Transactions on Information Theory*, vol. 64, no. 8, pp. 5478–5487, 2018.

[47] Y. Arjoune, N. Kaabouch, H. El Ghazi, and A. Tamtaoui, "Compressive sensing: Performance comparison of sparse recovery algorithms," in *2017 IEEE 7th Annual Computing and Communication Workshop and Conference (CCWC)*, 2017, pp. 1–7.

[48] R. Chartrand and W. Yin, "Iteratively reweighted algorithms for compressive sensing," *2008 IEEE International Conference on Acoustics, Speech and Signal Processing*, pp. 3869–3872, 2008.

[49] C. Miosso, R. Borries, and J. Pierluissi, "Compressive sensing method for improved reconstruction of gradient-sparse magnetic resonance images," 12 2009, pp. 799 – 806.

[50] G. L. Freitas, C. J. M. R. Mendes, and V. P. Goncalves, "The formation of computed tomography images from compressed sampled one-dimensional reconstructions," *2021 10th International Conference on Bioinformatics and Biomedical Science*, 2021.

[51] G. Goertzel, "An algorithm for the evaluation of finite trigonometric series," *The American Mathematical Monthly*, vol. 65, no. 1, pp. 34–35, 1958. [Online]. Available: http://www.jstor.org/stable/2310304

[52] P. Sysel and P. Rajmic, "Goertzel algorithm generalized to non-integer multiples of fundamental frequency," *EURASIP Journal on Advances in Signal Processing*, vol. 2012, pp. 1–8, 2012.

[53] M. R. Hestenes and E. Stiefel, "Methods of conjugate gradients for solving linear systems," *Journal of research of the National Bureau of Standards*, vol. 49, pp. 409–435, 1952.

[54] Y. Hu and Y. Wang, "An efficient projected gradient method for convex constrained monotone equations with applications in compressive sensing," *Journal of Applied Mathematics and Physics*, vol. 8, pp. 983–998, 2020.

[55] M. Sun, J. Liu, and Y. Wang, "Two improved conjugate gradient methods with application in compressive sensing and motion control," *Mathematical Problems in Engineering*, vol. 2020, pp. 1–11, 2020.

[56] Z. Wang, A. Bovik, H. Sheikh, and E. Simoncelli, "Image quality assessment: from error visibility to structural similarity," *IEEE Transactions on Image Processing*, vol. 13, no. 4, pp. 600–612, 2004.

[57] J. L. Hodges, "The significance probability of the smirnov two-sample test," *Arkiv för Matematik*, vol. 3, no. 5, p. 469–486, Jan 1958. [Online]. Available: http://projecteuclid.org/euclid.afm/1485893310

[58] M. A. Stephens, "Asymptotic results for goodness-of-fit statistics with unknown parameters," *The Annals of Statistics*, vol. 4, no. 2, pp. 357–369, 1976. [Online]. Available: http://www.jstor.org/stable/2958206

[59] F. Wilcoxon, "Individual comparisons by ranking methods," *Biometrics Bulletin*, vol. 1, no. 6, p. 80, Dec 1945. [Online]. Available: https://www.jstor.org/stable/10.2307/3001968?origin=crossref

Appendix A

Additional plots

The following figures refer to the Experiment 2 in Section 5.4.

A.1 CT1 actual image

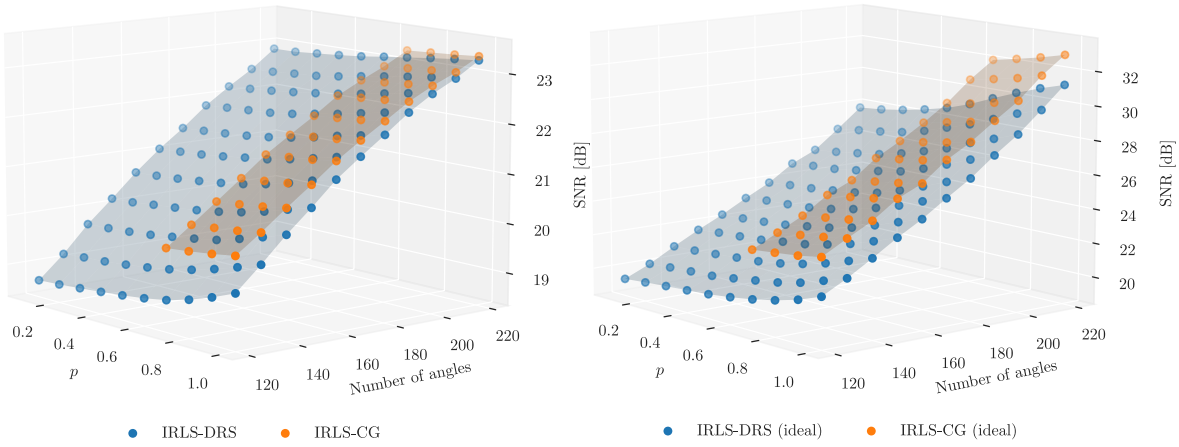

(a) Non-ideal measurements.

(b) Ideal measurements

Figure A.1 – SNR achieved by the reconstructions of the CT1 actual image. Each surface corresponds to a reconstructions algorithm.

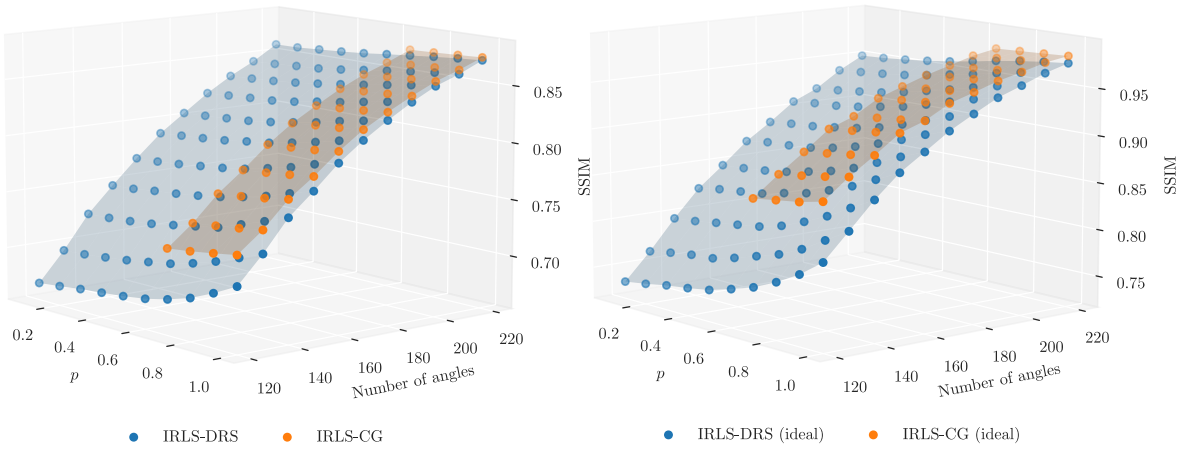

(a) Non-ideal measurements. (b) Ideal measurements

Figure A.2 – SSIM achieved by the reconstructions of the CT1 actual image. Each surface corresponds to a reconstructions algorithm

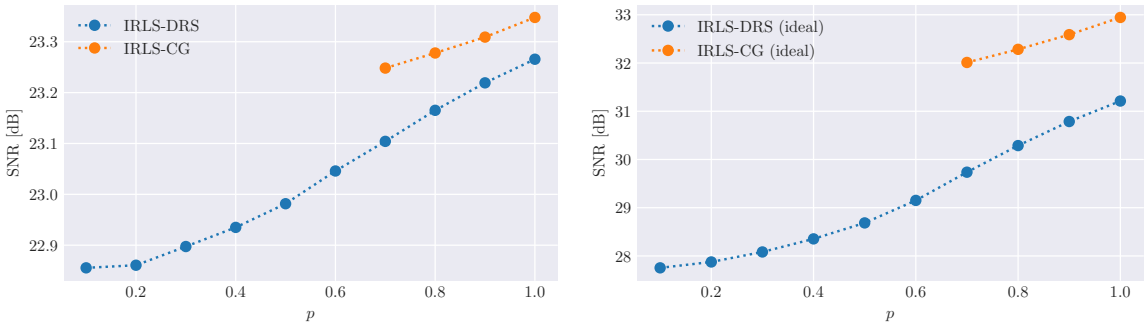

(a) Non-ideal measurements. (b) Ideal measurements.

Figure A.3 – SNR achieved by the reconstructions computed using measurements along 220 radial lines of the CT1 actual image. Each curve corresponds to a reconstruction algorithm.

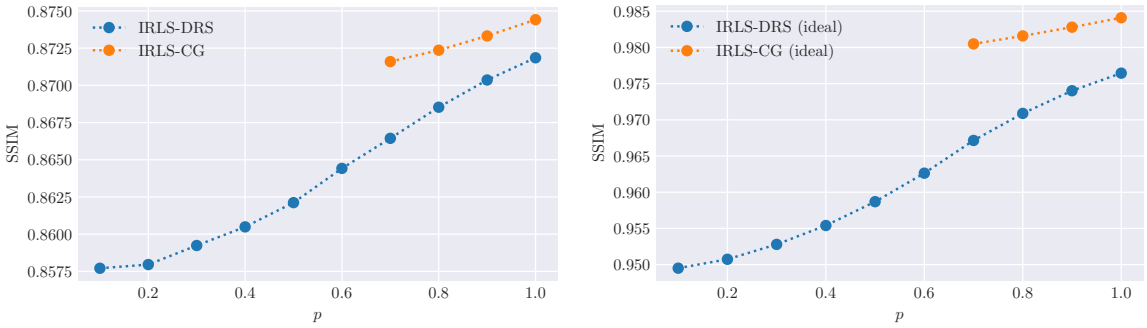

(a) Non-ideal measurements. (b) Ideal measurements

Figure A.4 – SSIM achieved by the reconstructions computed using measurements along 220 radial lines of the CT1 actual image. Each curve corresponds to a reconstruction algorithm.

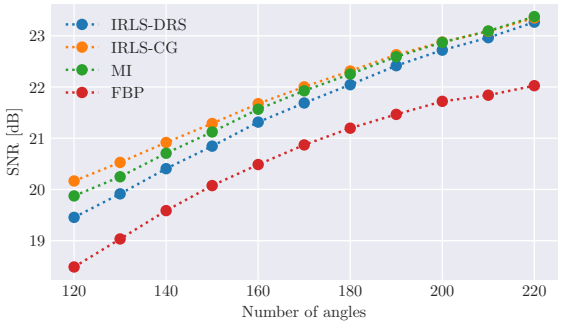

(a) Non-ideal measurements.

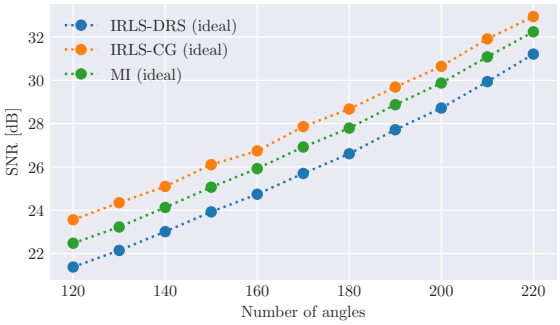

(b) Ideal measurements

Figure A.5 – SNR achieved by the reconstructions of the CT1 actual image. Each curve corresponds to a reconstruction algorithm. The CS-based approaches used $p = 1$ in the minimization step.

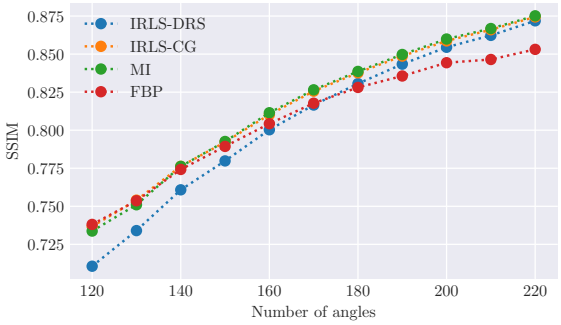

(a) Non-ideal measurements.

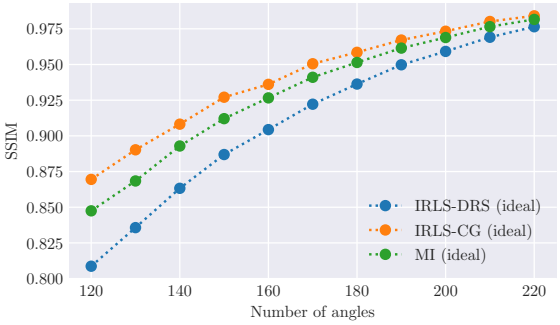

(b) Ideal measurements

Figure A.6 – SSIM achieved by the reconstructions of the CT1 actual image. Each curve corresponds to a reconstruction algorithm. The CS-based approaches used $p = 1$ in the minimization step.

A.2 CT2 actual image

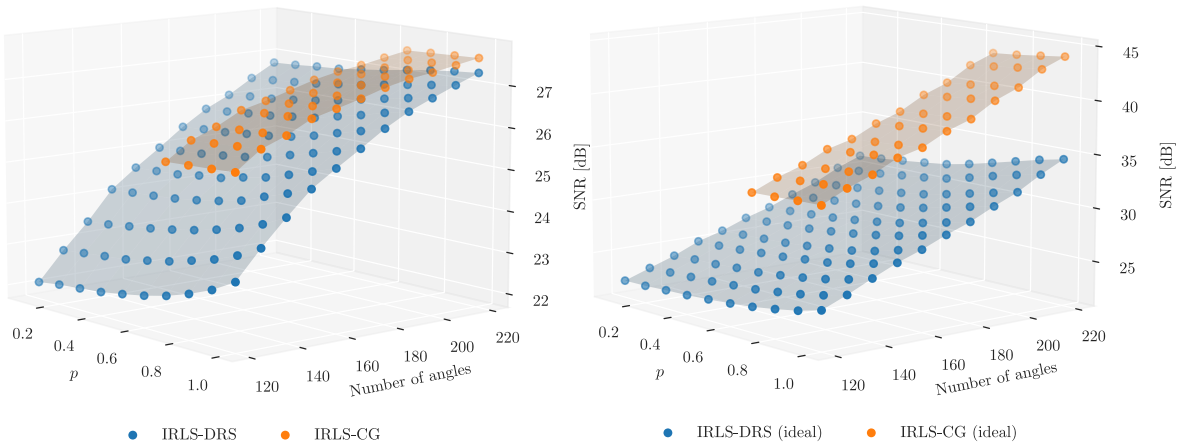

(a) Non-ideal measurements. (b) Ideal measurements

Figure A.7 – SNR achieved by the reconstructions of the CT2 actual image. Each surface corresponds to a reconstructions algorithm.

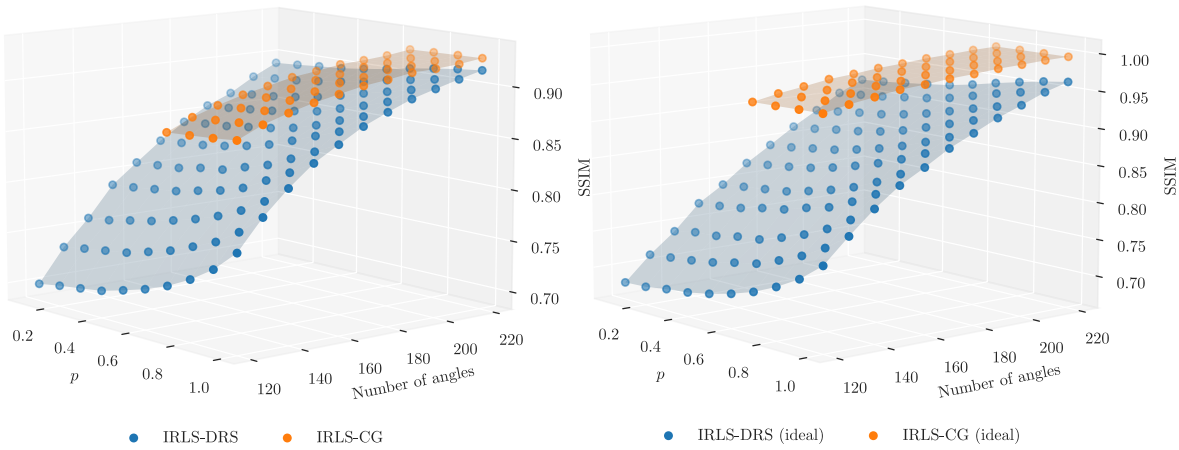

(a) Non-ideal measurements. (b) Ideal measurements

Figure A.8 – SSIM achieved by the reconstructions of the CT2 actual image. Each surface corresponds to a reconstructions algorithm

(a) Non-ideal measurements.

(b) Ideal measurements.

Figure A.9 – SNR achieved by the reconstructions computed using measurements along 220 radial lines of the CT2 actual image. Each curve corresponds to a reconstruction algorithm.

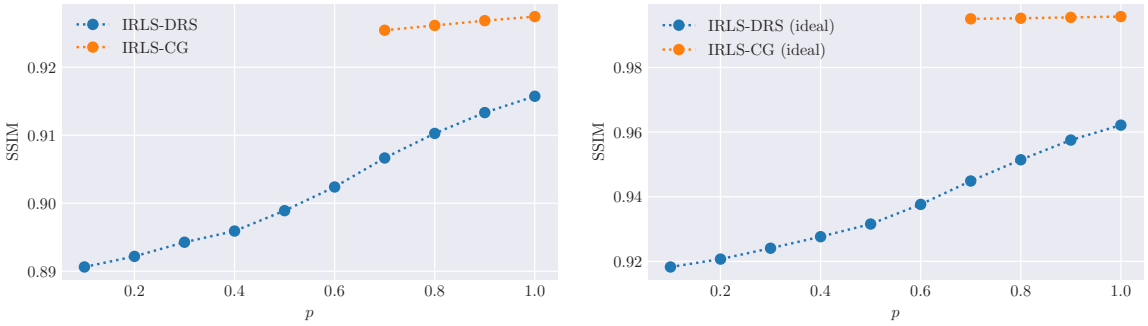

(a) Non-ideal measurements.

(b) Ideal measurements

Figure A.10 – SSIM achieved by the reconstructions computed using measurements along 220 radial lines of the CT2 actual image. Each curve corresponds to a reconstruction algorithm.

A.3 MR1 actual image

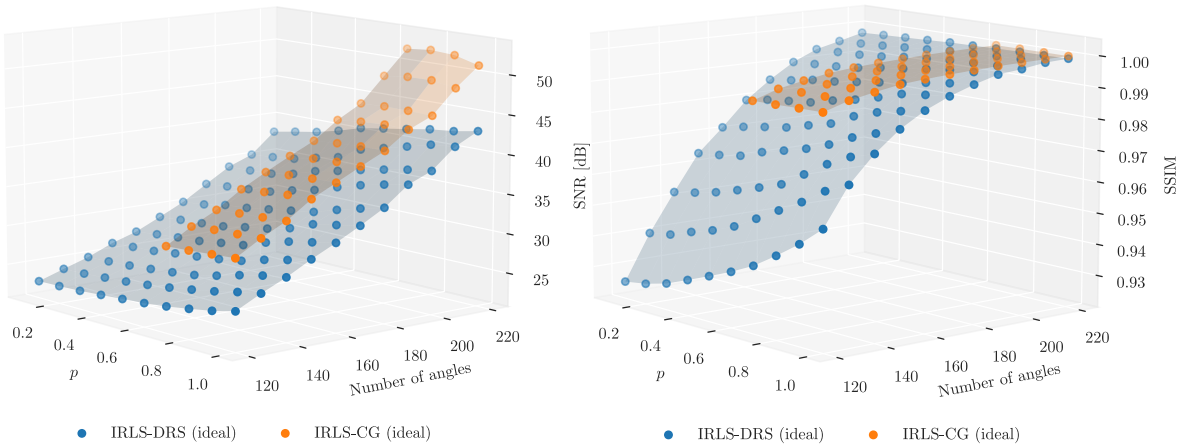

(a) SNR. (b) SSIM.

Figure A.11 – Quality indices achieved by the reconstructions of the MR1 actual image. Each surface corresponds to a reconstructions algorithm.

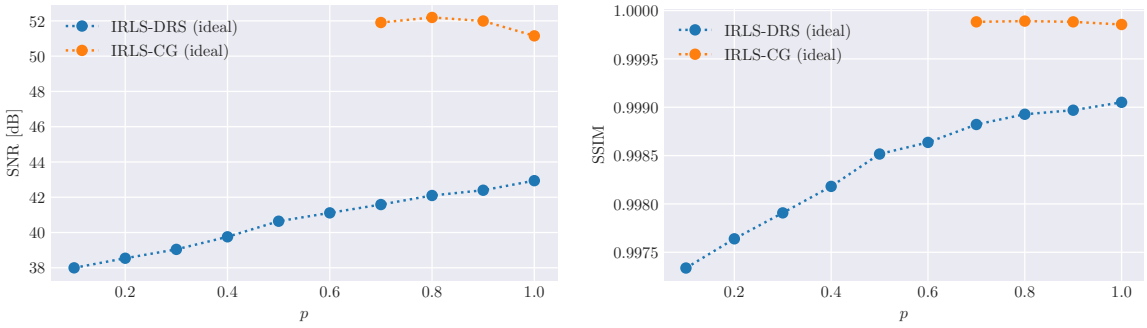

(a) SNR. (b) SSIM.

Figure A.12 – Quality indices achieved by the reconstructions computed using measurements along 220 radial lines of the MR1 actual image. Each surface corresponds to a reconstructions algorithm. Each curve corresponds to a reconstruction algorithm.

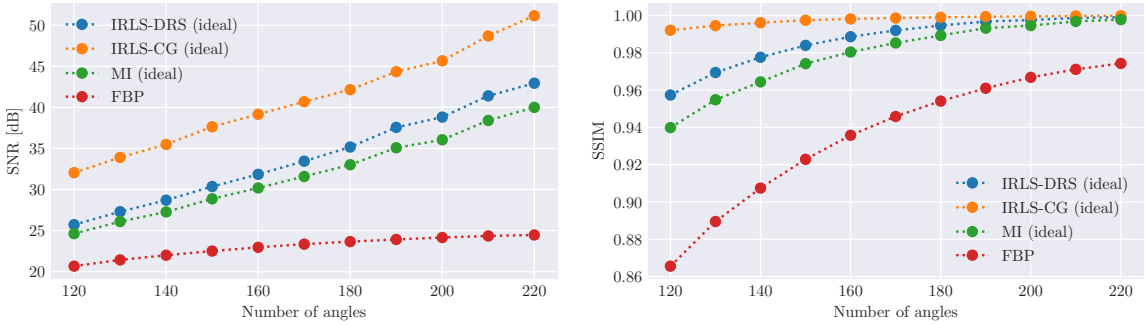

(a) SNR. (b) SSIM.

Figure A.13 – Quality indices achieved by the reconstructions of the MR1 actual image. Each curve corresponds to a reconstruction algorithm. The CS-based approaches used $p = 1$ in the minimization step.

A.4 MR2 actual image

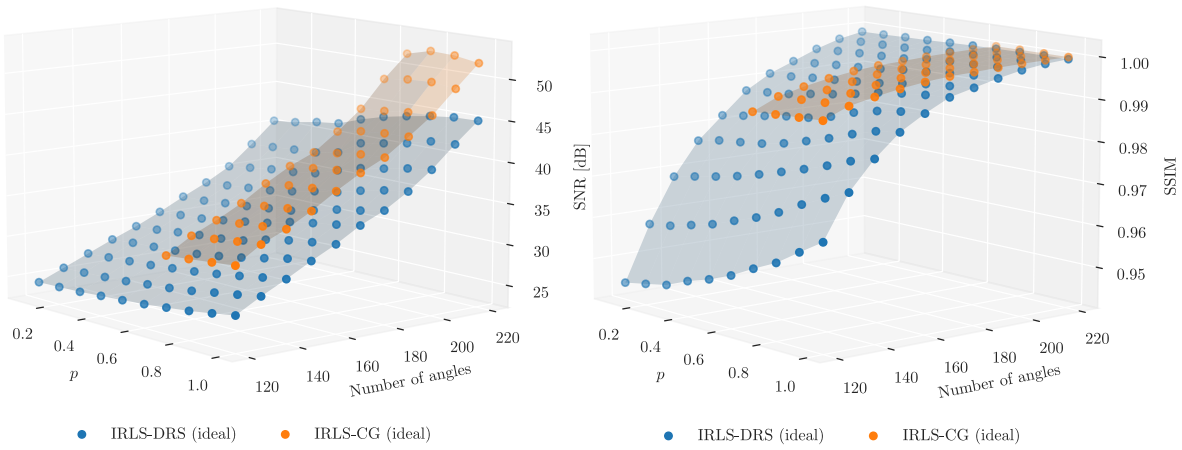

(a) SNR. (b) SSIM.

Figure A.14 – Quality indices achieved by the reconstructions of the MR2 actual image. Each surface corresponds to a reconstructions algorithm.

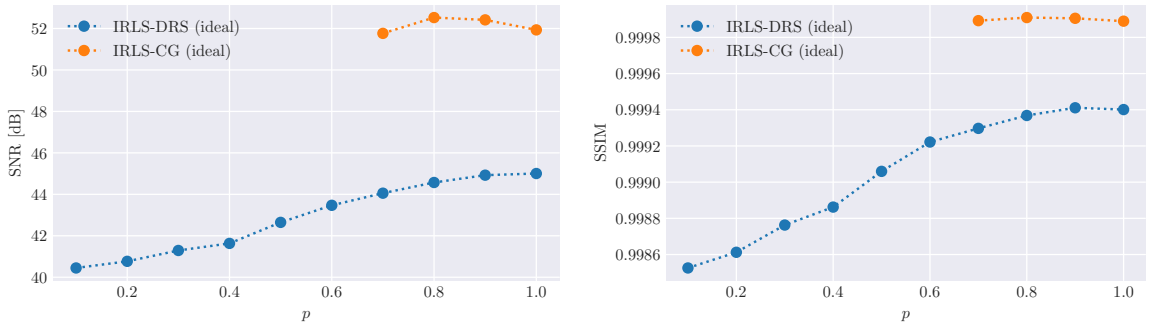

(a) SNR. (b) SSIM.

Figure A.15 – Quality indices achieved by the reconstructions computed using measurements along 220 radial lines of the MR2 actual image. Each curve corresponds to a reconstruction algorithm.

Appendix B

Additional reconstructed images

The following figures refer to the Experiment 2 in Section 5.4.

B.1 CT1 actual image

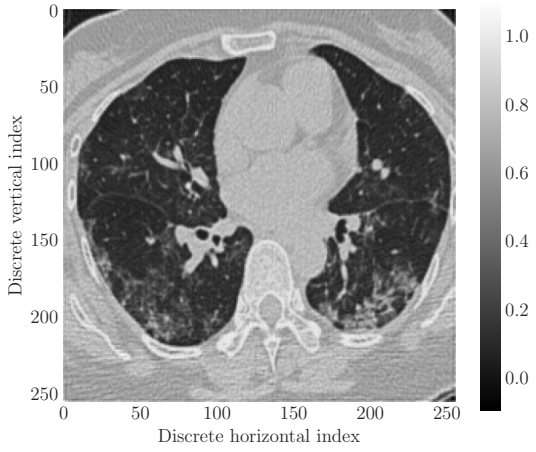

(a) FBP.

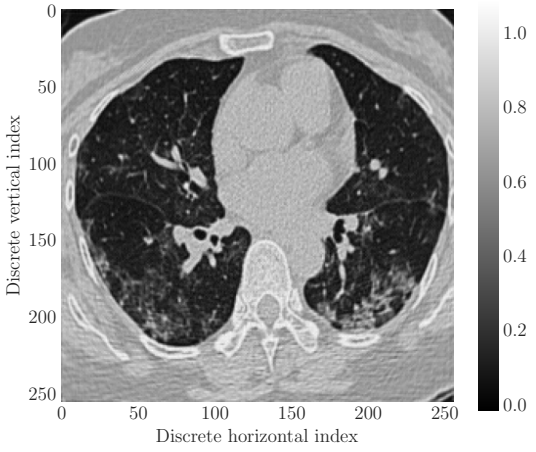

(b) MI.

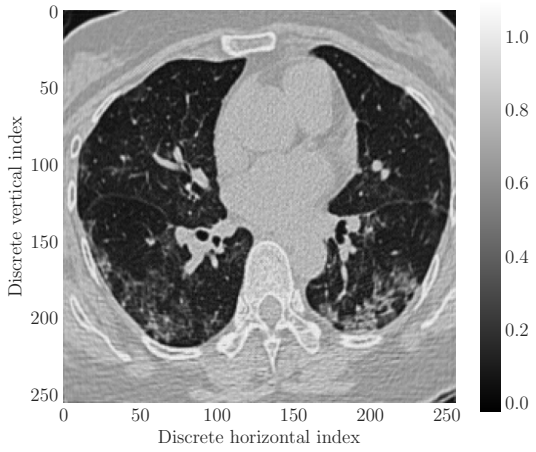

(c) IRLS-DRS ($p = 1$).

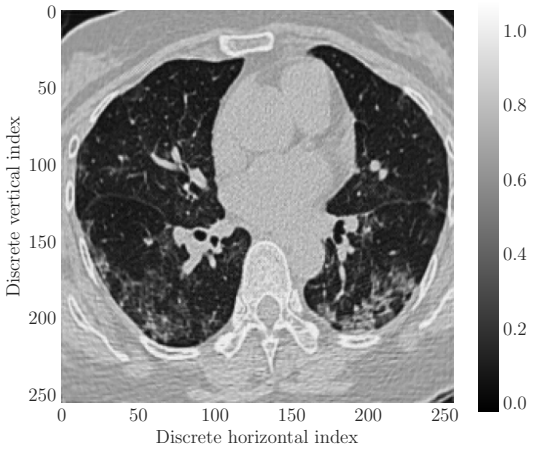

(d) IRLS-CG ($p = 1$).

Figure B.1 – Reconstructions of the CT1 actual image from non-ideal measurements taken in 200 angles.

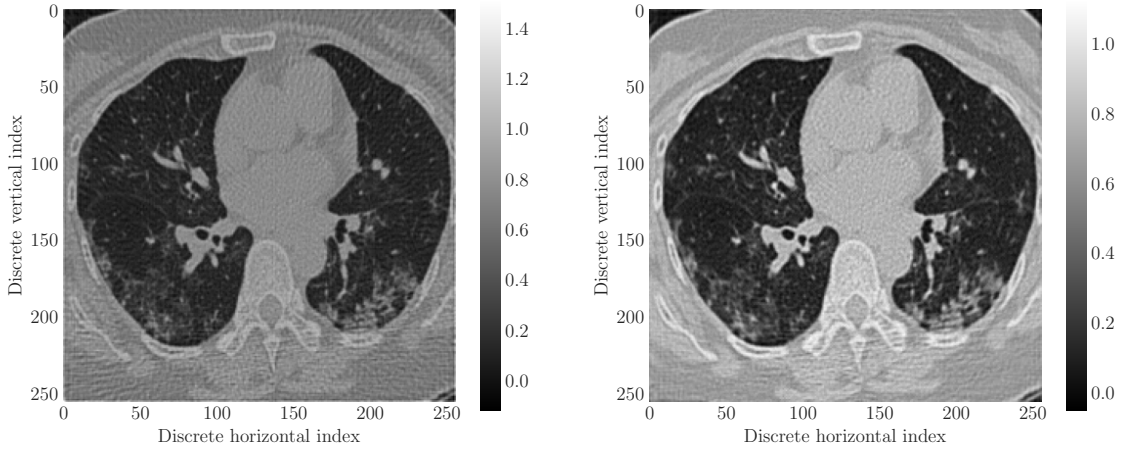

(a) FBP.

(b) MI.

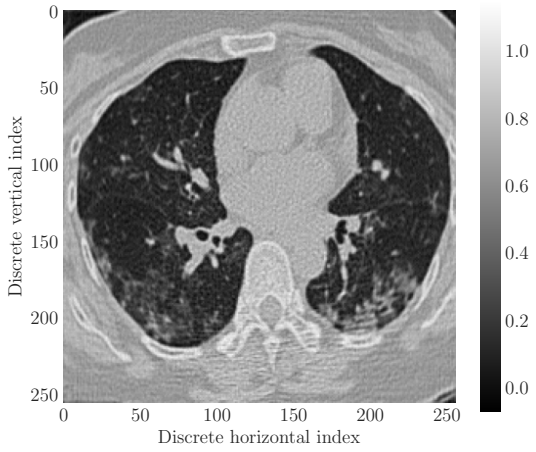

(c) IRLS-DRS ($p = 1$).

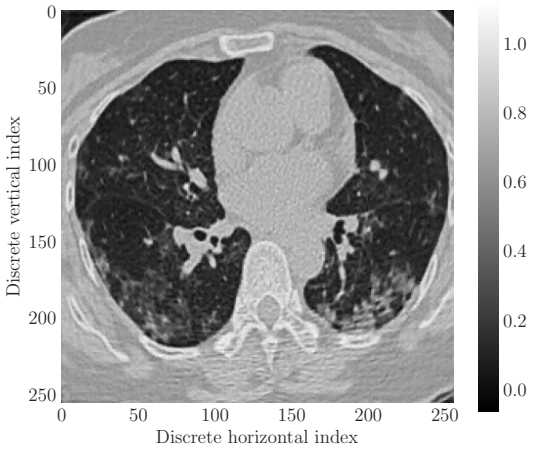

(d) IRLS-CG ($p = 1$).

Figure B.2 – Reconstructions of the CT1 actual image from non-ideal measurements taken in 120 angles.

B.2 CT2 actual image

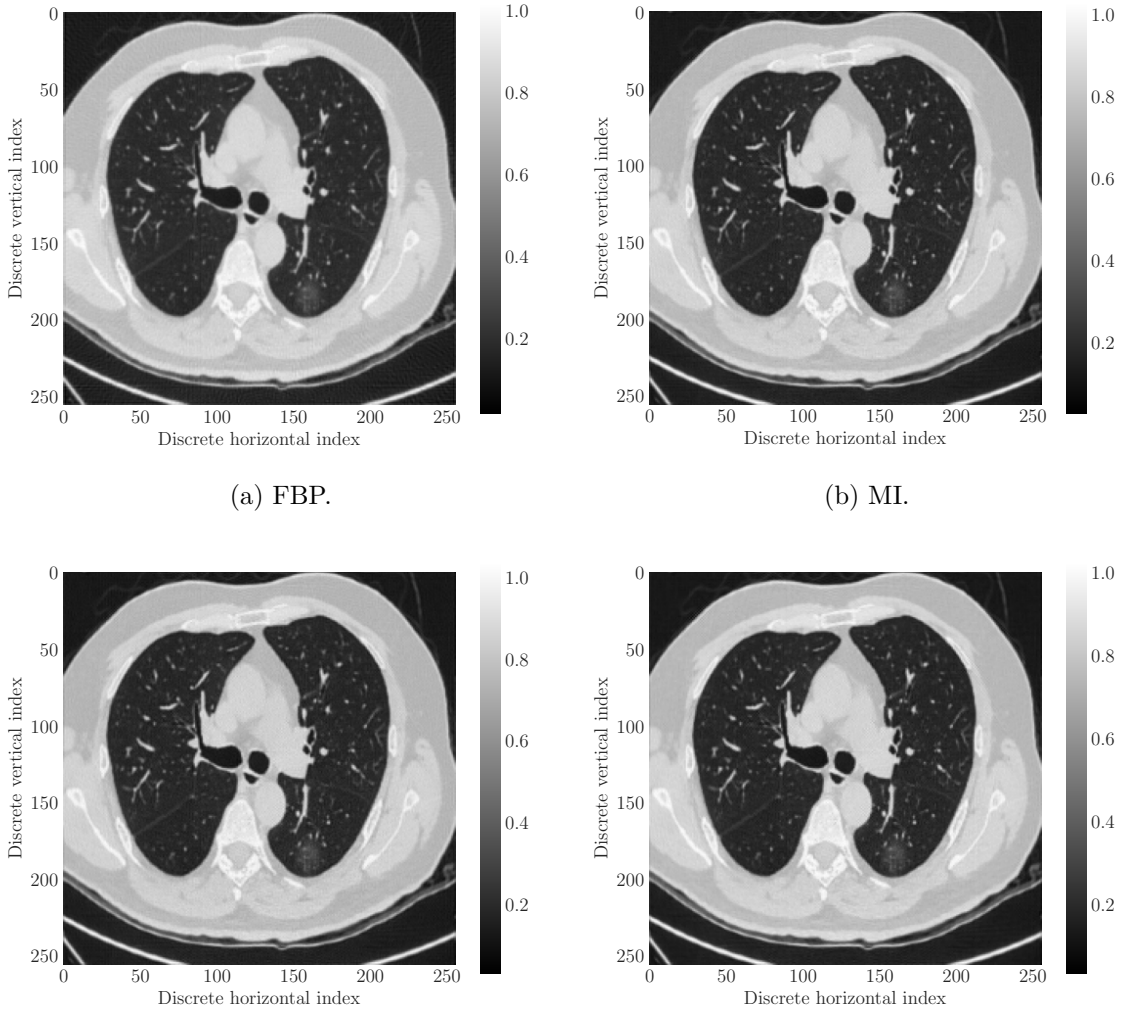

(a) FBP.

(b) MI.

(c) IRLS-DRS ($p = 1$).

(d) IRLS-CG ($p = 1$).

Figure B.3 – Reconstructions of the CT2 actual image from non-ideal measurements taken in 200 angles.

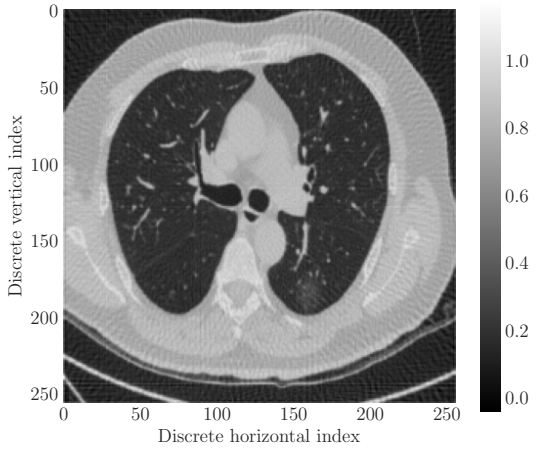

(a) FBP.

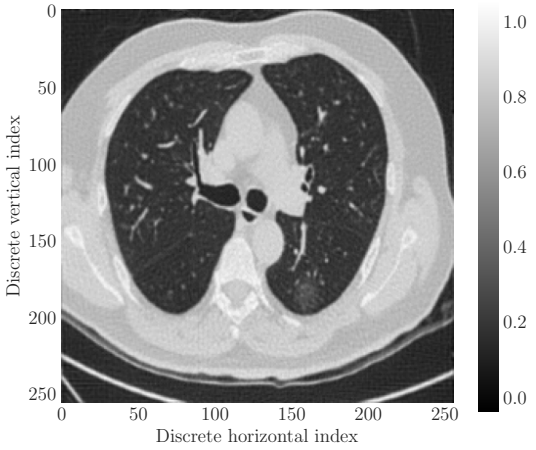

(b) MI.

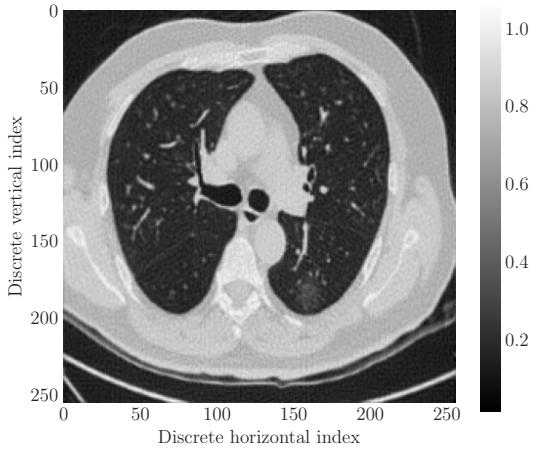

(c) IRLS-DRS ($p = 1$).

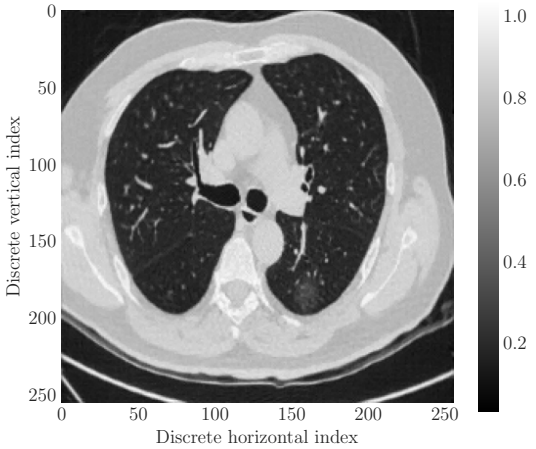

(d) IRLS-CG ($p = 1$).

Figure B.4 – Reconstructions of the CT2 actual image from non-ideal measurements taken in 120 angles.

B.3 MR1 actual image

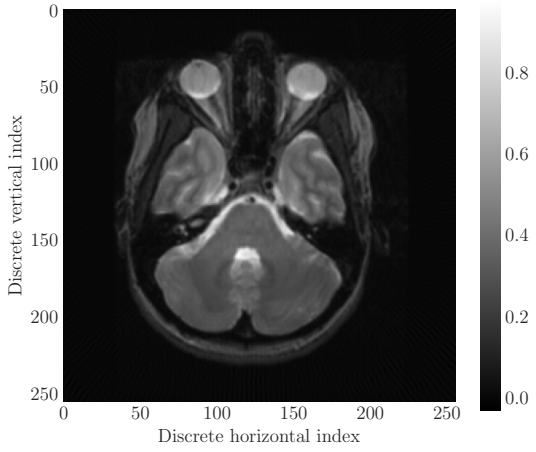

(a) FBP.

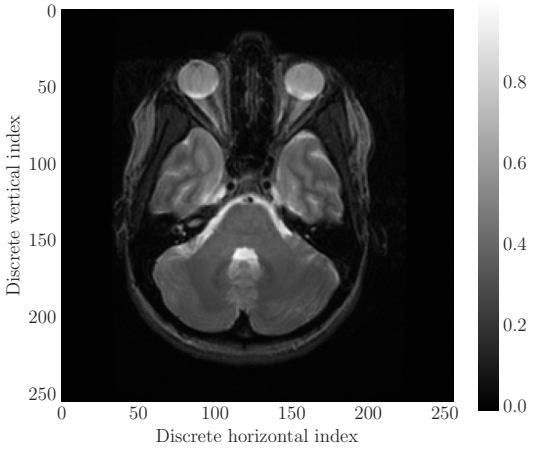

(b) MI.

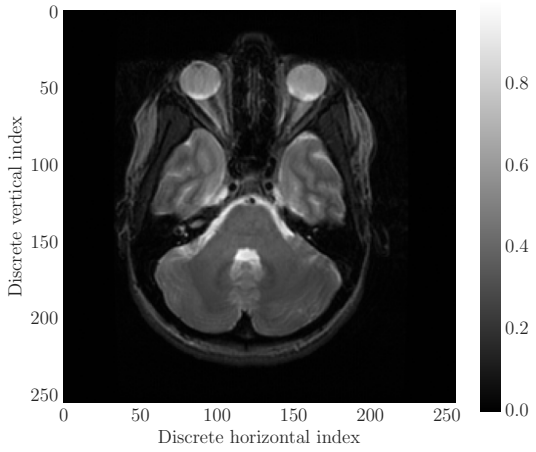

(c) IRLS-DRS ($p = 1$).

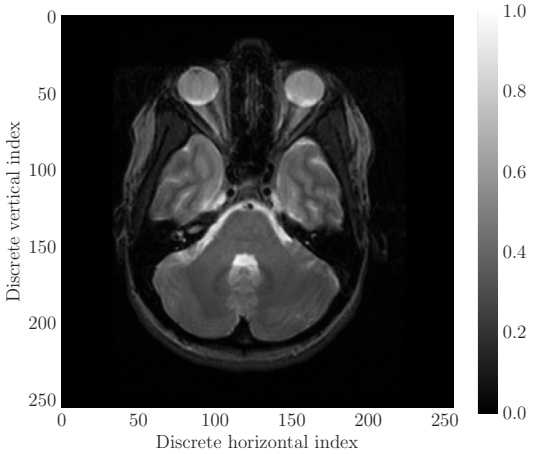

(d) IRLS-CG ($p = 1$).

Figure B.5 – Reconstructions of the MR1 actual image measurements taken in 200 angles.

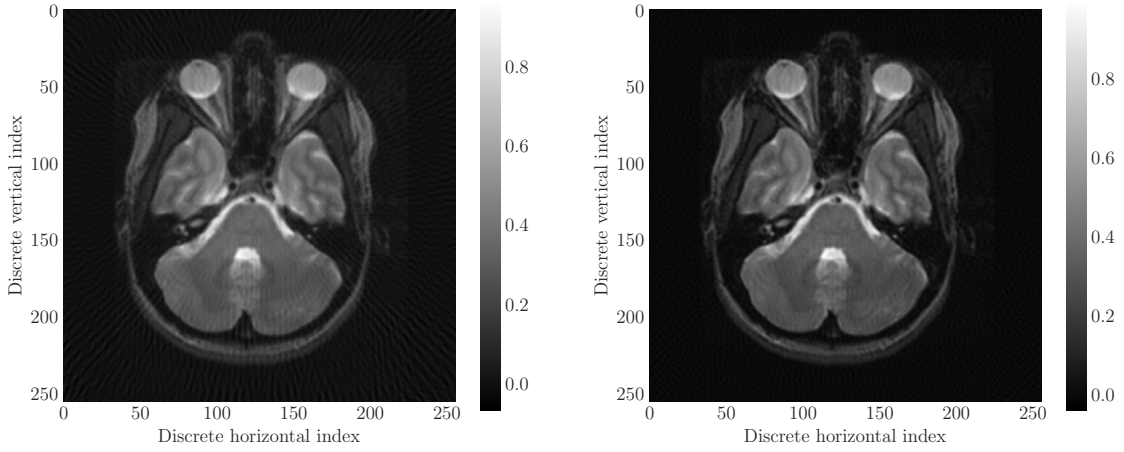

(a) FBP.

(b) MI.

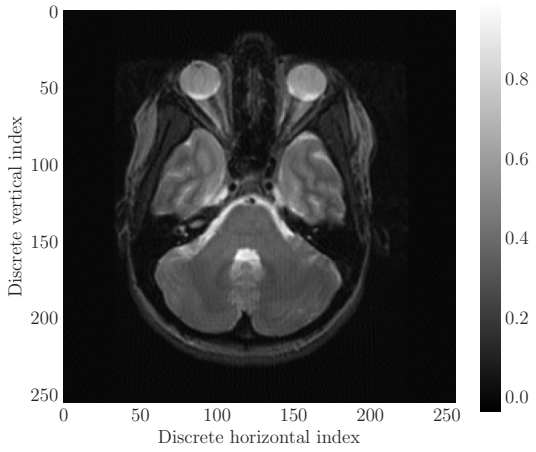

(c) IRLS-DRS ($p = 1$).

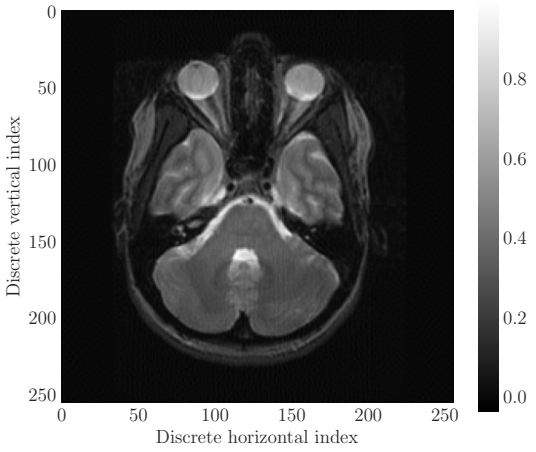

(d) IRLS-CG ($p = 1$).

Figure B.6 – Reconstructions of the MR1 actual image measurements taken in 120 angles.

B.4 MR2 actual image

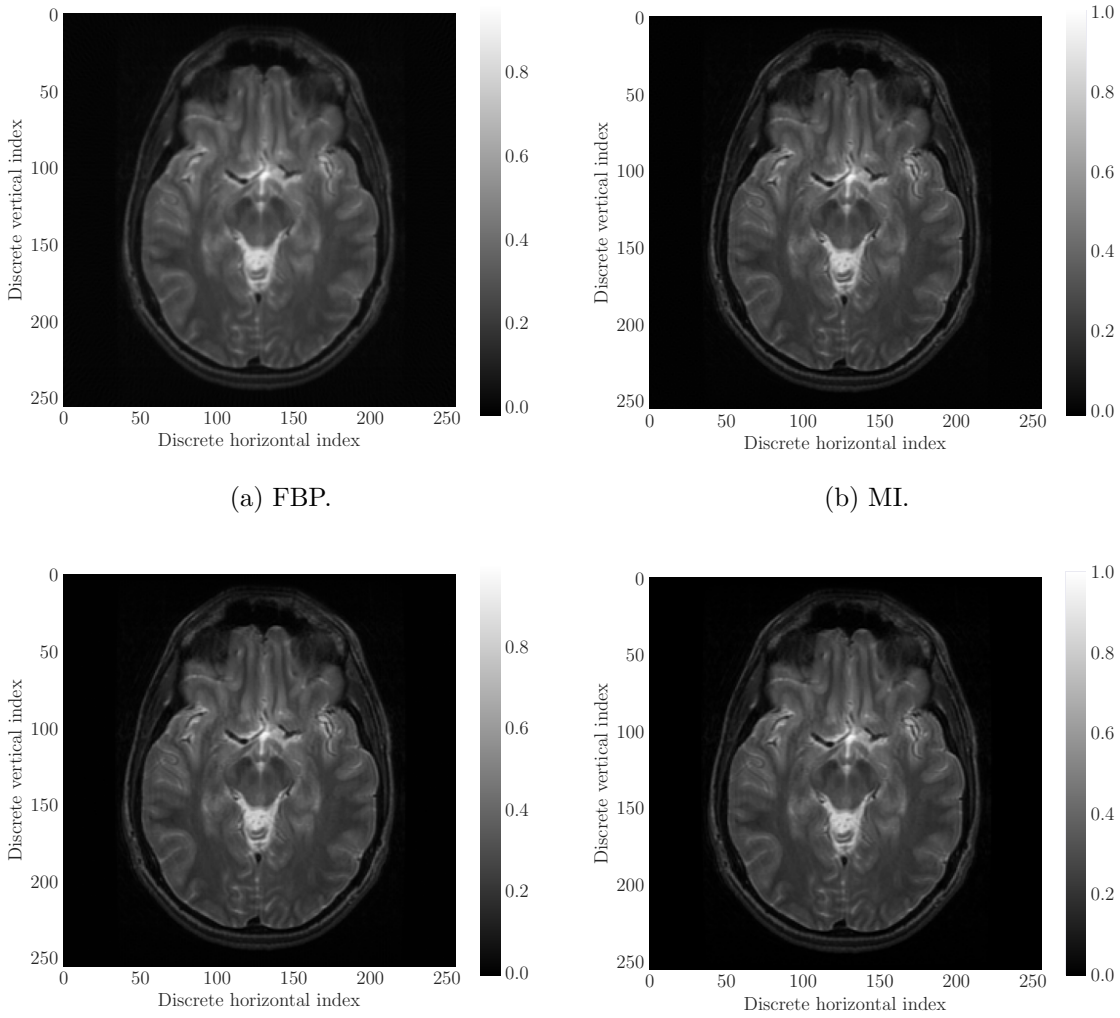

(a) FBP.

(b) MI.

(c) IRLS-DRS ($p = 1$).

(d) IRLS-CG ($p = 1$).

Figure B.7 – Reconstructions of the MR2 actual image measurements taken in 200 angles.

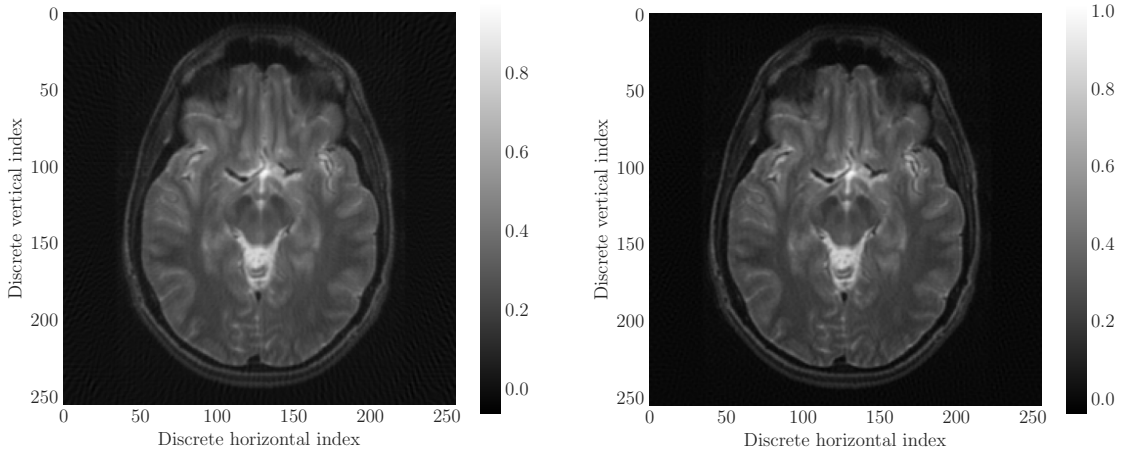

(a) FBP.

(b) MI.

(c) IRLS-DRS ($p = 1$).

(d) IRLS-CG ($p = 1$).

Figure B.8 – Reconstructions of the MR2 actual image measurements taken in 120 angles.